Synthesis and Thermodynamic Studies of Physisorptive Energy Storage Materials

Thesis by
Nicholas Stadie

In Partial Fulfillment of the Requirements
for the Degree of
Doctor of Philosophy

California Institute of Technology
Pasadena, California

2013
(defended November 5, 2012)

“Be glad of life,
for it gives you the chance
to love and to work and to play
and to look up at the stars…”
- Henry van Dyke

Acknowledgements

I had many great teachers who gave me a solid platform on which to build my work, among them Profs. John Kouvetakis, Edward Skibo, Karl Booksh, Tim Steimle, and Ulrich Hausermann. I credit my love of chemistry to Mr. Achtziger and Mr. Ishihara. Professor George Wolf remains a great inspiration to me, especially his commitment to teaching; I strive to live up to his standards. Prof. Wilson Francisco was responsible for giving me the confidence to seek a higher education, and is a seemingly infinite source of positive energy. With Prof. Michael O'Keeffe, I first saw the beauty of materials and periodic structures. I will always feel very privileged to have had the opportunity to work in his laboratory, and fondly remember our lunches together drawing nets and picking apart the periodic table.

The work presented in this thesis would not have been possible without discussions and collaborations with John Vajo and Robert Cumberland at HRL Laboratories, Joe Reiter and Bob Bowman at JPL, and the members of the Hydrogen and Energy group at EMPA. I thank Carol Garland for many patient hours sitting next to me at the TEM, and Sonjong Hwang and Joseph Beardslee for thoughtful discussions and assisting me with (crucial and timely) measurements. I would like to give special thanks to Mike Vondrus whose talents contributed to the success of building the high-pressure Sieverts apparatus, and who devoted extra time to making my life easier. Many other friendly

faces around campus (especially in the central warehouse) made the fabrication work truly a pleasure. Finally, Pam Albertson deserves a monument of credit for keeping us all on track.

I am very grateful to Justin Purewal who taught me how to (carefully) do the experimental science described in this thesis. Andrew Wilson was an honor to have mentored and his hard work will continue to be appreciated long after his short visit. Max Murialdo was tireless in helping with measurements during the final portion of this thesis work and the quantity of data that contributed to the quality of the final results is in large part due to his efforts. I also thank the rest of the Fultz group for keeping me motivated and setting the bar very high; I hope you'll forgive me for (occasionally) hoarding all the good tools.

I thank my thesis committee for thoughtful discussions of this material and for half a decade of coursework and guidance. I thank Channing Ahn for being a challenge-loving, risk-taking, always jovial, and straight-shooting adviser. I thank Brent Fultz for always encouraging me, leading by example, giving us students more than our fair share of his time and careful thought, and creating a model group atmosphere for carrying out effective and rewarding science. It was an honor and a pleasure to be in this group.

I draw endless inspiration to work as hard as I can from my family and friends. All my work is dedicated to Eyrún, who makes me undeniably happy.

Abstract

Physical adsorption of hydrogen or other chemical fuels on the surface of carbonaceous materials offers a promising avenue for energy storage applications. The addition of a well-chosen sorbent material to a compressed gas tank increases the volumetric energy density of the system while still permitting fast refueling, simplicity of design, complete reversibility, high cyclability, and low overall cost of materials. While physical adsorption is most effective at temperatures below ambient, effective storage technologies are possible at room temperature and modestly high pressure. A volumetric Sieverts apparatus was designed, constructed, and commissioned to accurately measure adsorption uptake at high pressures and an appropriate thermodynamic treatment of the experimental data is presented.

In Chapter 1, the problem of energy storage is introduced in the context of hydrogen as an ideal alternative fuel for future mobile vehicle applications, and with methane in mind as a near-term solution. The theory of physical adsorption that is relevant to this work is covered in Chapter 2. In-depth studies of two classes of materials are presented in the final chapters. Chapter 3 presents a study of the dissociative “hydrogen spillover” effect in the context of its viability as a practical hydrogen storage solution at room temperature. Chapters 4-5 deal with zeolite-templated carbon, an extremely high surface-area material which shows promise for hydrogen and methane storage

applications. Studies of hydrogen adsorption at high pressure (Chapter 4) and anomalous thermodynamic properties of methane adsorption (Chapter 5) on ZTCs are presented. The concluding chapter discusses the impact of and possible future directions for this work.

Contents

Nomenclature

Symbol	Description	Default Unit
t	time	s
P	pressure	MPa
T	temperature	K
V	volume	mL
R	gas constant	kJ K^{-1} mol^{-1}
n	molar number	mol
n_{ads}	molar number adsorbed	mol
n_e	specific excess (adsorption) uptake	mmol g^{-1}
n_a	specific absolute (adsorption) uptake	mmol g^{-1}
U	potential energy	kJ
F	Helmholtz free energy	kJ
G	Gibbs free energy	kJ
μ	chemical potential	kJ mol^{-1}
S	entropy	J K^{-1}
s	specific entropy	J mol^{-1} K^{-1}
H	enthalpy (of adsorption)	kJ
h	specific enthalpy (of adsorption)	kJ mol^{-1}
Δh	specific differential enthalpy (of adsorption)	kJ mol^{-1}
q_{st}	isosteric heat (of adsorption)	kJ mol^{-1}
n_{max}	adsorption scaling factor	mmol g^{-1}
α	weight factor	-
θ	Langmuir surface coverage	-
ρ	density	g mL^{-1}
V_a	volume of adsorbed molecule	$Å^3$
V_{ads}	specific volume of adsorption layer	mL g^{-1}
V_{max}	maximum specific volume of adsorption layer	mL g^{-1}
A	(surface) area	m^2
A_{BET}	specific BET surface area	m^2 g^{-1}
t_{ads}	thickness of adsorbed layer	Å
V_s	volume of solid sorbent	mL

Chapter 1

Mobile Energy

1.1 Introduction

The worldwide appetite for energy grows while energy-dense resources diminish and the threat posed by the negative environmental consequences of their use is no longer contested.[1] In particular, observations of increased levels of CO_2 in the Earth's atmosphere and a correlated rise in global temperatures since the advent of the widespread use of fossil fuels by humans has motivated the effort to reduce or eliminate the dependency on such fuels to fulfill future energy demands. At present, more than 80% of global energy consumption is met by burning fossil fuels,[2] primarily coal, oil, and natural gas, and their eventual physical depletion is certain. Total world consumption of energy will continue to increase, motivating the need to investigate alternative, sustainable means of energy transfer, use, and storage.

The two most impactful ways to effect a significant change to global carbon emissions are to 1) change the mobility fuel and 2) change the method of electricity generation.[3] Each accounts for ~40% of the total anthropogenic emission of CO_2 and the fuel of choice is highly segregated, mobility demands dominantly met by oil and

electricity generation dominantly by coal. In this work, we focus on mobility; a portable fuel system capable of providing energy on demand and in a nonpolluting manner is needed. The essential quality of an ideal mobility fuel is high energy density, but it must also meet other standards of availability, low cost, safety, and convenience of use.

Hydrogen is an ideal mobility fuel since it has the highest specific energy content of any chemical fuel, its constituent element (H) is highly abundant, it is readily synthesized by renewable methods, and it can be oxidized efficiently without the production of CO_2. However, numerous obstacles remain to realizing hydrogen as the primary mobility fuel beyond those associated with its inherent demands on infrastructure. Petroleum-based fossil fuels do not need to be synthesized, require relatively minor processing to be used, and are easily transported (due to their high volumetric energy density) whereas hydrogen must be synthesized and effectively stored, both steps that require substantial energy in themselves. Nonetheless, the superlative properties of hydrogen ensure that it will have importance in the global energy market in years to come.

1.2 Hydrogen and Energy

Hydrogen is the simplest and lightest element in the periodic table, is the most abundant element in the universe, and exhibits many unique properties due to its quantum-mechanical nature. Its liquid and solid state at ambient pressure are limited to very low temperature, a result of weak intermolecular forces. Supercritical hydrogen also exists at relatively low temperatures and pressures: above 33 K and 1.3 MPa (see Figure 1.1). At standard conditions, hydrogen is a near-ideal gas of diatomic molecules.

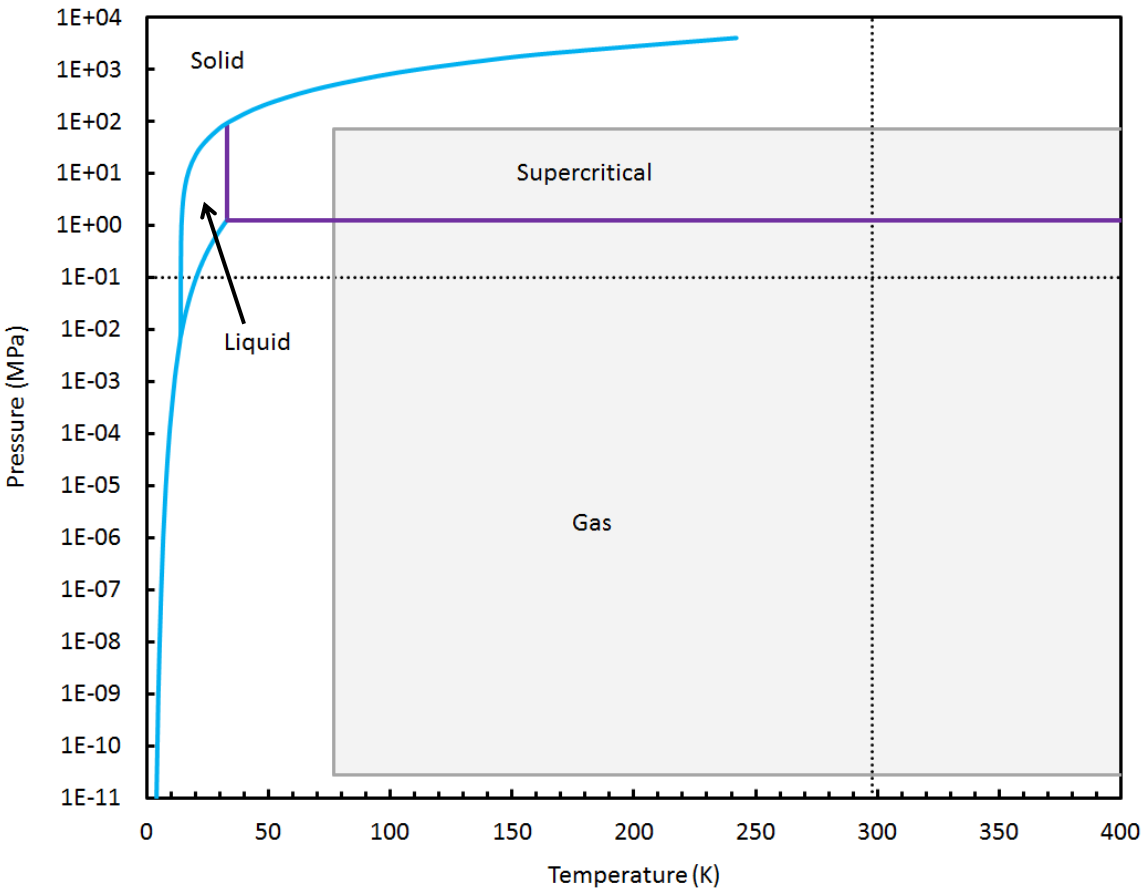

Figure 1.1. The phase diagram of hydrogen, calculated using REFPROP standard reference data. The equilibrium boundaries between the primary phases are shown: blue lines indicate the melting, boiling, and sublimation transitions and the purple lines indicate the boundary of the supercritical region. The dotted lines indicate standard conditions (0.1 MPa and 298 K) and the gray shaded region indicates the temperature and pressure limits of adsorption experiments in our laboratory.

Each molecule is bound by a single nonpolar covalent bond. While H_2 is not a particularly reactive molecule, H atoms will react with each other and all other elements (except noble gases); the H-H bond has a dissociation energy of +436 kJ mol^{-1} (dissociation is highly endothermic), and the heat of recombination leads to extremely high temperatures (e.g., 10^4 K during solar flares).[4] In the oxygen rich atmosphere on

Earth, it is practical to take advantage of a different reaction: the oxidation of molecular hydrogen to produce water:

$$H_{2\,(g)} + \frac{1}{2} O_{2\,(g)} \rightarrow H_2O_{(l)} \qquad \Delta H° = 141.8\ kJ\ (g\ H_2)^{-1}$$

Hydrogen has the highest gravimetric energy of any combustible species, a factor of three greater than gasoline (see Table 1.1). This chemical energy can be harnessed by thermal conversion to mechanical energy, such as in an internal combustion engine, or by electrochemical conversion to electrical energy, such as in a fuel cell. The latter method is not limited by Carnot efficiency, and typically reaches efficiencies twice that of traditional combustion. Using sunlight and a photovoltaic cell to drive the reverse reaction (electrolysis), the cycle of hydrogen production and consumption can be carried out entirely carbon-free.

A comparison of hydrogen's thermal energy properties with hydrocarbon fuels is given in Table 1.1. The standard enthalpy of combustion is also referred to as the "higher heating value" (HHV) since it represents the thermodynamic maximum energy that can be harnessed from combustion if all products are brought back to standard conditions after the reaction. It is more practical in engineering applications to assume that the water produced is not cooled back to 298 K, and the "lower heating value" (LLV) is a more accurate description of the energy gained in, for example, an internal combustion engine. In a fuel cell, the HHV is applicable. We also see the most obvious disadvantage of hydrogen as a fuel; gravimetric energy density is extraordinarily high, but the volumetric energy density of hydrogen is much lower than gasoline, even under conditions far from standard temperature and pressure (STP), due to its very low

density. In fact, the hydrogen content in liquid water or gasoline at STP is actually higher, per volume, than that found in pure liquid hydrogen at 20 K. This is an important caveat of hydrogen as an ideal fuel.

Table 1.1. Heat energy properties of hydrogen, methane, propane, and gasoline for engineering considerations.

Energy Carrier	ρ_{STP} (g L^{-1})	HHV (kJ g^{-1})	LHV (kJ g^{-1})	Volumetric HHV (MJ L^{-1})	
Hydrogen	0.0813	141.8	120	20 MPa, 298 K:	2.05
				80 MPa, 298 K:	6.09
				0.1 MPa, 20 K:	10.1
Methane	0.649	55.3	50	20 MPa, 298 K:	8.7
				80 MPa, 298 K:	17.8
Propane	1.809	48.9	46	0.95 MPa, 298 K:	24
Gasoline	~720	46.7	45	STP:	34

*standard state is defined as: T = 298 K, P = 0.1 MPa

The large heat of combustion of hydrogen has been known since well before liquid hydrocarbons were established as mainstream chemical energy carriers, and energy conversion technologies using hydrogen as a fuel have been pursued for over two centuries. For example, Figure 1.2 shows a large inflatable hydrogen storage container behind the Echo Mountain House, a remote (now defunct) mountain resort overlooking Pasadena, in 1893.[5] Hydrogen was used as a fuel for lighting and heating until it was replaced by electricity. Hydrogen was considered as an engine fuel for early vehicles as well, with the first known experiments carried out in 1820 by W. Cecil.[4] Some examples[6] of coal gas (containing hydrogen and other fuels) fuelled mobile vehicles are shown in Figure 1.3, predominantly used by civilians during World War I when petroleum-based

fuels were in high demand for the war effort. Hydrogen and coal gas vehicle experiments continued until approximately World War II when they were almost universally discarded in favor of the vastly denser energy available in liquid petroleum-based fuels. Liquid hydrogen-liquid oxygen mixtures became the primary propellant in chemical rocket engines starting in the 1960s and are still used today.

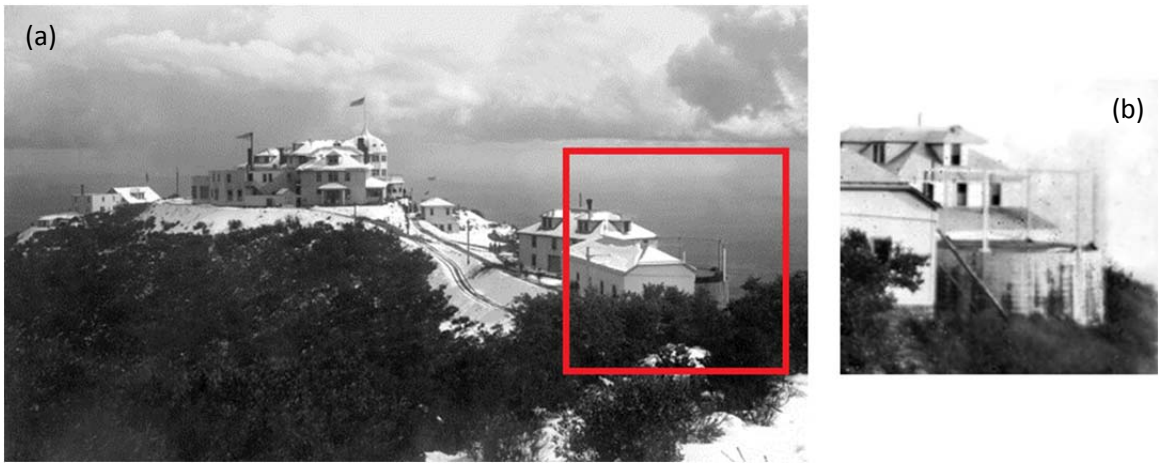

Figure 1.2. (a) The Echo Mountain House and Mt. Lowe Railway shown in 1893. An inflatable hydrogen storage container is shown in the red box. (b) A close-up view shows the framework used to support the gas reservoir which would expand upon filling.

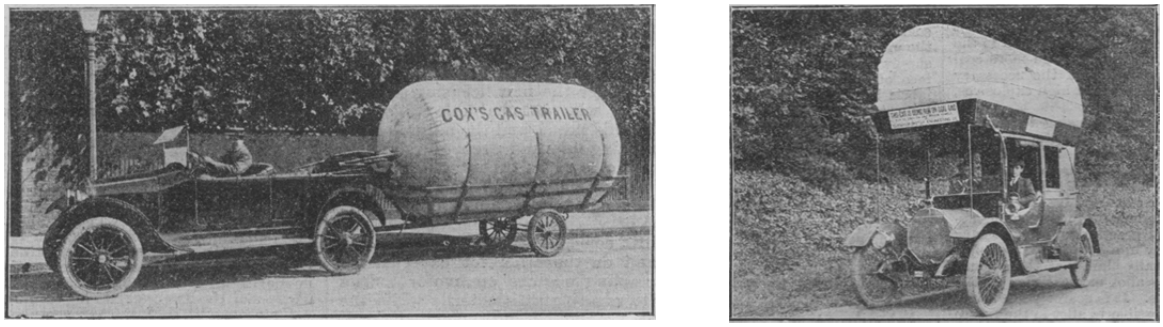

Figure 1.3. Early mobile vehicle gas storage concepts. On the left, ~6 cubic meters of coal gas is towed in a trailer to be used in the vehicle's internal combustion engine. The stated range of such a vehicle is ~20-30 km.

1.3 Methane and Energy

Energy density aside, hydrogen has another obstacle to achieving mainstream viability as a mobility fuel. Despite being the most abundant element in the universe, hydrogen on Earth is rarely found in pure molecular form, existing mainly in the form of water. Restoring molecular hydrogen via electrolysis is costly and itself the cause of significant carbon emission if the electricity used is generated in coal-burning power plants. A majority of the demand for hydrogen today is met by the steam reforming of natural gas, an economical method but one that inherently cannot take advantage of most of hydrogen's advantages over hydrocarbon fuels (carbon emission is still prevalent, though it is limited to the stationary location of the production facility rather than the remote location of the vehicle).

Until renewable hydrogen production is realized in a clean and economical way, other alternative fuels will maintain a significant role in the energy economy. Natural gas, the primary component of which is methane, is stated to be the premium fuel after hydrogen for numerous reasons.[7] While methane is itself a greenhouse gas (in fact 23 times more effective at trapping heat than CO_2[8]), it burns relatively cleanly, producing far less pollutant gases and particulate matter, and ~30% less CO_2 per unit energy than oil. Methane can also be derived by renewable means (referred to as biogas or biomethane) and is significantly more economical than producing longer-chain synthetic hydrocarbons.

Methane has a higher heating value of 55.3 kJ g^{-1}, the second highest (following hydrogen) of all chemical fuels. The phase diagram of methane is shown in Figure 1.4.

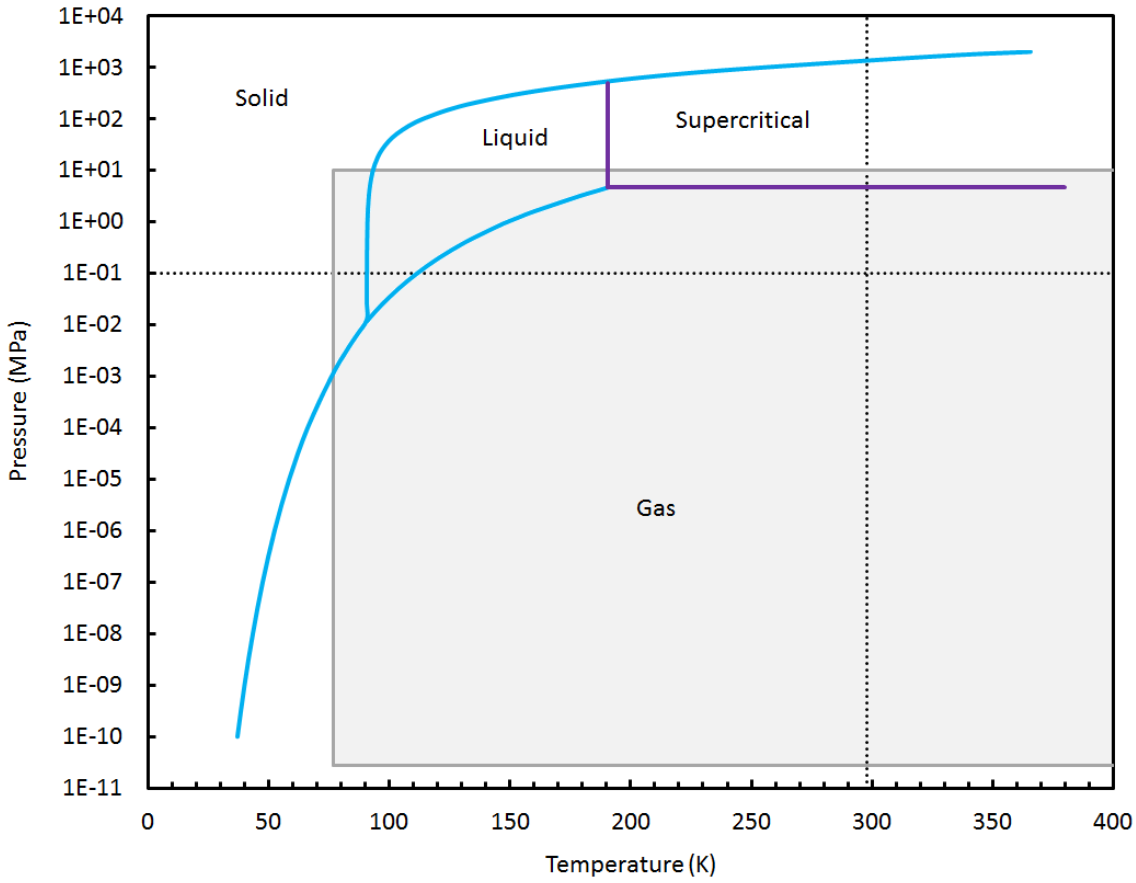

Figure 1.4. The phase diagram of methane. The equilibrium boundaries between the primary phases are shown: blue lines indicate the melting, boiling, and sublimation transitions and the purple lines indicate the boundary of the supercritical region. The dotted lines indicate ambient conditions (0.1 MPa and 298 K) and the gray shaded region represents the temperature and pressure limits of adsorption experiments in our laboratory.

Methane has significantly different properties than hydrogen, which can be observed from the shift of the phase boundaries nearer to the ambient regime. Strong interactions between methane molecules are responsible for this shift, and the gas is far from ideal within the pressure and temperature conditions applicable to storage. Thus, methane is interesting from both an engineering and fundamental science perspective.

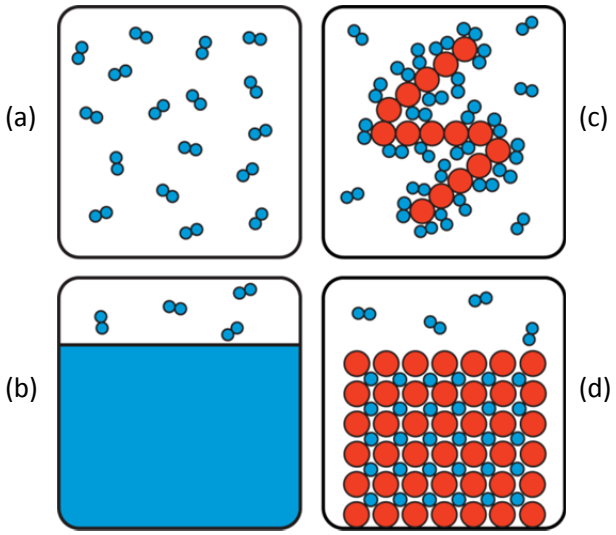

Figure 1.5. A schematic portraying four typical approaches to compact hydrogen storage: (a) pure gas compression, (b) liquefaction, (c) adsorption, and (d) absorption.

1.4 Hydrogen Storage

A serious obstacle to realizing a hydrogen-based energy economy is compact storage.[9] The problem is even more apparent for applications as a mobility fuel where volumetric energy density is of utmost importance. Numerous approaches for compact storage of hydrogen have been investigated (see Figure 1.5). As a pure substance, hydrogen can be contained as a gas or liquid (solidifying hydrogen is not considered a realistic storage approach). A secondary material, while adding mass to the system, can also be used to increase the volumetric density of hydrogen. Some metal hydrides reversibly store large amounts of hydrogen, chemically bound (*absorbed*) within their crystal structure, but generally suffer from poor kinetics and practicality is only achieved at elevated temperatures. Light-element hydrides such as $LiBH_4$ contain among the

highest gravimetric capacities of known materials, but hydrogen sorption is not fully reversible except under extreme conditions, and there are many complications to safety and practicality. There are many technologies being explored in these categories of storage materials and others such as complex hydrides. Hydrogen can also be effectively stored by *adsorption* on the surface of a material. For example, carbonaceous (i.e., predominantly carbon) sorbent materials are particularly attractive because they are lightweight, abundantly available, simple to produce, and can effectively increase the volumetric density of stored gases.[10-14] Another promising class of materials for adsorptive hydrogen storage is metal-organic frameworks (MOFs),[15, 16] which can achieve extremely high surface area and contain exposed metal sites which act as preferential adsorption sites at low pressure. Synthesis and characterization of MOFs as physisorptive storage materials is under active investigation, but is not the focus of this work. Representative isotherms of gas adsorption on a large variety of carbonaceous materials measured during the course of this thesis work are shown in Figure 1.6.

A main challenge for carbon (and other) adsorbent materials is that room temperature reversible hydrogen storage capacities are too low for effective use in mobile vehicle applications. Total system gravimetric capacities are better for pure compression than adsorptive compression except at very low temperatures; hydrogen adsorption at 77 K is a more promising solution, but requires significant additional system complexity to maintain such a low temperature. As compression containers achieve high strength to weight ratios, pure compression is favored over adsorption, but compaction of the adsorbent is a potential avenue favoring adsorption and could impart

significant improvement to volumetric capacities.[17] The complications associated with cryogenic containment temperatures and thermal management are also under assessment, but appear to be acceptable compared to other storage solutions. High-pressure hydrogen delivery is currently available to the public, for example up to 70 MPa, favoring pure compression storage as well as physisorption over other solutions.

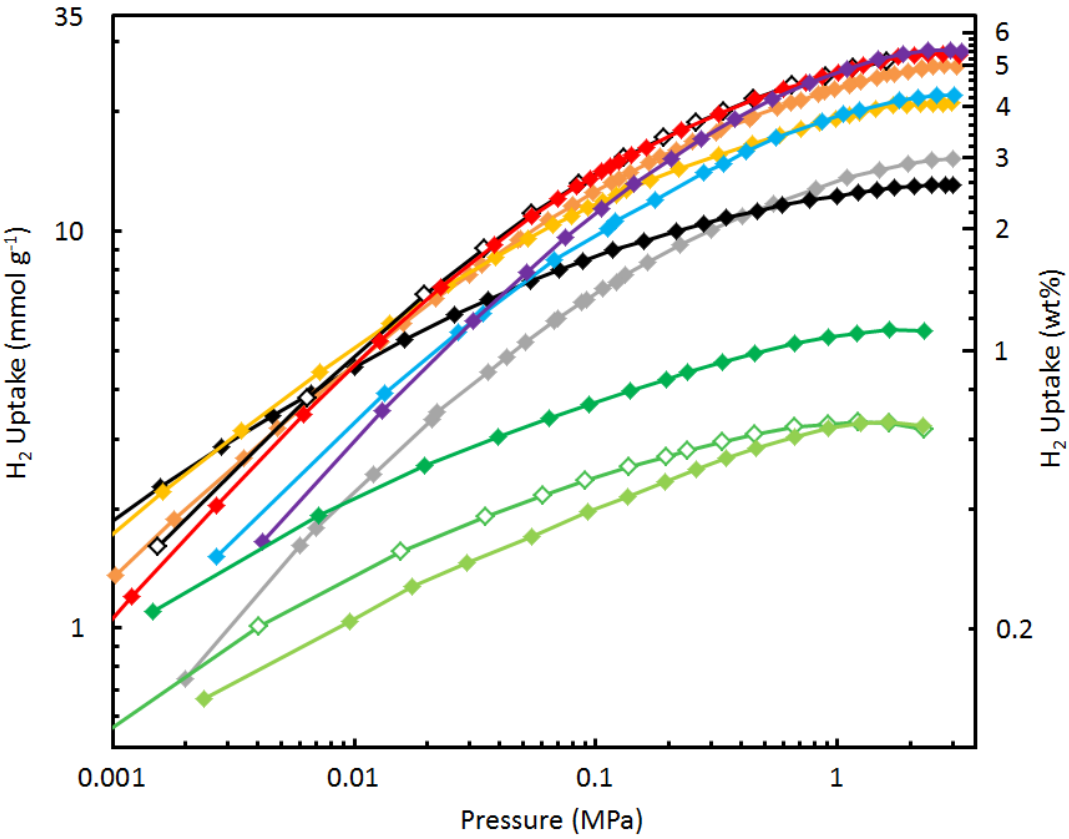

Figure 1.6. Equilibrium hydrogen adsorption isotherms (77 K) of a variety of carbonaceous samples measured during the present study:

Activated Carbon: (black) CNS-201, coconut shell-, (black, open) MU3K, corncob-, (yellow) CO2-9-60, PEEK-, (orange) CO2-9-80, PEEK-, (red) MSC-30, petroleum pitch-derived carbon

Aerogel Carbon: (gray) LLNL AD1

Templated Carbon: ZTC-2 (blue), ZTC-3 (purple)

Hetero-atom Substituted Carbon: (dark green) P-, (green, open) B-, (light green) N-doped carbon scaffolds

1.5 References

(1) R. A. Kerr, 'New greenhouse report puts down dissenters: an international panel assessing greenhouse warming pointedly denies the validity of objections raised by a prominent minority', *Science,* **249**, 481-482 (1990).

(2) REN21, 'Renewables 2012', *Global Status Report* (2012).

(3) A. B. Lovins, 'Profitable climate solutions: correcting the sign error', *Energy & Environmental Science,* **2**, 15-18 (2009).

(4) A. Züttel, A. Borgschulte, and L. Schlapbach, *Hydrogen as a future energy carrier*, Wiley-VCH GmbH & Co., Weinheim (2008).

(5) C. Seims, *Mount Lowe: the railway in the clouds*, Golden West Books (1976).

(6) H. M. Buist, 'Motor notes for medical men', *Brit. Med. J.*, 521-524 (1917).

(7) Y. Sun, C. Liu, W. Su, Y. Zhou, and L. Zhou, 'Principles of methane adsorption and natural gas storage', *Adsorption,* **15**, 133-137 (2009).

(8) U. H. Wiechert, 'Earth's early atmosphere', *Science,* **298**, 2341-2342 (2002).

(9) A. Züttel, 'Hydrogen storage methods', *Naturwissenschaften,* **91**, 157-172 (2004).

(10) N. D. Parkyns and D. F. Quinn, 'Natural gas adsorbed on carbon', *Porosity in carbons*, Edwards Arnold, London, 291-325 (1995).

(11) X. S. Chen, B. McEnaney, T. J. Mays, J. Alcaniz-Monge, d. Cazorla-Amoros, and A. Linares-Solano, 'Theoretical and experimental studies of methane adsorption on microporous carbons', *Carbon,* **35**, 1251-1258 (1997).

(12) E. Poirier, R. Chahine, and T. K. Bose, 'Hydrogen adsorption in carbon nanostructures', *Int. J. Hydrogen Energ.,* **26**, 831-835 (2001).

(13) B. Panella, M. Hirscher, and S. Roth, 'Hydrogen adsorption in different carbon nanostructures', *Carbon,* **43**, 2209-2214 (2005).

(14) M. Jordá-Beneyto, F. Suárez-García, D. Lozano-Castelló, D. Cazorla-Amorós, and A. Linares-Solano, 'Hydrogen storage on chemically activated carbons and carbon nanomaterials at high pressures', *Carbon,* **45**, 293-303 (2007).

(15) M. P. Suh, H. J. Park, T. K. Prasad, and D.-W. Lim, 'Hydrogen storage in metal-organic frameworks', *Chem. Rev.,* **112**, 782-835 (2011).

(16) D. J. Tranchemontagne, K. S. Park, H. Furukawa, J. Eckert, C. B. Knobler, and O. M. Yaghi, 'Hydrogen storage in new metal-organic frameworks', *J. Phys. Chem. C,* **116**, 13143-13151 (2012).

(17) J. Purewal, D. Liu, A. Sudik, M. Veenstra, J. Yang, S. Maurer, U. Müller, and D. J. Siegel, 'Improved hydrogen storage and thermal conductivity in high-density MOF-5 composites', *J. Phys. Chem. C,* **116**, 20199-20212 (2012).

Chapter 2

Physical Adsorption

> *The literature pertaining to the sorption of gases by solids is now so vast that it is impossible for any, except those who are specialists in the experimental technique, rightly to appraise the work, which has been done, or to understand the main theoretical problems which require elucidation.* – J. E. Lennard-Jones, 1932[1]

Adsorption is the phenomenon marked by an increase in density of a fluid near the surface, for our purposes, of a solid.* In the case of gas adsorption, this happens when molecules of the gas occasion to the vicinity of the surface and undergo an interaction with it, temporarily departing from the gas phase. Molecules in this new condensed phase formed at the surface remain for a period of time, and then return to the gas phase. The duration of this stay depends on the nature of the adsorbing surface and the adsorptive gas, the number of gas molecules that strike the surface and their kinetic energy (or collectively, their temperature), and other factors (such as capillary forces, surface heterogeneities, etc.). Adsorption is by nature a surface phenomenon, governed by the unique properties of bulk materials that exist only at the surface due to bonding deficiencies.

* Adsorption may also occur at the surface of a liquid, or even between two solids.

The sorbent surface may be thought of as a two-dimensional potential energy landscape, dotted with wells of varying depths corresponding to adsorption sites (a simplified representation is shown in Figure 2.1). A single gas molecule incident on the surface collides in one of two fundamental ways: elastically, where no energy is exchanged, or inelastically, where the gas molecule may gain or lose energy. In the former case, the molecule is likely to reflect back into the gas phase, the system remaining unchanged. If the molecule lacks the energy to escape the surface potential well, it becomes adsorbed for some time and later returns to the gas phase. Inelastic collisions are likelier to lead to adsorption. Shallow potential wells in this energy landscape correspond to weak interactions, for example by van der Waals forces, and the trapped molecule may diffuse from well to well across the surface before acquiring the energy to return to the gas phase. In other cases, deeper wells may exist which correspond to stronger interactions, as in chemical bonding where an activation energy is overcome and electrons are transferred between the surface and the adsorbed

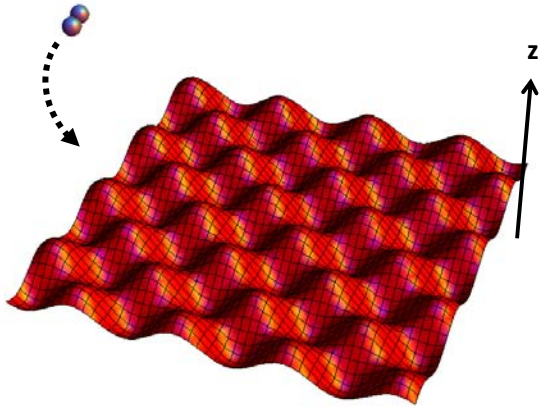

Figure 2.1. A potential energy landscape for adsorption of a diatomic molecule on a periodic two-dimensional surface. The depth of the energy well is shown in the z-axis.

molecule. This kind of well is harder to escape, the chemically bound molecule requiring a much greater increase in energy to return to the gas phase. In some systems, adsorption is accompanied by absorption, where the adsorbed species penetrates into the solid. This process is governed by the laws of diffusion, a much slower mechanism, and can be readily differentiated from adsorption by experimental means.

In the absence of chemical adsorption (chemisorption) and penetration into the bulk of the solid phase (absorption), only the weak physical adsorption (physisorption) case remains. The forces that bring about physisorption are predominantly the attractive "dispersion forces" (named so for their frequency dependent properties resembling optical dispersion) and short-range repulsive forces. In addition, electrostatic (Coulombic) forces are responsible for the adsorption of polar molecules, or by surfaces with a permanent dipole. Altogether, these forces are called "van der Waals forces," named after the Dutch physicist Johannes Diderik van der Waals.

2.1 Van der Waals Forces

An early and profoundly simple description of matter, the ideal law can be elegantly derived by myriad approaches, from kinetic theory to statistical mechanics. First stated by Émile Clapeyron in 1834, it combines Boyle's law (*PV* = constant) and Charles's law (stating the linear relationship between volume and temperature) and is commonly expressed in terms of Avogadro's number, *n*:

$$P\,V = n\,R\,T$$

Equation 2.1

This simple equation describes the macroscopic state of a three-dimensional gas of non-interacting, volumeless point particles. The gas constant, *R*, is the fundamental link between microscopic energy and macroscopic temperature. While satisfactory for describing common gases at low pressures and high temperatures, it is ineffective for real gases over a wide temperature and pressure regime. A better approximation was determined by van der Waals, combining two important observations:[2] a) the volume excluded by the finite size of real gas particles must be subtracted, and b) an attractive force between molecules effects a decreased pressure. The suggestion of an excluded real gas volume was made earlier by Bernoulli and Herapath, and confirmed experimentally by Henri Victor Regnault, but the attractive interactions between molecules was the important contribution by van der Waals. The change in pressure due to intermolecular forces is taken to be proportional to the square of the molecular density, giving the van der Waals equation of state:

$$\left(P + a\frac{n^2}{V^2}\right)(V - n\,b) = n\,R\,T$$

Equation 2.2

At the time, van der Waals was adamant that no repulsive forces existed between what he reasoned were “hard sphere” gas particles. Interestingly, it was James Clerk Maxwell who completed and popularized van der Waals’ (then obscure) work in *Nature*[3] and also who later correctly supposed that molecules do not in fact have a “hard sphere” nature. Nevertheless, the sum of the attractive and repulsive forces between atoms or molecules are now collectively referred to as “van der Waals forces.” Forces

between any electrically neutral atoms or molecules (thereby excluding covalent, ionic, and hydrogen bonding) conventionally fall into this category. Together, these include: Keesom forces (between permanent multipoles), Debye forces (between a permanent multipole and an induced multipole), London dispersion forces (between two induced multipoles), and the Pauli repulsive force.

2.1.1 Intermolecular Potentials

In his time, the range of van der Waals' attractive interaction was predicted to be of molecular scale but the form of the potential as a function of distance, $U(r)$, was unknown. There was unified acceptance that the attraction potential fell off with distance as $r^{-\eta}$, with $\eta > 2$ (the value for that of gravitation), but the value of η was actively debated.

In parallel with the effort to determine this potential, a noteworthy advance in the general description of equation of state was the "virial expansion" by H. K. Onnes:[4]

$$\frac{P\,V}{n\,R\,T} = 1 + \frac{B(T)}{V} + \frac{C(T)}{V^2} + \frac{D(T)}{V^3} + \cdots$$

Equation 2.3

Perhaps most importantly, this description signified a realization of the unlikelihood that all gases could be accurately described by a simple closed form of equation. Additionally, the second virial coefficient, $B(T)$, by its nature a first-neighbor term of interaction, sheds insight on the attractive potential between molecules. A major breakthrough followed, culminating in the theory now attributed to Sir John Edward Lennard-Jones, an English theoretical physicist. His description of the potential energy

between two interacting non-polar molecules used η = 6 and a repulsive term of order 12:[5, 6]

$$U(r) = -\left(\frac{C_1}{r}\right)^6 + \left(\frac{C_2}{r}\right)^{12}$$

Equation 2.4

The result constitutes a balance between the longer range attractive van der Waals potential (of order r^{-6}) with the short-range repulsive potential arising from electron orbital overlap (of order r^{-12}), described by the Pauli exclusion principle, and is also referred to as a 6-12 potential. It approximates empirical data for simple systems with gratifying accuracy, and has the added advantage that it is computationally efficient since r^{-12} is easily calculated as r^{-6} squared, an important consideration in its time. A representative plot of this potential is shown in Figure 2.2.

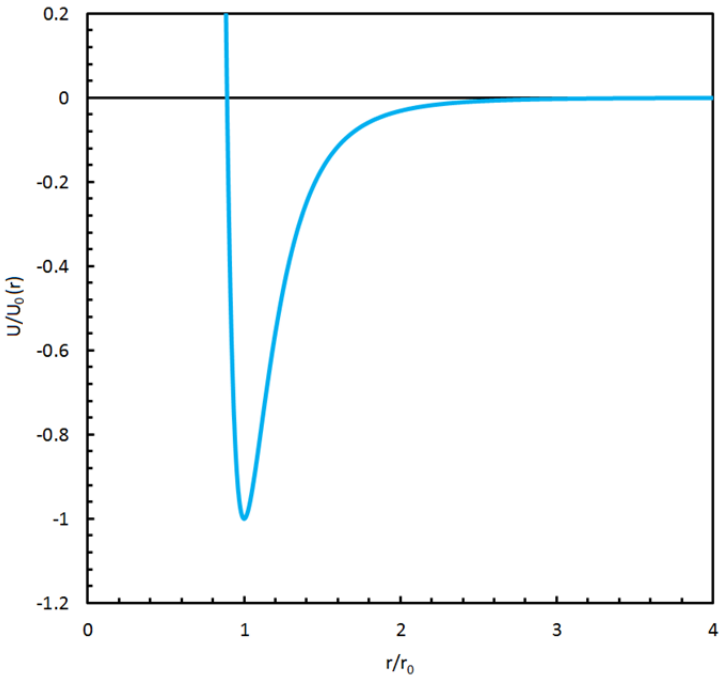

Figure 2.2. The Lennard-Jones 6-12 potential, scaled in units of U_0, the depth of the well. The equilibrium distance between the interacting species is $r = r_0$.

At far distances ($r >> r_0$), the magnitude of the interaction potential is negligible. If the species become spontaneously closer together (e.g., as the result of random collision), it is favorable for them to remain at a specific distance apart, namely $r = r_0$. At very short distance, the Pauli repulsion term dominates and the system is unfavorable.

A number of similar potential forms arose shortly afterward (using various forms for the Pauli repulsion term such as an exponential or other power of order near 12), and an early triumph of these models was accurately fitting the second virial coefficient of simple gases, such as helium for which the equilibrium He-He distance was calculated to be r_0 = 2.9 Å in 1931. This value remains accurate within 2% today.

Coincidentally, Lennard-Jones' work was originally undertaken to attempt to explain a puzzling observation made during volumetric adsorption measurements of hydrogen on nickel,[7, 8] showing two distinct characteristic binding potentials associated with different temperature regimes. This would lead to the first explanation of the differentiable nature of adsorption at low and high temperature (now referred to separately as physisorption and chemisorption, respectively). As a result of its success, the Lennard-Jones inverse seventh-power force (from the inverse sixth-power potential) became the backbone of adsorption theory.

2.1.2 Dispersion Forces

The $-r^{-6}$ Lennard-Jones potential was derived from first-principles and first explained correctly by the German physicist Fritz London;[9, 10] hence, the attractive force that occurs between neutral, non-polar molecules is called the "London dispersion force." It is a weak, long-range, non-specific intermolecular interaction arising from the induced

polarization between two species, resulting in the formation of instantaneous electrical multipole moments that attract each other. Arising by rapid, quantum induced fluctuations of the electron density within a molecule or atom (the reason they were coined as “dispersive” forces by London), the force is stronger between larger species due to those species’ increased polarizability. The key to the correct explanation of dispersion forces is in quantum mechanics; without the uncertainty principle (and the fundamental quantum-mechanical property of zero-point energy), two spherically symmetric species with no permanent multipole could not influence a force on each other and would remain in their classical rest position. The subject of dispersion forces is important to many fields, and a thorough overview of their modern theory can be found elsewhere.[11]

The physisorption of nonpolar molecules or atoms on a nonpolar surface (as well as their liquefaction) occurs exclusively by dispersion forces. Dispersion forces are also essential for explaining the total attractive forces between multipolar molecules (e.g., H_2) for which typical static models of intermolecular forces (e.g., Keesom or Debye forces) account for only a fraction of the actual attractive force. The existence of “noble liquids” (liquefied noble gases) is a fundamental verification of dispersion forces since there is no other attractive intermolecular force between noble gas atoms that could otherwise explain their condensation.

2.1.3 Modern Theory of Physical Adsorption

Despite their correct explanation over 80 years ago, dispersion forces are not well simulated by typical computational methods, such as density-functional theory which

cannot accurately treat long-range interactions in weakly bound systems.[12] The first-principles methods that are dependable are computationally intensive and are often foregone for empirical potentials such as a Lennard-Jones potential as described in the previous section.[13, 14] For this reason, the ab-initio guidance of the design of physisorptive materials has been much less than that for chemisorptive materials, and was not a component of the work described in this thesis.

2.2 Gas-Solid Adsorption Models

A thermodynamic understanding of adsorption can be achieved by describing a simplified system, and a small subset of important models will be discussed. The constituent chemical species of the simplest system are a pure solid, indexed as *s*, and a single-component adsorptive gas, indexed as *a* in the adsorbed phase, *g* in the gas phase, or *x* if it is ambiguous. The system is held at fixed temperature and pressure. We start with the following description:

(i) the adsorptive density, ρ_x, is zero within and up to the surface of a material,

(ii) at the material surface and beyond, ρ_x is an unknown function of *r*, the distance from the surface, and

(iii) at distance from the surface, ρ_x is equal to the bulk gas density, ρ_g.

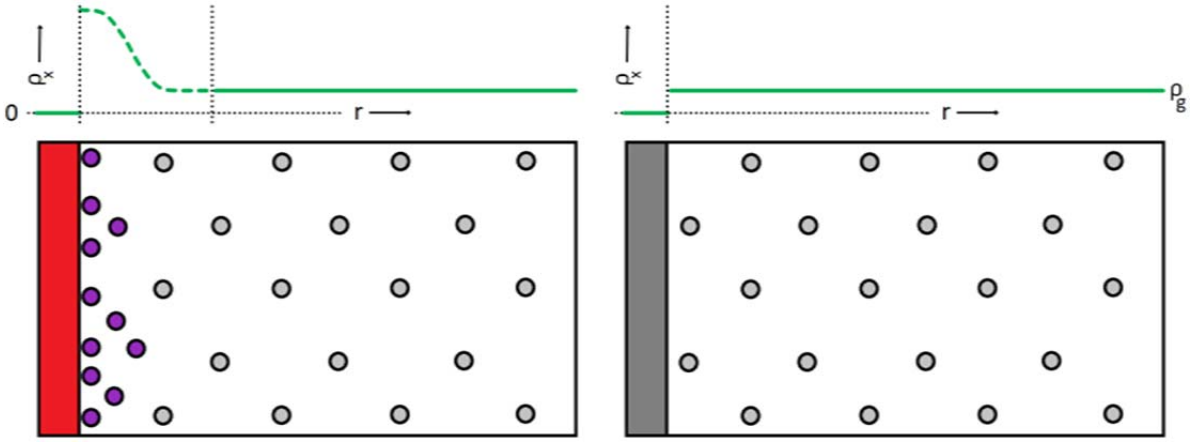

Figure 2.3. A simplified representation of a gas-solid adsorption system (left) and a non-adsorbing reference system of the same volume (right). Adsorptive density (green) is plotted as a function of *r*.

A schematic of this system is shown in Figure 2.3 (left). The functional form of the densification at the sorbent surface, and the thickness of the adsorption layer are not precisely known. However, the adsorbed amount can be defined as the quantity existing in much higher density near the surface, and is easily discerned when compared to the reference case of a non-adsorptive container, shown in Figure 2.3 (right). We may assume that the gas pressure, P_g, is equal to the total hydrostatic pressure, P, of the system at equilibrium, which is consistent with ordinary experimental conditions.

2.2.1 Monolayer Adsorption

The simplest representation of an adsorbed phase is as an ideal gas, constrained to a two-dimensional monolayer where there is no interaction between adsorbed molecules:

$$P_a \, A_a = n_a \, R \, T$$

Equation 2.5

Here, P_a is the spreading pressure of the adsorption layer and A_a is its area of coverage. In the system described, the surface area for adsorption is fixed, as well as the temperature. If we take the spreading pressure as proportional to that of the gas phase in equilibrium with it, we find that the amount adsorbed is a linear function of pressure:

$$n_a = \frac{P_a \, A_a}{R \, T} = \frac{c \, P \, A_a}{R \, T} = k_H \, P$$

Equation 2.6

This relationship, called Henry's law, is the simplest description of adsorption, and applies to systems at low relative occupancy. When occupancy increases, the relationship between the pressures of the adsorbed phase and the gas phase becomes unknown, and a more general treatment is necessary.

A first approximation of an imperfect two-dimensional gas may be made by adapting the van der Waals equation of state to two dimensions:

$$\left(P_a + a\frac{{n_a}^2}{{A_a}^2}\right)(A_a - n_a\, b) = n_a\, R\, T$$

Equation 2.7

For simplicity, it is convenient to define a fractional coverage of the surface available for adsorption, θ, as the number of adsorbed molecules per surface site, a unitless fraction that can also be expressed in terms of relative surface area:

$$\theta = \frac{n_a}{n_{sites}} = A_{site}\frac{n_a}{A_a}$$

Equation 2.8

With this definition, and a more elegant description of the spreading pressure of the van der Waals two-dimensional phase, the Hill-de Boer equation is derived:

$$P = \frac{\theta}{k_H\,(1-\theta)}\; e^{\left(\frac{\theta}{(1-\theta)} - k_2\theta\right)}$$

Equation 2.9

This equation has been shown to be accurate for certain systems, up to a maximum coverage of θ = 0.5.[15] Ultimately though, treatment of the adsorbed phase without reference to its interaction with the surface encounters difficulties.

A more insightful approach is to treat adsorption and desorption as kinetic processes dependent on an interaction potential with the surface, also seen as an energy of adsorption. In dynamic equilibrium, the exchange of mass between the adsorption layer and the bulk gas phase can be treated by kinetic theory; at a fixed pressure, the rate of

adsorption and desorption will be equal, resulting in an equilibrium monolayer coverage. This equilibrium can be described by the following scheme:

$$X_g + empty\ site \leftrightarrow X_a$$

The rate (where adsorption is taken to be an elementary reaction) is given by the (mathematical) product of the concentrations of the reactants, c_i, and a reaction constant, $K(T)$:

$$r_{ads} = K_{ads}\, c_g\, c_{empty\ site}$$

Equation 2.10

Correspondingly, for the reverse (desorption) reaction:

$$r_{des} = K_{des}\, c_a$$

Equation 2.11

We can assume that the number of adsorption sites is fixed, so the concentration of adsorbed molecules and empty adsorption sites is complementary. To satisfy equilibrium, we set Equations 2.10 and 2.11 equal and express them in terms of the fractional occupancy, recognized as equivalent to c_a:

$$r_{eq} = r_a = K_{ads}\, c_g\, (1 - \theta) = r_d = K_{des}\, \theta$$

$$\theta = \frac{K_{ads}\, c_g}{K_{des} + K_{ads}\, c_g} = \frac{\frac{K_{ads}}{K_{des}} c_g}{1 + \frac{K_{ads}}{K_{des}} c_g}$$

Equation 2.12

To express the temperature dependence of the reaction constants, we can use an Arrhenius-type equation:

$$K_i = \frac{A_i}{\sqrt{T}}\, e^{\left(\frac{-E_i}{RT}\right)}$$

Equation 2.13

The ratio of the adsorption and desorption constants is:

$$K = \frac{K_{ads}}{K_{des}} = \frac{A_{ads}}{A_{des}}\, e^{\left(\frac{E_g - E_a}{RT}\right)} = A\, e^{\left(\frac{-\Delta E}{RT}\right)}$$

If the gas phase is assumed to be ideal, its concentration is proportional to pressure, P. Secondly, if we assume that the energy of the adsorbed molecule, E_a, is the same at every site, and the change in energy upon adsorption, ΔE, is independent of surface coverage, the result is Langmuir's isotherm equation:

$$\theta = \frac{KP}{1 + KP}$$

Equation 2.14

The Langmuir isotherm, in the context of its inherent assumptions, is applicable over the entire range of θ. Plots of multiple Langmuir isotherms with varying energies of adsorption are shown in Figure 2.4 (right). In the limit of low pressure, the Langmuir isotherm is equivalent to Henry's law:

$$\lim_{P \to 0} \frac{KP}{1 + KP} = \frac{KP}{1} = KP$$

Equation 2.15

The plots in Figure 2.4 show the temperature and energy dependence of the Langmuir isotherm equation. With increasing temperature, the Henry's law region is marked by more gradual uptake, a similar trend as for decreasing energy of adsorption; both trends are consistent with experiment (in systems referred to as exhibiting type-I isotherms).

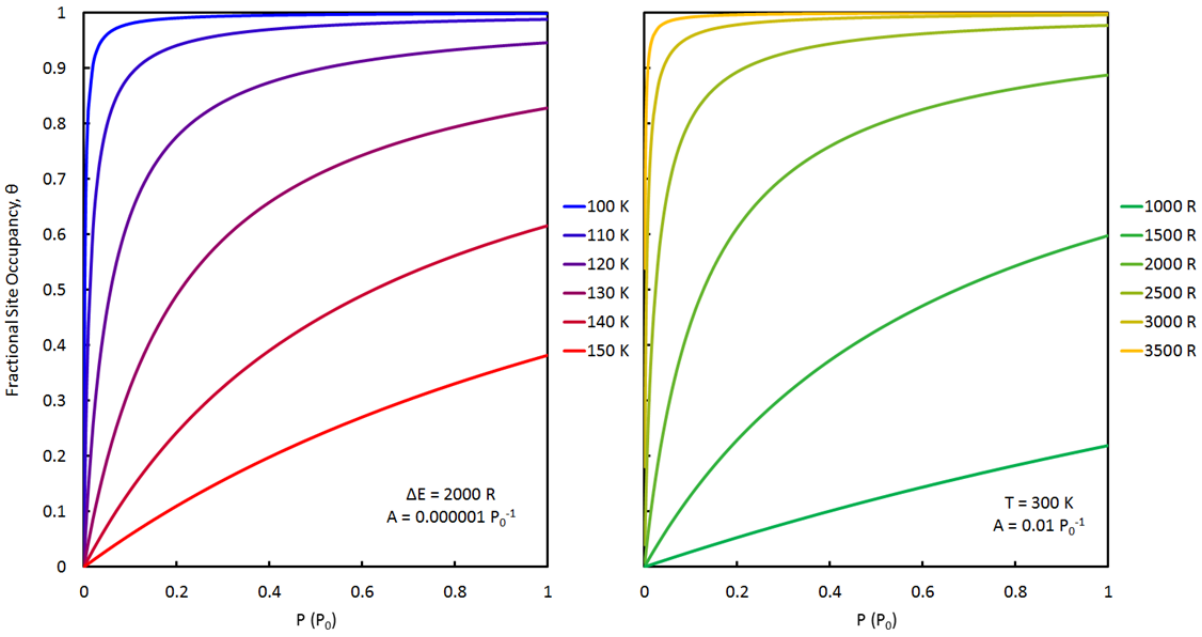

Figure 2.4. Langmuir isotherms showing the dependence of adsorption site occupancy with pressure, varying temperature (left) and energy of adsorption (right).

Although it enjoys quantitative success in characterizing adsorption in limited ranges of pressure for certain systems, conformity of experimental systems to the Langmuir equation is not predictable, and does not necessarily coincide with known properties of the system (such as expected homogeneity of adsorption sites, or known adsorbate-adsorbate interactions).[16] No system has been found which can be characterized by a single Langmuir equation with satisfactory accuracy across an arbitrary range of pressure and temperature.[15] Langmuir's model assumes: 1) the adsorption sites are identical, 2) the energy of adsorption is independent of site occupancy, and 3) both the two- and three-dimensional phases of the adsorptive are well approximated as ideal gases. Numerous methods have been suggested to modify the Langmuir model to generalize its assumptions for application to real systems.

For heterogeneous surfaces with a distribution of adsorption sites of different characteristic energies, one possibility is to superimpose a set of Langmuir equations, each corresponding to a different type of site. This generalized-Langmuir equation can be written as:

$$\theta = \sum_i \alpha_i \left(\frac{K_i P}{1 + K_i P}\right)$$

$$\sum_i \alpha_i = 1$$

Equation 2.16

The weight of each component isotherm, α_i, corresponds to the fraction of sites with the energy E_i. This form of Langmuir's equation is applicable across a wide range of experimental systems, and can lend insight into the heterogeneity of the adsorbent surface and the range of its characteristic binging energies. Its treatment of adsorption sites as belonging to a two-dimensional "monolayer" can be made completely general; the adsorption layer can be understood as any set of equally accessible sites within the adsorption volume, assuming the volume of gas remains constant as site occupancy increases (an assumption that is valid when $\rho_a >> \rho_g$). The application of this equation for high-pressure adsorption in microporous materials is discussed in Section 2.4.6.

2.2.2 Multilayer Adsorption

A practical shortcoming of Langmuir's model is in determining the surface area available for adsorption. Typically, fitting experimental adsorption data to a Langmuir equation results in an overestimation of the surface area.[16] The tendency of experimental isotherms toward a non-zero slope in the region beyond the "knee" indicates that

adsorption occurs in two distinct phases: a primary phase, presumably adsorption on homogeneous adsorption sites at the sorbent surface, and a secondary phase corresponding to adsorption in layers beyond the surface of the adsorbent.

An adaptation of Langmuir's model can be made which accounts for multiple, distinct layers of adsorption. A characteristic of adsorption in a multilayer system is that each layer corresponds to a different effective surface, and thus a different energy of adsorption. The distinction between the multilayer class of systems and a generalized-monolayer system (such as in Equation 2.16) lies in the description of the adsorbent surface; even a perfectly homogeneous surface *is* susceptible to a multiple layers of adsorption, an important consideration at temperatures and pressures near the saturation point. Brunauer, Emmett, and Teller successfully adapted the Langmuir model to multilayer adsorption by introducing a number of simplifying assumptions.[17] Most importantly, 1) the second, third, and i^{th} layers have the same energy of adsorption, notably that of liquefaction, and 2) the number of layers as the pressure approaches the saturation pressure, P_0, tends to infinity and the adsorbed phase becomes a liquid. Their equation, called the BET equation, can be derived by extending Equation 2.12 to i layers, where the rate of evaporation and condensation between adjacent layers is set equal. Their summation leads to a simple result:

$$\theta = \frac{c_{BET}\ \frac{P}{P_0}}{\left(1-\frac{P}{P_0}\right)\left(1-\frac{P}{P_0}+c_{BET}\ \frac{P}{P_0}\right)}$$

Equation 2.17

If the Arrhenius pre-exponential factors A_1/A_2 and A_2/A_l (from Equation 2.13) are approximately equal, a typical assumption,[16] the parameter c_{BET} can be written:

$$c_{BET} = e^{\frac{(\Delta E_1 - \Delta E_l)}{RT}}$$

Equation 2.18

The change in energy upon adsorption in any of the layers beyond the surface layer is taken as the energy of liquefaction, and the difference in the exponent in Equation 2.18 is referred to as the net molar energy of adsorption. Strictly within BET theory, no allowance is made for adsorbate-adsorbate interactions or different adsorption energies at the surface, assumptions that prevent the BET model from being applied to general systems and across large pressure ranges of adsorption.

The BET equation was specifically developed for characterizing adsorption in a gas-solid system near the saturation point of the adsorptive gas for the practical purpose of determining the surface area of the solid adsorbent. Despite its narrow set of defining assumptions, its applicability to experimental systems is remarkably widespread. As a result, it is the most widely applied of all adsorption models, even for systems with known insufficiencies to meet the required assumptions. Nitrogen adsorption at 77 K up to P_0 = 101 kPa has become an essential characterization technique for porous materials, and the BET model is commonly applied to determine the surface available for adsorption, called the BET surface area. Even for microporous adsorbents where the BET assumptions are highly inadequate, this is the most common method for determination of specific surface area, and its deficiencies are typically assumed to be similar between comparable materials.

The BET surface area of a material can be determined by fitting experimental adsorption data to Equation 2.17 and determining the monolayer capacity, n_{sites}. Typically, N_2 adsorption data are plotted in the form of the linearized-BET equation, a rearrangement of Equation 2.17:

$$\frac{n_a}{n_{sites}} = \frac{c_{BET}\ \frac{P}{P_0}}{\left(1-\frac{P}{P_0}\right)\left(1-\frac{P}{P_0}+c_{BET}\ \frac{P}{P_0}\right)}$$

$$B_{BET} = \frac{\frac{P}{P_0}}{n_a\left(1-\frac{P}{P_0}\right)} = \frac{\left(1-\frac{P}{P_0}-c_{BET}\ \frac{P}{P_0}\right)}{c_{BET}\ n_{sites}} = \frac{1}{c_{BET}\ n_{sites}} + \frac{c_{BET}-1}{c_{BET}\ n_{sites}}\frac{P}{P_0}$$

Equation 2.19

The BET variable, B_{BET}, is plotted as a function of P/P_0 and if the data are satisfyingly linear, the slope and intercept are used to determine n_{sites} which is proportional to the surface area as stated in Equation 2.8 (using A_{sites} = 16.2 Å^2)[16]. In practice, the linearity of the BET plot of a nitrogen isotherm at 77 K may be limited to a small range of partial pressure. An accepted strategy is to fit the low-pressure data up to and including a point referred to as "point B," the end of the characteristic knee and the start of the linear region in a Type II isotherm.[15, 16]

2.2.3 Pore-Filling Models

The Langmuir model, and its successive adaptations, were developed in reference to an idealized surface which did not have any considerations for microstructure, such as the presence of narrow micropores, which significantly change the justifiability of the assumptions of monolayer and multilayer adsorption. While numerous advances have

been made in adsorption theory since the BET model, a notable contribution was by Dubinin and collaborators to develop a pore-filling theory of adsorption. Their success at overcoming the inadequacies of layer theories at explaining nitrogen adsorption in highly microporous media, especially activated carbons, is highly relevant. The Dubinin-Radushkevich (DR) equation, describing the fractional pore occupancy θ_{pore}, is stated as:

$$\theta_{pore} = \frac{\mathrm{W}}{\mathrm{W}_0} = \mathrm{e}^{\left(-B\left(\frac{T}{\beta}\right)^2 \log^2\left(\frac{P}{P_0}\right)\right)}$$

Equation 2.20

The DR equation can be used for determining DR micropore volume, W_0, in an analogous way as the Langmuir or BET equation for determining surface area. Its similarities to BET analyses are discussed in Appendix D.

2.2.4 Gibbs Surface Excess

Measurements of adsorption near or above the critical point, either by volumetric (successive gas expansions into an accurately known volume containing the adsorbent) or gravimetric (gas expansions into an enclosed microbalance containing the adsorbent) methods, have the simple shortcoming that they cannot directly determine the adsorbed amount. This is readily apparent at high pressures where it is observed that the measured uptake amount increases up to a maximum and then decreases with increasing pressure. This is fundamentally inconsistent with the Langmuir model of adsorption, which predicts a monotonically increasing adsorption quantity as a function of pressure. The reason for the discrepancy can be traced to the finite volume of the adsorbed phase, shown in Figure 2.3. The "free gas" volume displaced by the adsorbed phase would have contained an amount of gas given by the bulk gas density even in the absence of adsorption. Therefore, this amount is necessarily excluded from the measured adsorption amount since the gas density, measured remotely, must be subtracted from in the entire void volume, such that adsorption is zero in the "reference state" which does not have any adsorption surface.

In the landmark paper of early thermodynamics, O*n the Equilibrium of Heterogeneous Substances*,[18] Josiah Willard Gibbs gave a simple geometrical explanation of the excess quantity adsorbed at the interface between two bulk phases, summarized for the gas-solid case in Figure 2.5. The absolute adsorbed amount, shown in purple, is subdivided into two constituents: *reference* molecules shown in light blue, existing within the adsorbed layer but corresponding to the density of the bulk gas far

from the surface, and *excess* molecules shown in dark blue, the measured quantity of adsorption. The Gibbs definition of excess adsorption, n_e, as a function of absolute adsorption, n_a , is:

$$n_e = n_a - V_{ads}\,\rho(P,T)$$

Equation 2.21

Any measurement of gas density far from the surface cannot account for the existence of the reference molecules near the surface; these would be present in the reference system. The excess quantity, the amount in the densified layer that is in excess of the bulk gas density, is the experimentally accessible value. It is simple to show that the excess uptake is approximately equal to the absolute quantity at low pressures. As the bulk gas density increases, the difference between excess and absolute adsorption increases. A state may be reached at high pressure, P_3 in Figure 2.5, where the increase in adsorption density is equal to the increase in bulk gas density, and thus the excess quantity reaches a maximum. This point is referred to as the Gibbs excess maximum. Beyond this pressure, the excess quantity may plateau or decline, a phenomenon readily apparent in the high-pressure data presented in this thesis.

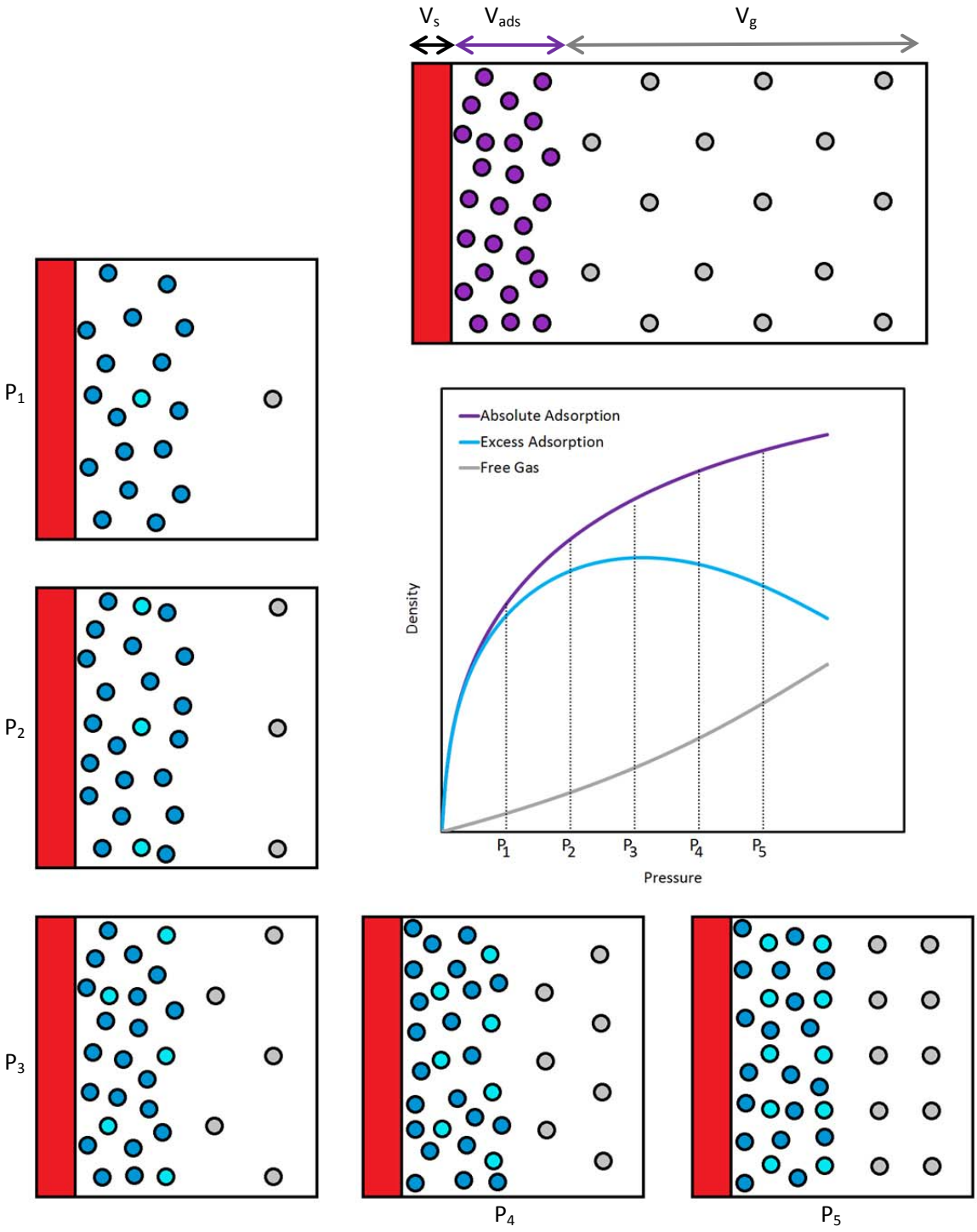

Figure 2.5. The Gibbs excess adsorption is plotted as a function of pressure (center). A microscopic representation of the excess (light blue), reference (dark blue), and absolute (combined) quantities is shown at five pressures, P_1-P_5. The bulk gas density (gray) is a function of the pressure, and depicted as a regular pattern for clarity. The volume of the adsorbed phase, unknown experimentally, is shown in purple (top).

2.3 Adsorption Thermodynamics

2.3.1 Gibbs Free Energy

Adsorption is a spontaneous process and must therefore be characterized by a decrease in the total free energy of the system. When a gas molecule (or atom) is adsorbed on a surface, it transitions from the free gas (with three degrees of translational freedom) to the adsorbed film (with two degrees of translational freedom) and therefore loses translational entropy. Unless the adsorbed state is characterized by a very large additional entropy (perhaps from vibrations), it follows that adsorption must always be exothermic ($\Delta H_{ads} < 0$) since:

$$\Delta G_{ads} = \Delta H_{ads} - T\Delta S_{ads} < 0$$

$$\Delta H_{ads} = H_a - H_g$$

Equation 2.22

We refer to the Gibbs free energy, *G*, since it governs thermodynamic systems at constant temperature and pressure, the variables held constant during equilibrium gas adsorption measurements. The chemical potential in each phase is defined as:

$$\mu_a = \left(\frac{\partial G_a}{\partial n_a}\right)_{T,P}$$

$$\mu_g = \left(\frac{\partial G_g}{\partial n_g}\right)_{T,P}$$

Equation 2.23

We have assumed that the thermodynamic properties of the solid surface remain unchanged upon adsorption, an approximation that serves us well for this purpose. Let us assume that the system is held in a constant temperature bath, and we have

instantaneously adjusted the pressure of the system at a location remote to the adsorbent surface by adding dn_g molecules of gas. The adsorbed phase and the bulk gas phase are not in equilibrium, and will proceed to transfer matter in the direction of lower free energy, resulting in adsorption. When equilibrium is reached, the chemical potential of the gas phase and the adsorbed phase are equal, since:

$$dG = (\mu_a - \mu_g) dn_a = 0$$

$$\mu_a = \mu_g$$

Equation 2.24

Determining the change in chemical potential, or the Gibbs free energy, of the adsorptive species as the system evolves toward equilibrium is essential to a fundamental understanding of adsorptive systems for energy storage or other engineering applications. We develop this understanding through the experimentally accessible components of the Gibbs free energy: ΔH_{ads} and ΔS_{ads}.

2.3.2 Entropy of Adsorption

We take the total derivative of both sides of Equation 2.24, and rearrange to arrive at the classic Clausius-Clapeyron relation:

$$-s_a dT + v_a dP = -s_g dT + v_g dP$$

$$\frac{dP}{dT} = \frac{(s_g - s_a)}{(v_g - v_a)}$$

Equation 2.25

where:

$$s_i = \left(\frac{\partial S}{\partial n_i}\right)_{T,P} \quad v_i = \left(\frac{\partial V}{\partial n_i}\right)_{T,P}$$

The specific volume of the free gas is usually much greater than that of the adsorbed gas, and a robust[19] approximation simplifies the relation:

$$v_g - v_a \approx v_g$$

Equation 2.26

$$\frac{dP}{dT} = \frac{(s_g - s_a)}{v_g} = -(s_a - s_g)\,\rho_g$$

We rearrange to derive the common equation for change in entropy upon adsorption:

$$\Delta S_{ads}(n_a) = -\left(\frac{dP}{dT}\right)_{n_a} {\rho_g}^{-1}$$

Equation 2.27

2.3.3 Enthalpy of Adsorption

At equilibrium, the corresponding change in enthalpy upon adsorption is:

$$\Delta H_{ads}(n_a) = T\,\Delta S_{ads} = -T\left(\frac{dP}{dT}\right)_{n_a} {\rho_g}^{-1}$$

Equation 2.28

We refer to this as the "common" enthalpy of adsorption. To simplify further, we must specify the equation of state of the bulk gas phase. The ideal gas law is commonly used, a suitable equation of state in limited temperature and pressure regimes for typical gases (the limitations of which are investigated in Section 2.4.1). For an ideal gas:

$$\rho_g = \frac{n_g}{V_g} = \frac{P}{R\,T}$$

$$\Delta H_{ads}(n_a) = -T\left(\frac{dP}{dT}\right)_{n_a} \frac{R\,T}{P} = -\frac{R\,T^2}{P}\left(\frac{dP}{dT}\right)_{n_a}$$

Equation 2.29

This is often rearranged in the van't Hoff form:

$$\Delta \mathrm{H}_{ads}(n_a) = R\left(\frac{d\ln P}{d\left(\frac{1}{T}\right)}\right)_{n_a}$$

Equation 2.30

The isosteric heat of adsorption, a commonly reported thermodynamic quantity, is given a positive value:*

$$\mathrm{q}_{st}(n_a) = -\Delta \mathrm{H}_{ads}(n_a) = -R\left(\frac{d\ln P}{d\left(\frac{1}{T}\right)}\right)_{n_a} > 0$$

Equation 2.31

For adsorption at temperatures or pressures outside the ideal gas regime, the density of the bulk gas phase is not easily simplified, and we use the more general relationship:

$$\mathrm{q}_{st}(n_a) = T\left(\frac{dP}{dT}\right)_{n_a} {\rho_g}^{-1}$$

Equation 2.32

If the excess adsorption, n_e, is substituted for the absolute quantity in the equations above, the result is called the "isoexcess heat of adsorption":

$$\mathrm{q}_{st}(n_e) = T\left(\frac{dP}{dT}\right)_{n_e} {\rho_g}^{-1}$$

Equation 2.33

* It is typical to report the "isosteric enthalpy of adsorption" in this way as well, and for our purpose, "increasing enthalpy" refers to the increase in magnitude of the enthalpy, or most specifically, the increase in the heat of adsorption.

It is common to include the ideal gas assumption in the isoexcess method since the assumptions are valid in similar regimes of temperature and pressure, giving:

$$\mathrm{q}_{st}(n_e) = -R\left(\frac{d\ln P}{d\left(\frac{1}{T}\right)}\right)_{n_e}$$

Equation 2.34

For cases where the adsorptive is in a regime far from ideality, it is sometimes necessary to use a better approximation for the change in molar volume specified in Equation 2.26. For example, gaseous methane at high pressures and near-ambient temperatures (near-critical) has a molar volume approaching that of liquid methane. Therefore, a more general equation must be used, and here we suggest to approximate the molar volume of the adsorbed phase as that of the adsorptive liquid at 0.1 MPa, v_{liq}:

$$v_g - v_a \approx v_g - v_{liq}$$

Equation 2.35

$$\frac{dP}{dT} = \frac{\left(s_g - s_a\right)}{v_g} = -\frac{\left(s_a - s_g\right)}{\left(v_g - v_{liq}\right)}$$

This gives the following equations for the isosteric and isoexcess heat of adsorption:

$$\mathrm{q}_{st}(n_a) = T\left(\frac{dP}{dT}\right)_{n_a}\left(v_g - v_{liq}\right)$$

Equation 2.36

$$\mathrm{q}_{st}(n_e) = T\left(\frac{dP}{dT}\right)_{n_e}\left(v_g - v_{liq}\right)$$

Equation 2.37

In summary:

Assumptions:	Isosteric Method	Isoexcess Method ($n_a \approx n_e$)
Ideal Gas $v_g \gg v_a$	$\Delta S_{ads}(n_a) = \frac{R}{T}\left(\frac{d\ln P}{d\left(\frac{1}{T}\right)}\right)_{n_a}$ $q_{st}(n_a) = -R\left(\frac{d\ln P}{d\left(\frac{1}{T}\right)}\right)_{n_a}$ Eq. 2.31	$\Delta S_{ads}(n_e) = \frac{R}{T}\left(\frac{d\ln P}{d\left(\frac{1}{T}\right)}\right)_{n_e}$ $q_{st}(n_e) = -R\left(\frac{d\ln P}{d\left(\frac{1}{T}\right)}\right)_{n_e}$ Eq. 2.34
Non-ideal Gas $v_g \gg v_a$	$\Delta S_{ads}(n_a) = -\left(\frac{dP}{dT}\right)_{n_a} {\rho_g}^{-1}$ $q_{st}(n_a) = T\left(\frac{dP}{dT}\right)_{n_a} {\rho_g}^{-1}$ Eq. 2.32	$\Delta S_{ads}(n_e) = -\left(\frac{dP}{dT}\right)_{n_e} {\rho_g}^{-1}$ $q_{st}(n_e) = T\left(\frac{dP}{dT}\right)_{n_e} {\rho_g}^{-1}$ Eq. 2.33
Non-ideal Gas $v_a \approx v_{liq}$	$\Delta S_{ads}(n_a) = -\left(\frac{dP}{dT}\right)_{n_a} (v_g - v_{liq})$ $q_{st}(n_a) = T\left(\frac{dP}{dT}\right)_{n_a} (v_g - v_{liq})$ Eq. 2.36	$\Delta S_{ads}(n_e) = -\left(\frac{dP}{dT}\right)_{n_e} (v_g - v_{liq})$ $q_{st}(n_e) = T\left(\frac{dP}{dT}\right)_{n_e} (v_g - v_{liq})$ Eq. 2.37

The Henry's law value of the isosteric enthalpy of adsorption, $-\Delta H_0$, is calculated by extrapolation of the adsorption enthalpy to zero uptake:

$$-\Delta H_0 = \lim_{n \to 0} \left(-\Delta H_{ads}(n)\right)$$

Equation 2.38

A common technique for determining the enthalpy of adsorption in the ideal gas approximation is to plot ln *P* as a function of T^{-1}, a van't Hoff plot, and to find the slope of the line along each isostere (corresponding to a fixed value of *n*). If the data are linear in a certain range of T^{-1}, the enthalpy of adsorption is determined to be temperature independent in that range, corresponding to the average temperature:

$$T_{avg} = \frac{2}{\left(\frac{1}{T_{max}} + \frac{1}{T_{min}}\right)}$$

Equation 2.39

If the slope is nonlinear, a subset of the data between two temperatures, T_1 and T_2, is found where the slope is approximately linear. A difference of 10 K is considered to be acceptable for most purposes.[15] Inside this "window," the average temperature is:

$$T_{window} = \frac{2}{\left(\frac{1}{T_1} + \frac{1}{T_2}\right)}$$

Equation 2.40

With a series of windows, a temperature dependence of the data can be determined within the range of temperatures collected.

2.4 Thermodynamic Calculations from Experimental Data

Simplicity and accuracy are desired in solving the thermodynamic relations derived in Section 2.3 for calculating the entropy and enthalpy of adsorption from experimental data. The limitations of the two most commonly applied simplifications, the ideal gas and isoexcess assumptions, are discussed in Sections 2.4.1-2.

The primary obstacles to a completely assumptionless derivation of the thermodynamic quantities of interest are twofold. Most importantly, both the isosteric and isoexcess treatments require tabulations of the equilibrium pressure, or ln *P*, at fixed values of uptake, n_a or n_e. Experimentally, it is possible to control P and measure the amount adsorbed, but exceedingly difficult to fix the adsorbed quantity and measure the equilibrium pressure. Therefore, a fitting equation is often used to interpolate the measured values. The interpolation of adsorption data is very sensitive to the fitting method chosen, and small deviations from the true value cause significant errors in thermodynamic calculations.[20-22] Sections 2.4.3-6 discuss the use of the data with and without a fitting equation, and compare the results across three types of model-independent fitting equations in an effort to determine the most accurate methodology for calculating thermodynamic quantities of adsorption.

Secondly, the determination of the absolute quantity of adsorption requires a model which defines the volume of the adsorbed phase as a function of pressure and temperature in the system. Numerous methods have been suggested to define it, and a successful model is presented in Section 2.5.

The data used for the comparisons is methane adsorption on superactivated carbon MSC-30, a standard carbon material whose properties are thoroughly discussed in Chapters 4-6. It is a well characterized material with traditional sorbent properties and a large surface area (giving a large signal to noise ratio in measurements of its adsorption uptake). The data set consists of 13 isotherms between 238-521 K, and spans pressures between 0.05-9 MPa, as shown in Figure 2.6.

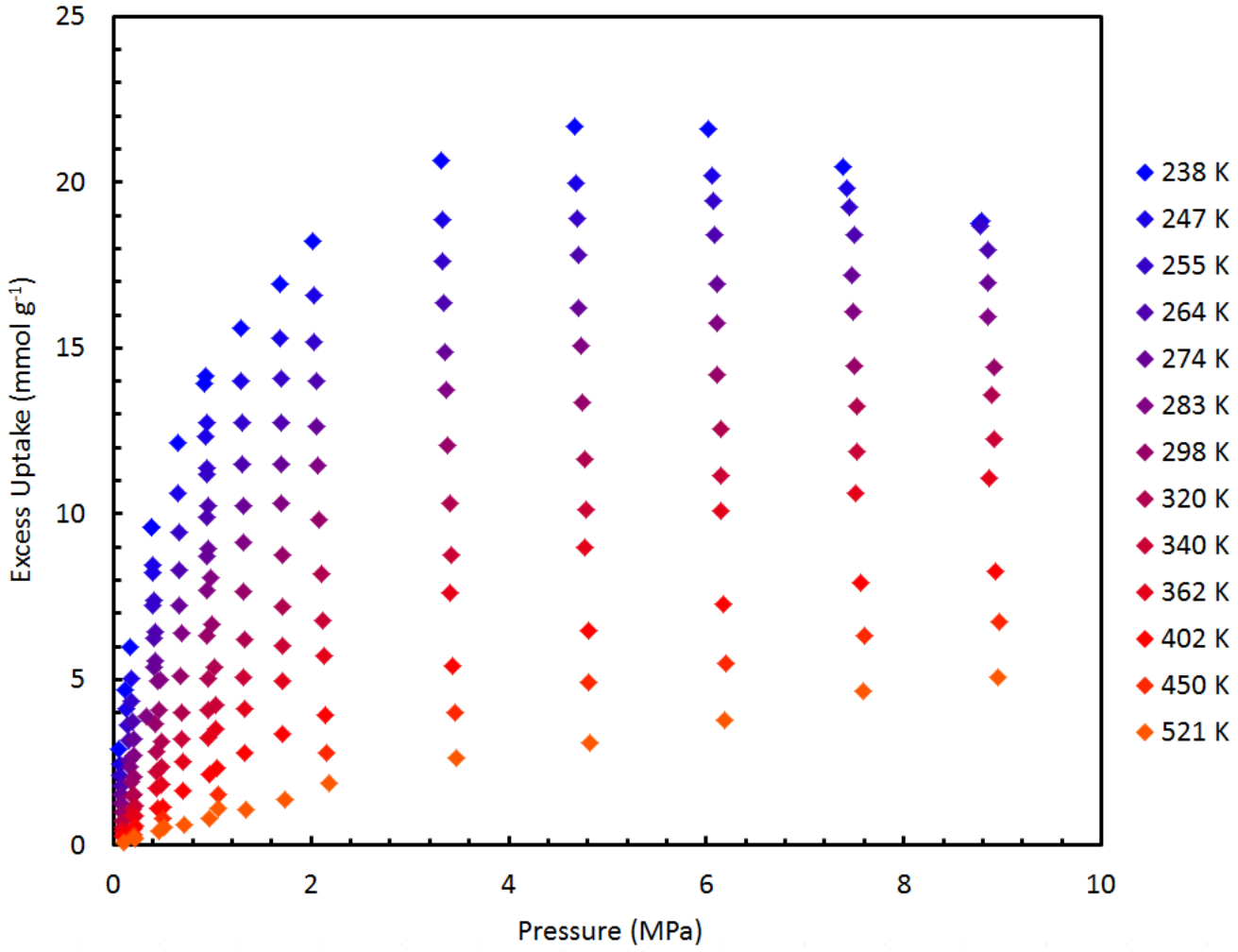

Figure 2.6. Equilibrium adsorption isotherms of methane on MSC-30 between 238-521 K, the test data for thermodynamic calculations of adsorption.

2.4.1 Ideal Gas Assumption

The ideal gas law is defined by two main approximations: that the gas molecules do not interact or have inherent volume. In the limit of zero pressure, all gases tend toward ideality since they are dilute enough that interactions are improbable and the total volume of the system is approximately unchanged by including the molecules in it. For hydrogen, the ideal gas law holds approximately true for a large pressure and temperature regime around ambient; for example, the error in density is only 6% even at 10 MPa and 298 K (see Figure 2.7a). However, at low temperatures and high pressures that are desired in many adsorption applications, non-ideality of the gas phase is strikingly apparent for most common gases. Figure 2.7b shows the density of methane as a function of pressure at various temperatures of interest for storage applications. The very significant non-ideality of both hydrogen and methane is apparent at room temperature and elevated pressures. In addition, each gas shows significant non-ideality in their respective low temperature regimes of interest for storage applications, even at low pressures. This is an issue for most adsorptive gases since the latent heat of physical adsorption is very close to that of liquefaction.

The van der Waals equation of state predicts a density for hydrogen and methane that is generally an acceptable approximation of the true density at pressures up to 10 MPa, as shown in Figure 2.8. For hydrogen at 77 K, the error in density is less than 0.4% between 0-5 MPa, an acceptable figure for isosteric heat calculations, and much improved compared to the 4.5% error in the ideal gas density.

Ultimately, real gases exhibit properties that cannot be accurately modeled in our pressure and temperature regime of interest by any simple means. The most accurate pure fluid model available at this time is the 32-term modified Benedict-Webb-Rubin (mBWR) equation of state.[23] For this work, we refer to the mBWR model, as implemented by the REFPROP standard reference database,[24] as the "real gas" equation of state.

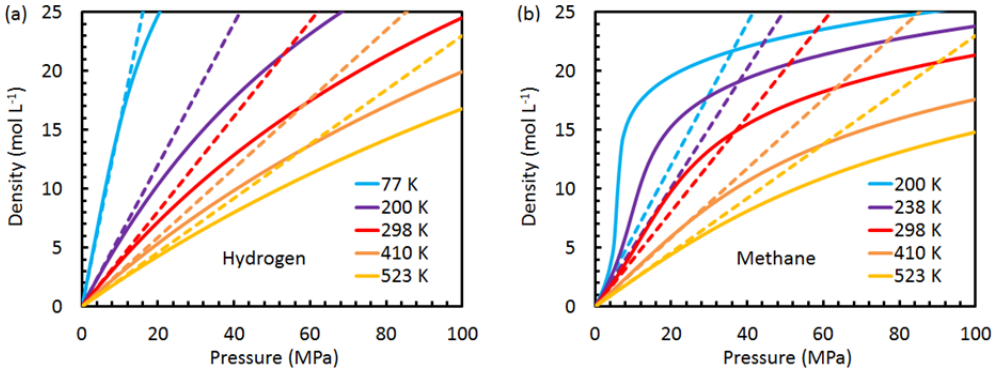

Figure 2.7. A comparison of ideal gas density (dotted lines) to (a) hydrogen and (b) methane at various temperatures, and pressures up to 100 MPa.

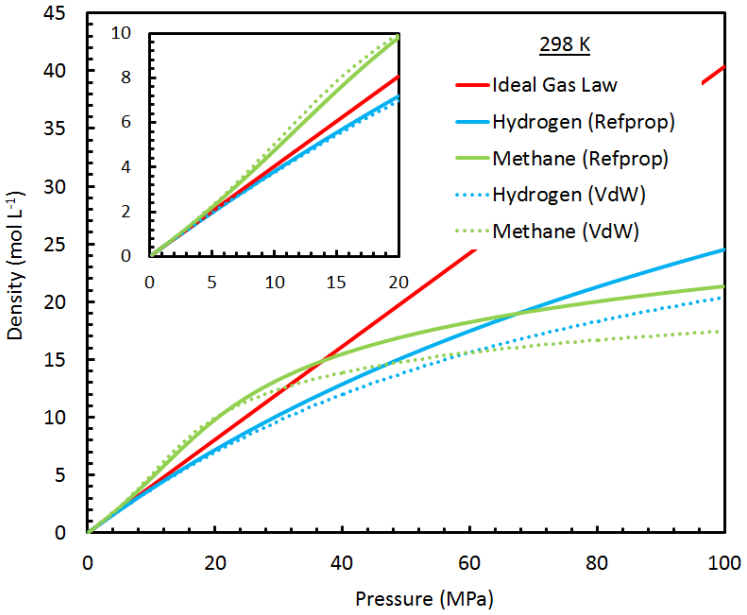

Figure 2.8. A comparison of the ideal gas, van der Waals (vdW) gas, and real (mBWR) gas density of methane and hydrogen at 298 K between 0-100 MPa.

2.4.2 Isoexcess Assumption

For thermodynamic or other calculations from experimental adsorption data at sufficiently low pressures, such as in determining BET surface area, the measured (excess) quantity of adsorption (from Equation 2.21) suffices for approximating the total adsorption amount. However, this assumption quickly becomes invalid even at relatively modest pressures and especially at low temperatures where the gas density is high compared to the density of the adsorbed layer. [20, 21]

Nevertheless, the simplest approach to thermodynamic calculations using experimental isotherm data is to proceed with the measured excess uptake quantity, n_e, in place of the absolute adsorption quantity, n_a. Since the volume of adsorption is fundamentally unknown, a model is required to determine the absolute adsorption amount, a task that is beyond the scope of many adsorption studies. This shortcut is valid in the low coverage limit since, from Equation 2.21, if the pressure of the gas approaches zero:

$$\lim_{P\to 0}(n_a) = \lim_{P\to 0}\left(n_e + \rho_g\, V_{ads}\right) = n_e + 0 = n_e$$

Equation 2.41

This approach can therefore be effective for approximating the "Henry's law" value of the isosteric enthalpy of adsorption. However, it leads to significant errors in determining the dependence of the enthalpy on uptake (discussed further in Section 2.4.3-5) and any isoexcess enthalpy of adsorption values calculated at coverages higher than n_e/n_{max} = 0.5 should only be accepted with great caution.

2.4.3 Calculations Without Fitting

Controlling the pressure of experimental measurements is possible, but it proves very difficult to perform experiments at specific fixed quantities of uptake. By coincidence, such as in a large data set like the one used in this comparison, it may happen that numerous data points lie at similar values of excess adsorption, and analysis of the isosteric enthalpy of adsorption may be performed without fitting. The van't Hoff plot of these coincidentally aligned points is shown in Figure 2.9.

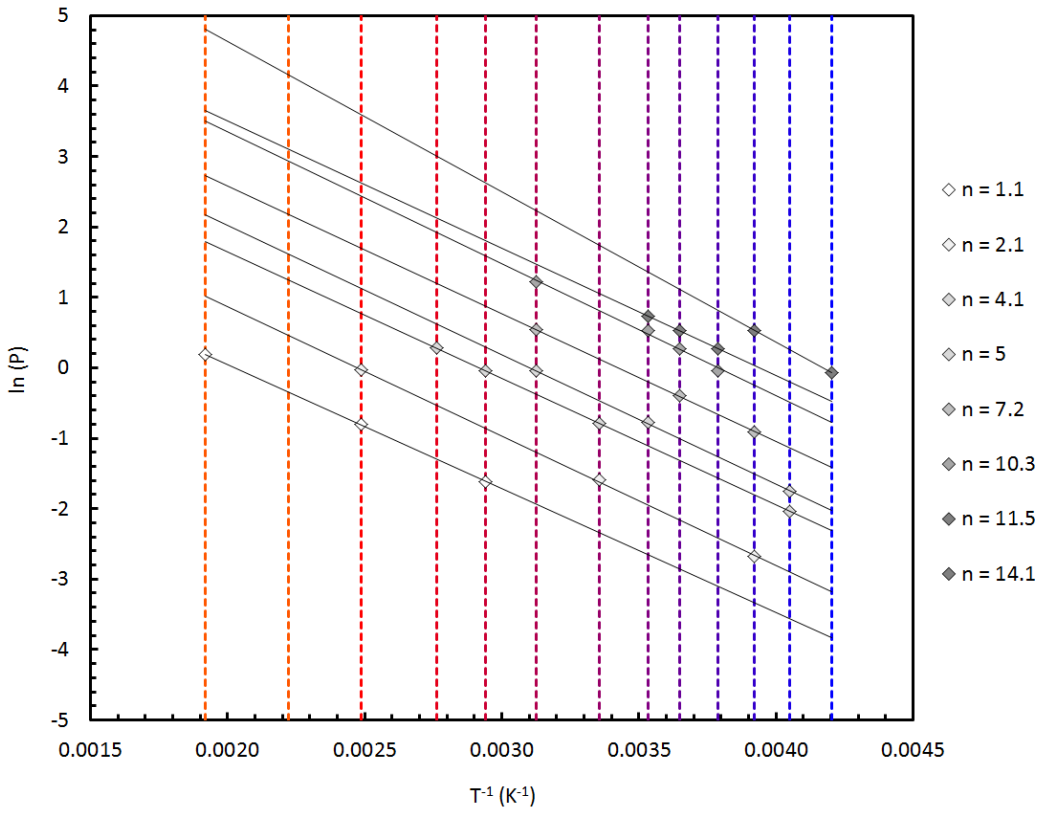

Figure 2.9. The van't Hoff plot of the (unfitted) methane uptake data at particular values of excess adsorption on MSC-30. The dashed colored lines, from blue to orange, indicate the temperatures of the isotherms from 238-521 K, respectively.

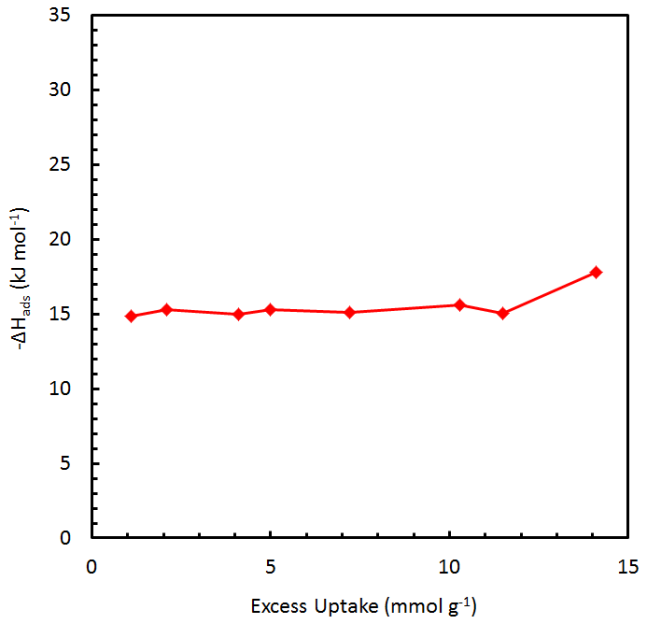

Figure 2.10. The average isoexcess enthalpy of adsorption calculated over the entire temperature range of data shown in Figure 2.9, 238-521 K.

Since the experimental quantity is excess adsorption, the isoexcess method must be used; the resulting isoexcess enthalpy of adsorption is shown in Figure 2.10. This method is severely limited since it relies on the statistical probability of two data points lying on the same isostere in the van't Hoff plot. This likelihood is dramatically less at high uptake where only low temperature data are available, and requires intense experimental effort to be accurate. The "fixed" values of n_e are necessarily approximated (in this case, ±0.05 mmol g^{-1}) and the absolute adsorbed amount is not used, resulting in a significant, unphysical divergence at high values of uptake. Nonetheless, without any fitting equation or model, we achieve an acceptable determination of the Henry's law value of the enthalpy of methane adsorption on MSC-30 (as an average over the entire temperature range): 15 kJ mol^{-1} at T_{avg} = 310 K.

2.4.4 Linear Interpolation

A primitive method for fitting the experimental adsorption data is by linear interpolation. This method does not require any fitting equation and is the simplest approach to determining values of P at specific fixed values of n_e to be used in the isoexcess method. The MSC-30 data set fitted by linear interpolation and the resulting van't Hoff plot is shown in Figure 2.11. The data are often apparently linear for analysis across the entire range of n_e, but are limited to the values of n_e where there are multiple measured points (favoring the measurements at low uptake and low temperature). Additionally, at high values of n_e the isoexcess approximation becomes invalid, or $n_e \neq n_a$, and errors become larger as n_e increases.

To calculate the enthalpy of adsorption, the isoexcess method is used because the absolute adsorption is unknown; the results are shown in Figure 2.12. The average enthalpy of adsorption over the entire data set (where T_{avg} = 310 K) is plotted at the top. The temperature dependent results are plotted at top, middle, and bottom, using windows of sizes 3, 5, and 7 temperatures, respectively. The colors from blue to orange represent the average temperatures of each window, from low to high. Two observations may be made: there is no significant trend of the temperature dependence of the data, and increasing the window size has the effect of decreasing outliers but not elucidating any further insight into the thermodynamics of adsorption in this system. As before, the enthalpy of adsorption diverges at high values of uptake where the isoexcess approximation is invalid (n_e > 10) and cannot be regarded as accurate.

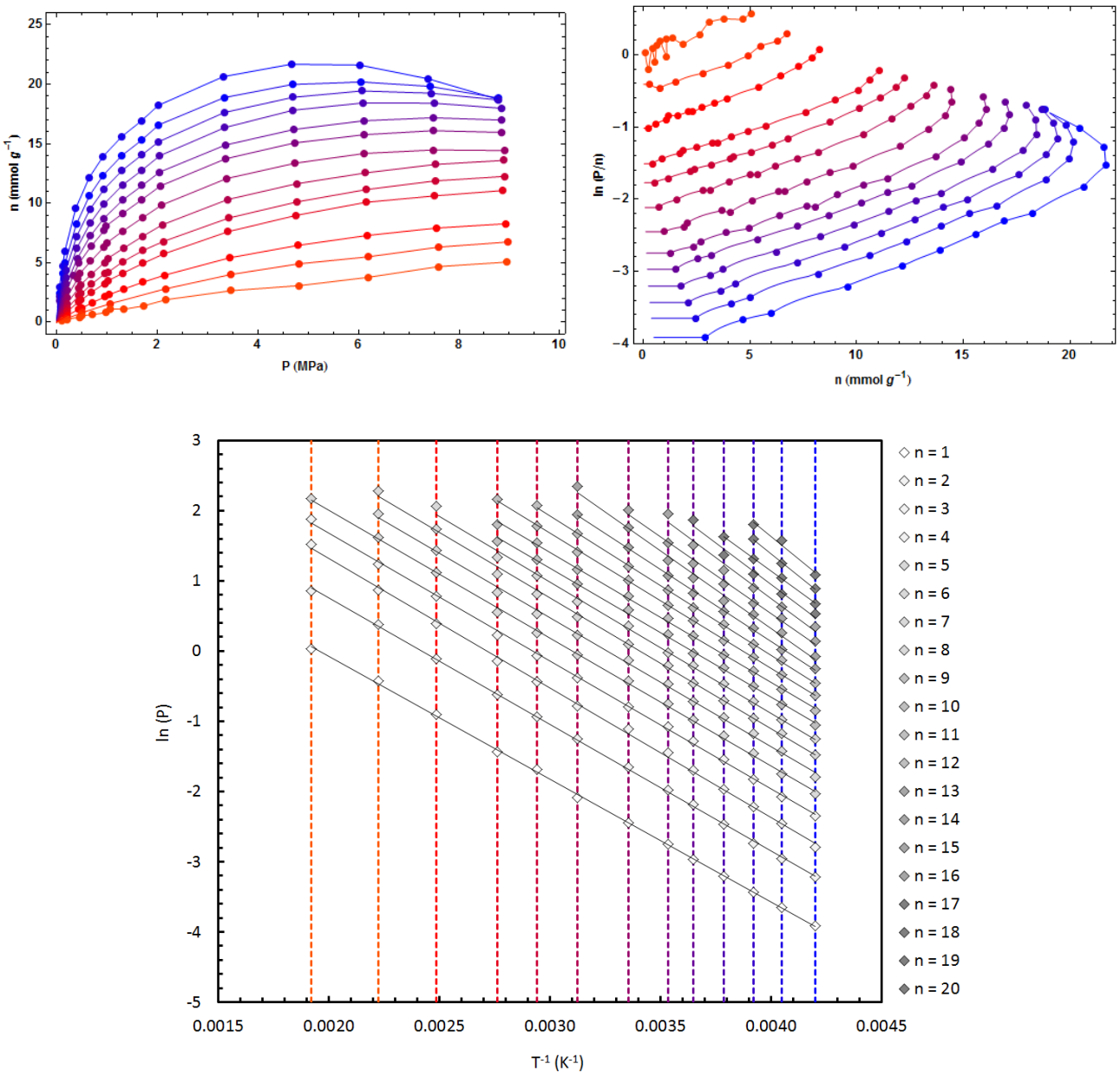

Figure 2.11. Linear interpolation of the experimental (excess) uptake data of methane on MSC-30 (top), and the corresponding van't Hoff plot showing the relative linearity of the data even using this primitive fitting technique (bottom). The colored lines, from blue to orange, indicate the temperatures of the measurements from 238-521 K, respectively.

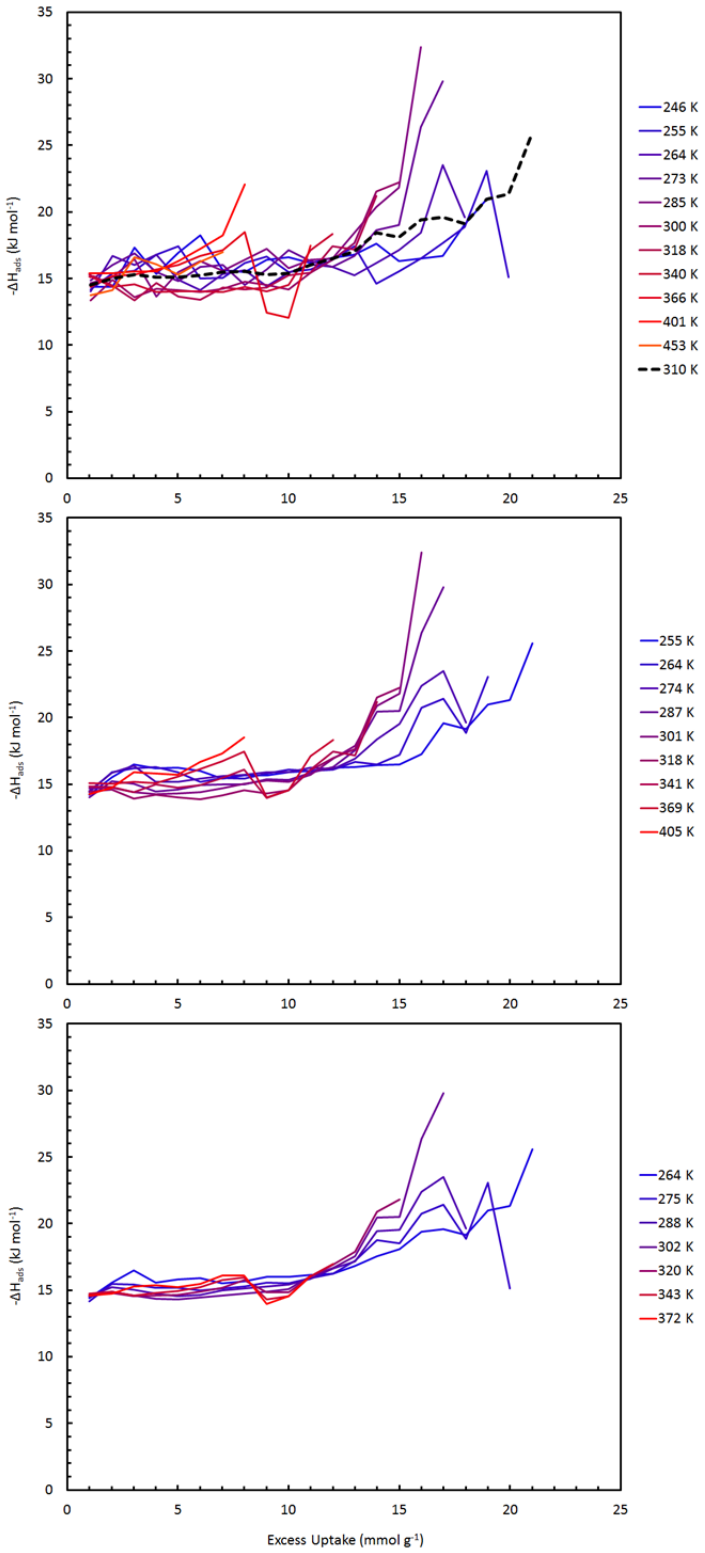

Figure 2.12. Isoexcess enthalpy of adsorption of methane on MSC-30, using linear interpolation fits and 3- (top), 5- (middle), and 7- (bottom) temperature windows. A calculation over all data (a single 13-temperature window) is also shown (dashed black).

2.4.5 Virial Type Fitting Equation

Numerous equations have been suggested to fit experimental adsorption data for thermodynamic calculations. The most common is to fit the data with a model-independent virial-type equation[25] and proceed with the Gibbs excess quantities, n_e, as directly fitted. The advantages to this method are that the number of fitting parameters is easily adjusted to suit the data. The fitting equation has the form:

$$\ln\left(\frac{P}{n_e}\right) = \frac{1}{T}\sum_i a_i {n_e}^i + \sum_i b_i {n_e}^i$$

Equation 2.42

The parameters a_i and b_i are temperature independent, and optimized by a least squares fitting algorithm. The experimental data of methane adsorption on MSC-30 are shown in Figure 2.13, fitted using first, third, and fifth order terms (with 4, 8, and 12 independent parameters, respectively). It can be observed that the data are very poorly fitted beyond the Gibbs excess maximum and cannot be used. In addition, as the number of fitting parameters is increased, a well-known limitation of polynomial fitting occurs: a curvature is introduced between data points. However, the isoexcess method is never employed beyond the Gibbs excess maximum, and an analogous plot of optimized fits of only selected data is shown in Figure 2.14. The data are well approximated even for i = 1, but some improvement is gained for i = 3. There is no significant improvement by adding parameters to i = 5. The data are well fitted at low temperatures up to ~4 MPa and at all pressures for isotherms at and above 340 K.

The enthalpy of adsorption is calculated by the isoexcess method, using:

$$-\Delta \mathrm{H}_{ads}(n_e) = -R\left(\frac{d\ln P}{d\left(\frac{1}{T}\right)}\right)_{n_e} = \sum_i a_i {n_e}^i$$

Equation 2.43

The functional form of the enthalpy is that of an i^{th} order polynomial. Therefore, if only first order parameters are used, the enthalpy will be a straight line (as shown in Figure 2.15). This is acceptable for some purposes, but allows little potential insight to the true dependence of the enthalpy on uptake. A fit using higher order terms may be preferred for that reason. Nevertheless, in this comparison, third order terms do not lend any significant contribution to the analysis (see Figure 2.16). The Henry's law value of the enthalpy calculated in Equation 2.43 is:

$$-\Delta \mathrm{H}_0 = \lim_{n\to 0}\left(\sum_i a_i {n_e}^i\right) = a_0$$

Equation 2.44

The fits of select data give values of the Henry's law enthalpy in the range of 13.5-17.5 kJ mol^{-1}. Since the parameters are constant with temperature, it is not possible to determine the temperature dependence of the isoexcess enthalpy with a single fitting equation, and it is often assumed to be negligible. If a moving window method is employed, a temperature dependence is accessible, but does not yield any significant trends in this case (for windows of 3 temperatures, with i = 1 or i = 3) as shown in Figures 2.15-16. All calculations show an increasing isoexcess enthalpy of adsorption except for small windows of isotherms using only first order fits, and overall, this fitting methodology is unsatisfactory for analyzing methane adsorption on MSC-30.

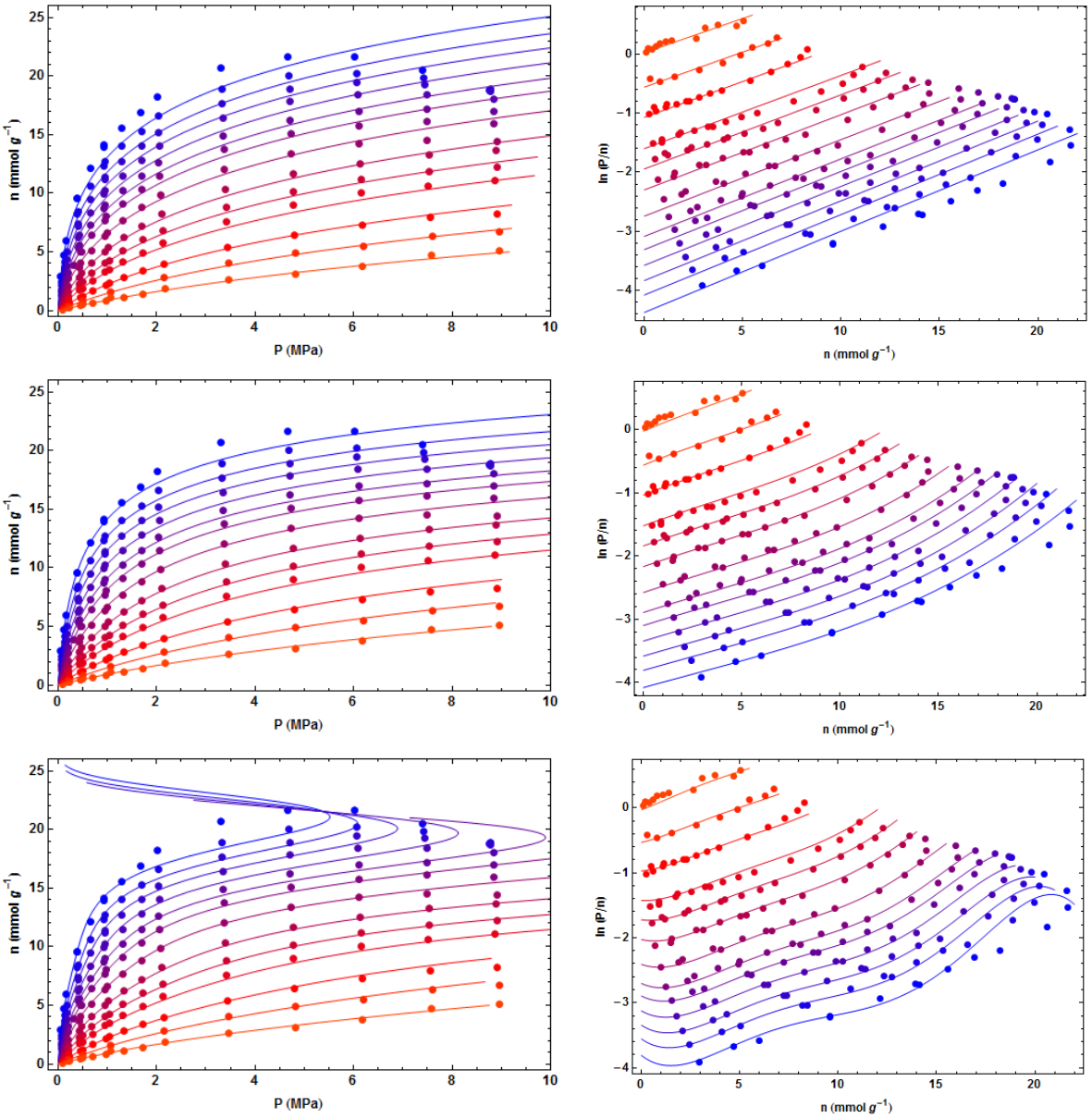

Figure 2.13. First- (top), third- (middle), and fifth-order (bottom) virial-equation fits of methane adsorption uptake on MSC-30 between 238-521 K, fitting the *complete* data set including the uptake beyond the Gibbs excess maximum.

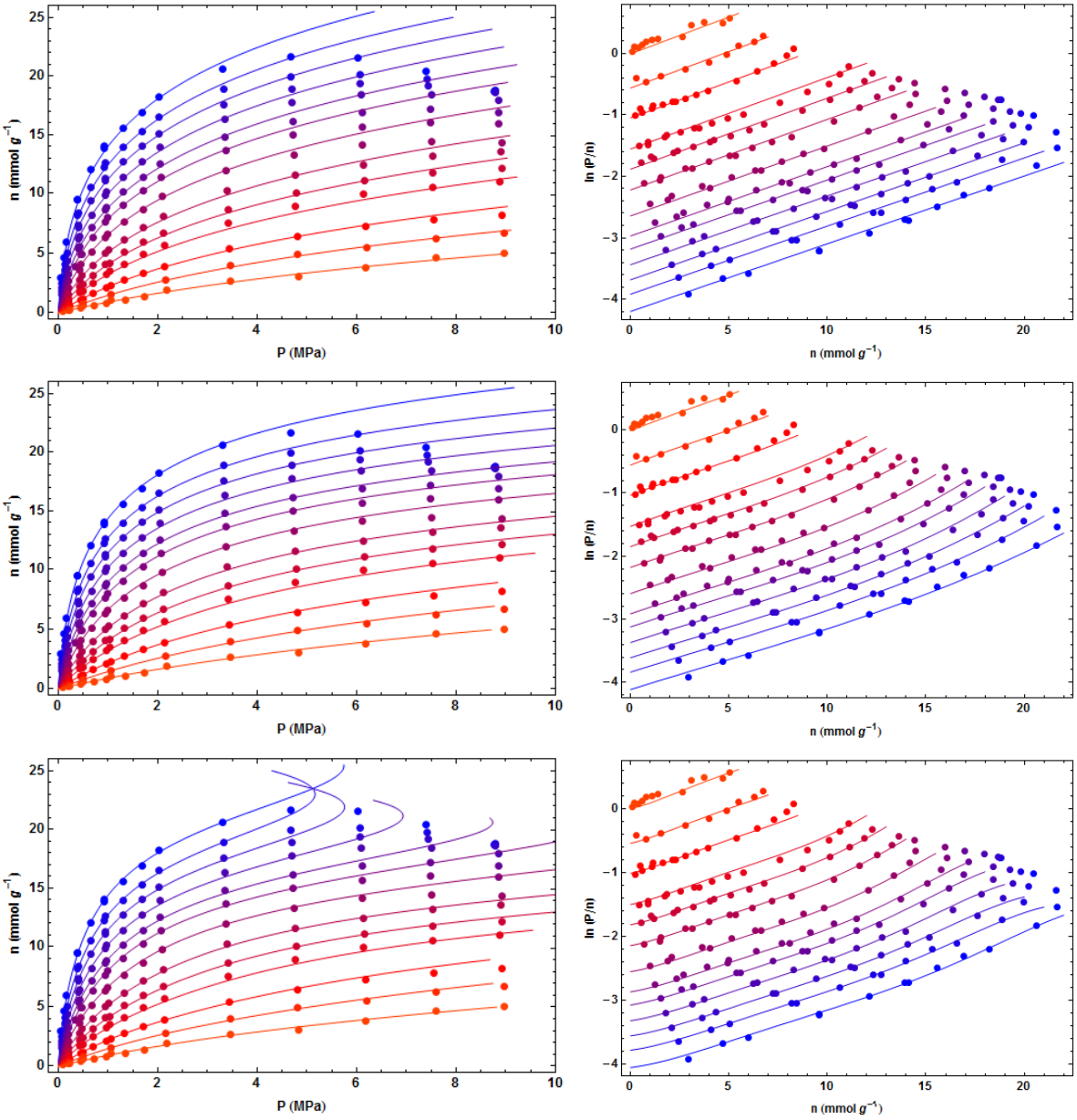

Figure 2.14. First- (top), third- (middle), and fifth-order (bottom) virial-equation fits of methane adsorption uptake on MSC-30 between 238-521 K, fitting *only the data below the Gibbs excess maximum*.

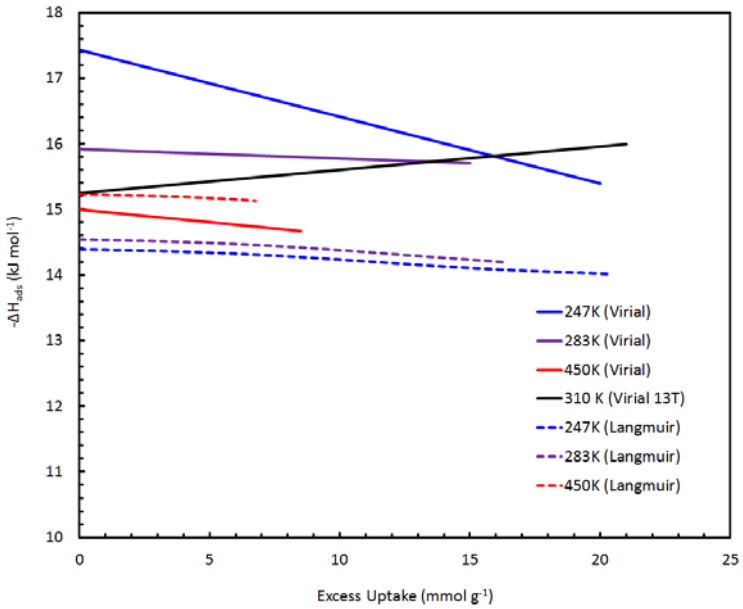

Figure 2.15. Isoexcess enthalpy of adsorption, using first-order virial equation fits and 3-temperature windows. Also shown is the result for a first-order virial equation fit using the entire data set, a 13-temperature (13T) single window. The calculated enthalpies are compared to those for a generalized-Langmuir fit (given in Section 2.5).

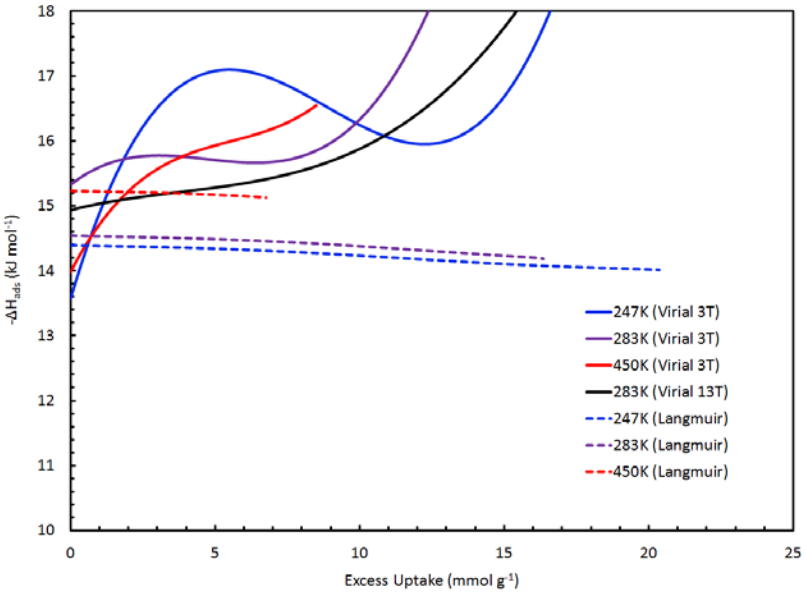

Figure 2.16. Isoexcess enthalpy of adsorption, using third-order virial equation fits and 3-temperature windows. Also shown is the result for a third-order virial equation fit using the entire data set, a 13-temperature (13T) single window. The calculated enthalpies are compared to those for a generalized-Langmuir fit (given in Section 2.5).

2.4.6 Generalized-Langmuir Fitting Equation

A major limitation of the virial-type equation is that it does not accurately interpolate the data at high adsorption uptake in the near- or supercritical regime where the maximum in Gibbs excess is a prominent feature of the data. Another approach is to incorporate the Gibbs definition (Equation 2.21) of adsorption into the fitting equation, which can be done in a model-independent way.

An effective strategy is to choose a functional form for n_a that is monotonically increasing with pressure, consistent with the physical nature of adsorption.[20] The Langmuir isotherm is one example, although others have been suggested (e.g., Langmuir-Freundlich,[21] Unilan,[22] and Toth[26] equations). If an arbitrary number of Langmuir isotherms are superpositioned, referred to as a generalized-Langmuir equation, the number of independent fitting parameters can be easily tuned to suit the data. Langmuir was the first to generalize his equation for a heterogeneous surface consisting of numerous different adsorption sites of different characteristic energies.[27] Implementing the generalized-Langmuir model (Equation 2.16) in a model-independent way, absolute adsorption takes the form:

$$n_a(P,T) = c_n \sum_i \alpha_i \left(\frac{K_i P}{1 + K_i P}\right)$$

$$\sum_i \alpha_i = 1$$

Equation 2.45

The volume of adsorption in the Gibbs equation also has a pressure dependence that is fundamentally unknown, but which is generally accepted to be monotonically

increasing in most systems. It too can be approximated by a generalized-Langmuir equation, simplifying the final equation and keeping the number of parameters low:

$$V_{ads}(P,T) = c_V \sum_i \alpha_i \left(\frac{K_i P}{1 + K_i P}\right)$$

Equation 2.46

The excess adsorption data are then fitted to:

$$n_e(P,T) = c_n \sum_i \alpha_i \left(\frac{K_i P}{1 + K_i P}\right) - \left(c_V \sum_i \alpha_i \left(\frac{K_i P}{1 + K_i P}\right)\right) \rho(P,T)$$

$$n_e(P,T) = \left(c_n - c_V \rho(P,T)\right)\left(\sum_i \alpha_i \left(\frac{K_i P}{1 + K_i P}\right)\right)$$

Equation 2.47

The K_i are equivalent to the equilibrium constants of adsorption in the classical Langmuir model, but are not required to have physical meaning for this purpose. They can be taken as constant with pressure, but having a dependence on temperature similar to Equation 2.13:

$$K_i = \frac{C_i}{\sqrt{T}} e^{\frac{E_i}{RT}}$$

Equation 2.48

The fitting parameters (c_n, c_V, α_i, C_i, and E_i) are constants. If the ideal gas law applies to the pressure and temperature regime of interest, the equation simplifies:

$$n_e(P,T) = \left(c_n - c_V \frac{P}{RT}\right)\left(\sum_i \alpha_i \left(\frac{K_i P}{1 + K_i P}\right)\right)$$

Equation 2.49

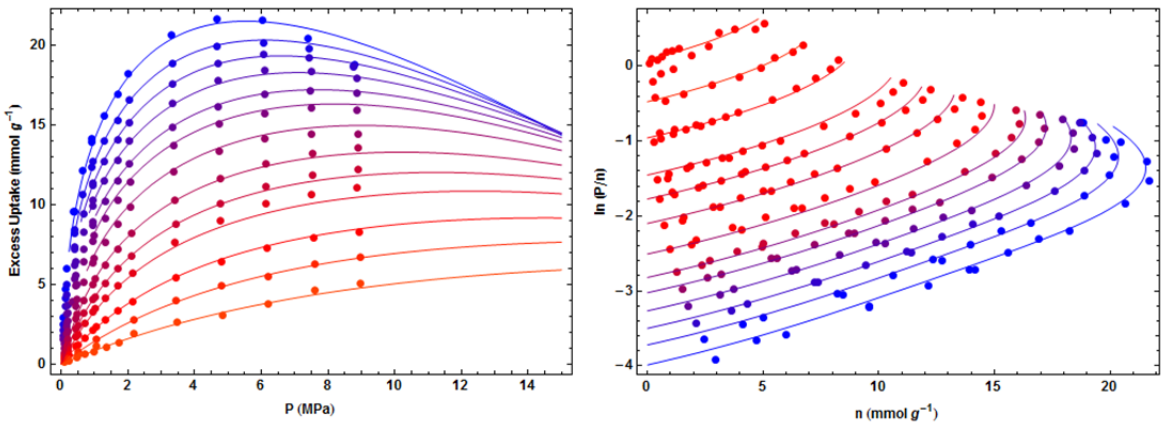

Figure 2.17. Double-Langmuir fit of methane uptake on MSC-30 using the ideal gas law.

The experimental data fitted by a double-Langmuir isotherm (i = 2) with the ideal gas assumption are shown in Figure 2.17. For all but the highest pressures, the data are well approximated by this method. The curvature of the interpolation between points, even near or at the Gibbs excess maximum, is representative of the physical nature of the system, and the extrapolation to high pressures shows much improved behavior compared to the previous fitting methods. A limitation of the ideal gas assumption is that the excess uptake isotherms cannot cross at high pressure, the lowest temperature data decreasing proportionally with pressure. This is not consistent with experimental results where it frequently occurs that low temperature data falls significantly below higher temperature data at the same pressure. This phenomenon is entirely due to non-ideal gas interactions from a nonlinear change in gas density, and can be accounted for by using the more general form of the excess adsorption (Equation 2.47). Data fitted using 1, 2, and 3 superimposed Langmuir isotherms (with 4, 7, and 10 independent parameters, respectively) and using the mBWR gas density are shown in Figure 2.18.

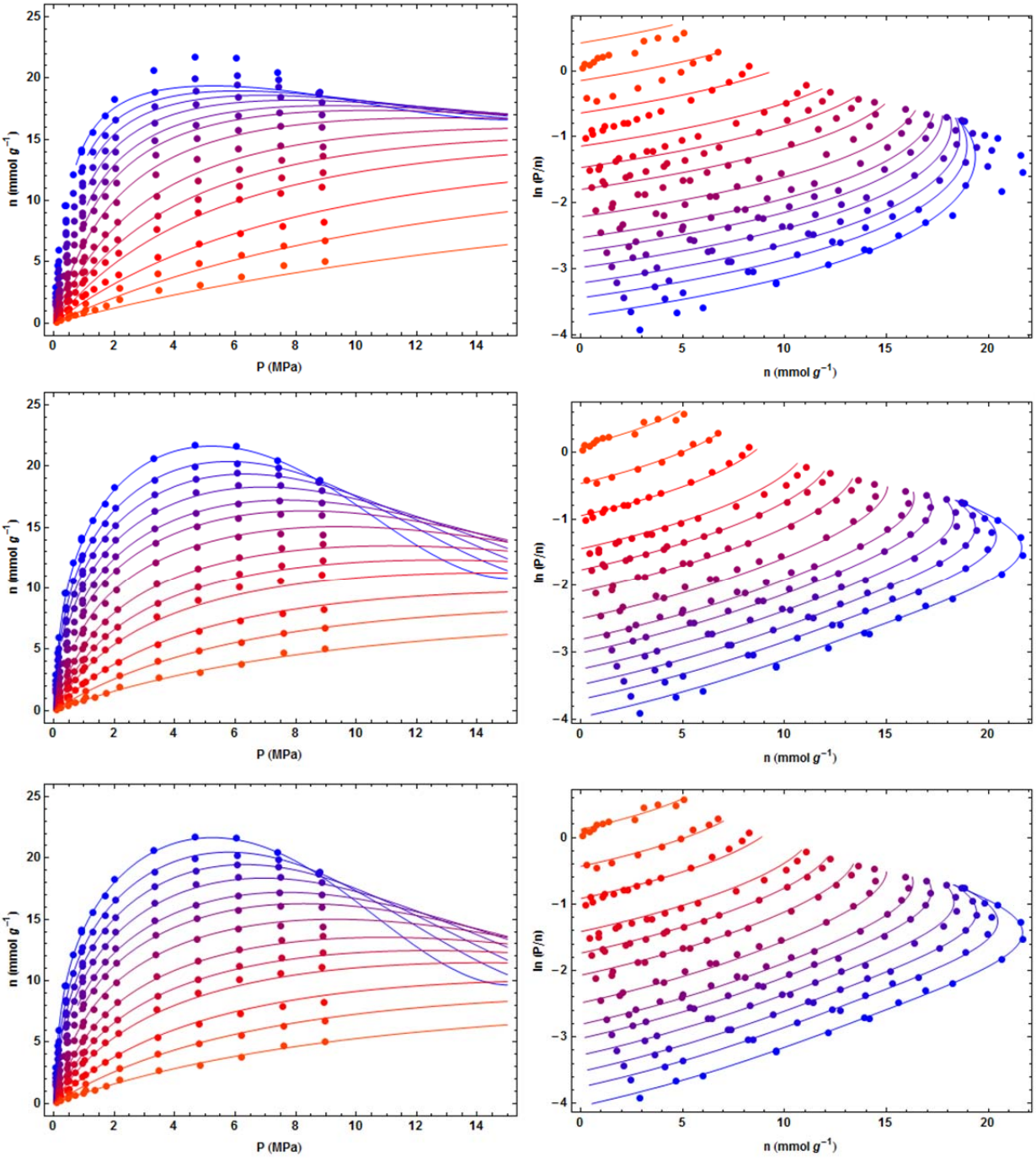

Figure 2.18. Single- (top), double- (middle), and triple- (bottom) Langmuir equation fits of methane adsorption uptake on MSC-30 between 238-521 K.

The double-Langmuir fit is satisfactory for thermodynamic calculations, and is the preferred method in this study. The triple-Langmuir fit is not significantly improved to justify the addition of 3 independent fitting parameters. The extrapolation of the data to high pressures shows behavior consistent with other experimental results of hydrogen and methane adsorption at low temperature.

2.5 Generalized-Langmuir High-Pressure Adsorption Model

To understand the true thermodynamic quantities of adsorption from experimentally measured adsorption data, a model is necessary to determine the absolute adsorption amount as a function of pressure. The necessary variable that remains unknown is the volume of the adsorption layer and numerous methods have been suggested to estimate it. Typical methods include fixing the volume of adsorption as the total pore volume of the sorbent material,[20] using a volume proportional to the surface area (assuming fixed thickness),[28] or deriving the volume by assuming the adsorbed layer is at liquid density.[29] Some approaches are specific to graphite-like carbon materials, such as the Ono-Kondo model.[30, 31] The most general approach is to let the adsorption volume be an independent parameter of the fitting equation of choice, equivalent to the parameter c_V in the model-independent treatment above.

The generalized-Langmuir equation[20] (as shown in Section 2.4.6) and numerous others (e.g., Langmuir-Freundlich,[21] Unilan,[22] and Toth[26] equations) have been shown to be suitable fitting equations for determining absolute adsorption from excess uptake isotherms since they are monotonically increasing and contain a relatively small number

of fitting parameters to achieve a satisfactory fit to the experimental data. We consider the following fitting equation for Gibbs excess adsorption as a function of pressure, identical in form to the model-independent equation above (Equation 2.47):

$$n_e(P,T) = \left(n_{max} - V_{max}\,\rho(P,T)\right)\left(\sum_i \alpha_i \left(\frac{K_i\,P}{1+K_i\,P}\right)\right)$$

$$K_i = \frac{A_i}{\sqrt{T}} e^{\frac{E_i}{RT}} \qquad \sum_i \alpha_i = 1$$

Equation 2.50

The minimum number of independent parameters is desired, and we find that *i* = 2 yields satisfying results across a number of materials in supercritical adsorption studies of both methane and hydrogen (where the regime beyond the excess maximum is well-characterized), giving the reduced equation:

$$n_e(P,T) = \left(n_{max} - V_{max}\,\rho(P,T)\right)\left((1-\alpha)\left(\frac{K_1\,P}{1+K_1\,P}\right) + \alpha\left(\frac{K_2\,P}{1+K_2\,P}\right)\right)$$

Equation 2.51

We have found that the assumption that the total adsorption volume scales proportionally with site occupancy is robust, and this fitting equation has been shown to be successful for both carbonaceous (see Chapter 6) and MOF materials.[20] We refer to this method as the double-Langmuir method, and if the absolute quantity of adsorption is held constant, it yields the true isosteric quantities of adsorption. The absolute quantity, from the Gibbs definition, is:

$$n_a(P,T) = n_{max}\left((1-\alpha)\left(\frac{K_1\,P}{1+K_1\,P}\right) + \alpha\left(\frac{K_2\,P}{1+K_2\,P}\right)\right)$$

Equation 2.52

The fractional site occupancy, also called the surface coverage, is:

$$\theta(P,T) = (1-\alpha)\left(\frac{K_1\,P}{1+K_1\,P}\right) + \alpha\left(\frac{K_2\,P}{1+K_2\,P}\right)$$

Equation 2.53

Least squares fits of methane uptake on MSC-30 to the double-Langmuir equation are shown in Figure 2.19, the fitted excess adsorption (left) and calculated absolute adsorption (right) at all temperatures measured. The goodness of fit is satisfactory across the entire range of temperature and pressure, with a residual sum of squares less than 0.04 mmol g^{-1} per data point. The optimal fitting parameters for MSC-30 are given in Table 5.2, and their relation to the materials properties is discussed in Section 5.2.3.

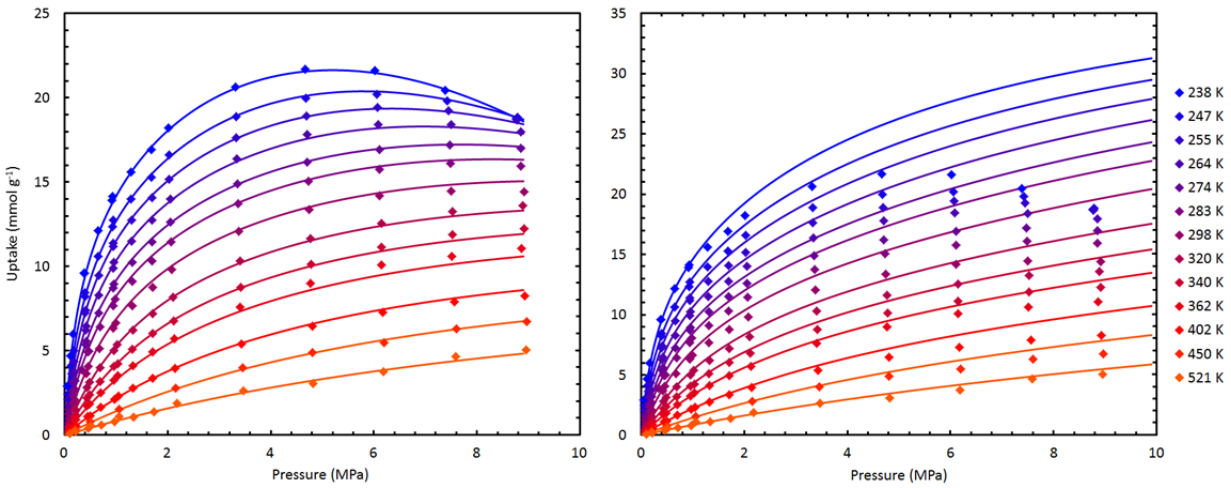

Figure 2.19. Double-Langmuir equation fits of methane adsorption uptake on MSC-30 between 238-521 K, showing calculated excess uptake (left) and calculated absolute uptake (right) as solid lines, and the measured excess uptake data as filled diamonds (left and right).

To derive the isosteric enthalpy from the generalized Langmuir equation, the derivative of pressure with respect to temperature is decomposed as follows:

$$\left(\frac{\partial P}{\partial T}\right)_{\mathrm{n_a}} = \left(\frac{\partial \theta}{\partial P}\right)_{\mathrm{n_a}}^{-1} \sum_i \left(\frac{\partial \theta}{\partial K_i}\right)_{\mathrm{n_a}} \left(\frac{\partial K_i}{\partial T}\right)_{\mathrm{n_a}}$$

Equation 2.54

From Equations 2.50-53, the respective components of the derivative are given by:

$$\left(\frac{\partial \theta}{\partial P}\right)_{\mathrm{n_a}} = \left(\frac{\partial}{\partial P}\right)_{\mathrm{n_a}} \left((1-\alpha)\left(\frac{K_1 P}{1+K_1 P}\right) + \alpha\left(\frac{K_2 P}{1+K_2 P}\right)\right)$$

$$= \left((1-\alpha)\left(\frac{K_1}{(1+K_1 P)^2}\right) + \alpha\left(\frac{K_2}{(1+K_2 P)^2}\right)\right) = X^{-1}$$

$$\left(\frac{\partial \theta}{\partial K_1}\right)_{\mathrm{n_a}} = (1-\alpha)\left(\frac{P}{(1+K_1 P)^2}\right) = Y_1$$

$$\left(\frac{\partial \theta}{\partial K_2}\right)_{\mathrm{n_a}} = \alpha\left(\frac{P}{(1+K_2 P)^2}\right) = Y_2$$

$$\left(\frac{\partial K_i}{\partial T}\right)_{\mathrm{n_a}} = \left(\frac{\partial}{\partial T}\right)_{\mathrm{n_a}} \left(\frac{A_i}{\sqrt{T}} e^{\frac{E_i}{RT}}\right) = -\frac{\frac{1}{2}RT + E_i}{RT^2} \frac{A_i}{\sqrt{T}} e^{\frac{E_i}{RT}} = -Z_i$$

These are combined to find the isosteric enthalpy of adsorption, in Equations 2.31-37. When a double-site Langmuir isotherm (i = 2) is used, this can be written as:

$$-\left(\frac{\partial P}{\partial T}\right)_{\mathrm{n_a}} = X\,(Y_1 Z_1 + Y_2 Z_2)$$

Equation 2.55

The isosteric enthalpy of adsorption of methane on MSC-30 is shown in Figure 2.20, using the ideal gas law to approximate the density in the gas phase. The results are consistent with reported results for numerous sorbent systems and show a physically insightful dependence of the isosteric enthalpy on both uptake and temperature. The Henry's law value is between 14.5-15.5 kJ mol^{-1}, consistent with the isoexcess results

calculated without a fitting equation (the best approximate of the Henry's law value), and the enthalpy declines with uptake to 14 kJ mol^{-1}. Due to the ideal gas dependence of the density with pressure, the enthalpy reaches a plateau at high values of uptake.

When the real gas data is used, the calculation of isosteric enthalpy changes significantly at high pressures, as shown in Figure 2.21. Non-ideality of methane in the gas phase is substantial under these conditions and must be taken into account for the most accurate description of adsorption thermodynamics in MSC-30, and was also necessary when extended to other systems. The tendency of the isosteric heat to a constant value at high uptake[32] is commonly reported as evidence of proper calculation procedures[20, 21]; however a plateau was not observed when ideal gas assumptions were

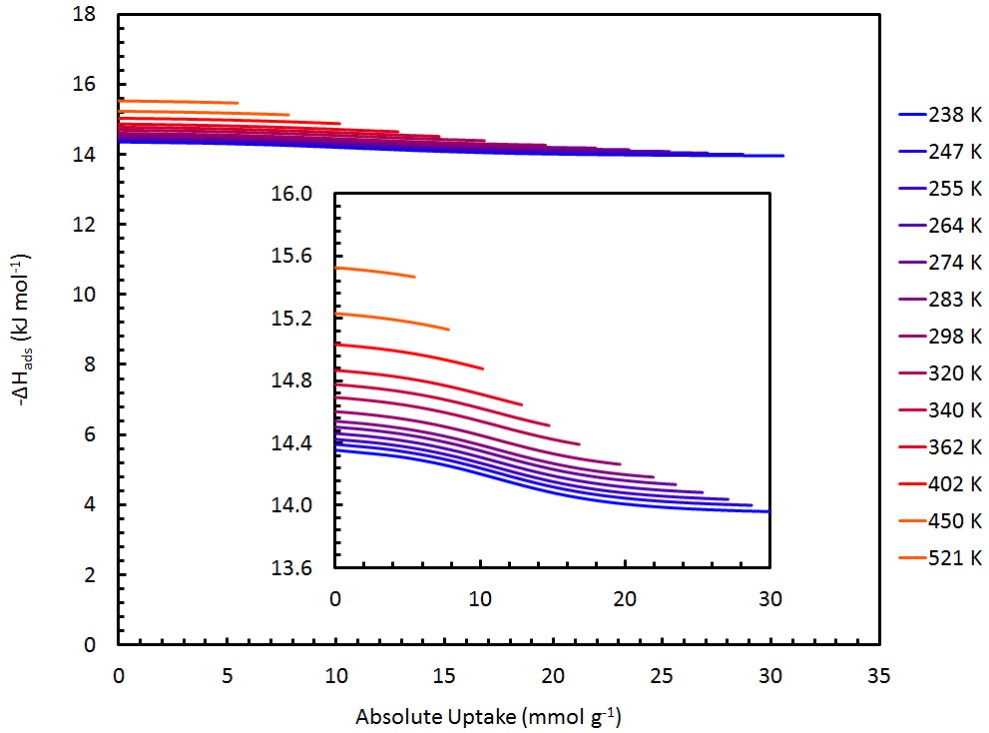

Figure 2.20. Isosteric enthalpy of adsorption, using a double-Langmuir fit with the ideal gas assumption (Equation 2.31).

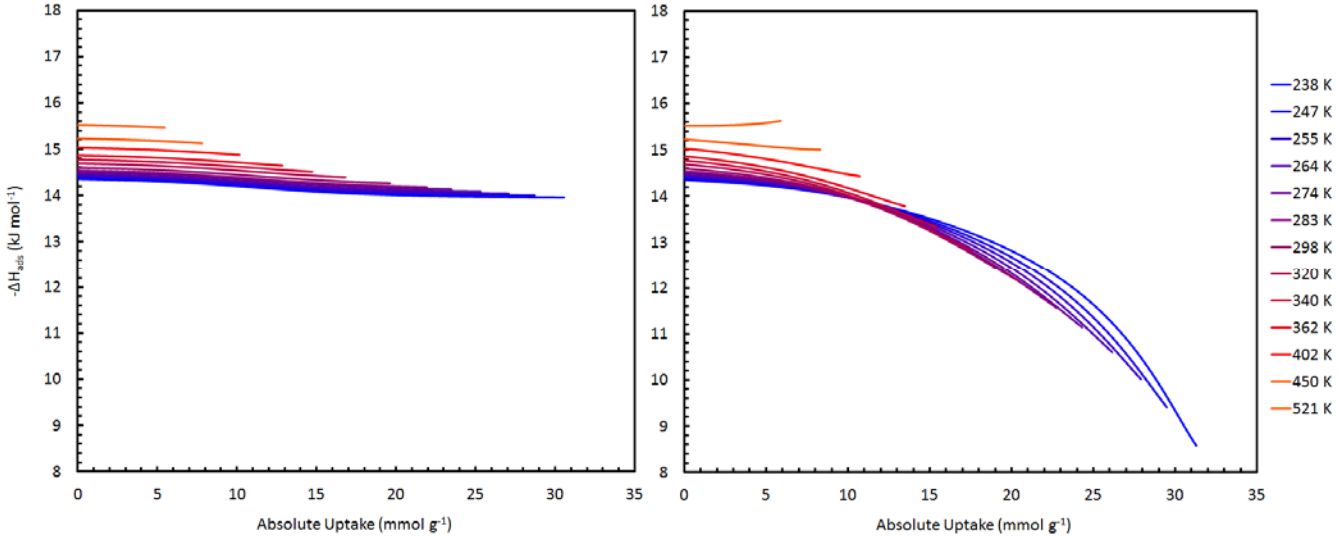

Figure 2.21. Isosteric enthalpy of adsorption, using double-Langmuir fits: (left) with the ideal gas assumption (Equation 2.31), and (right) with the real gas density (Equation 2.32), both employing the typical molar volume assumption.

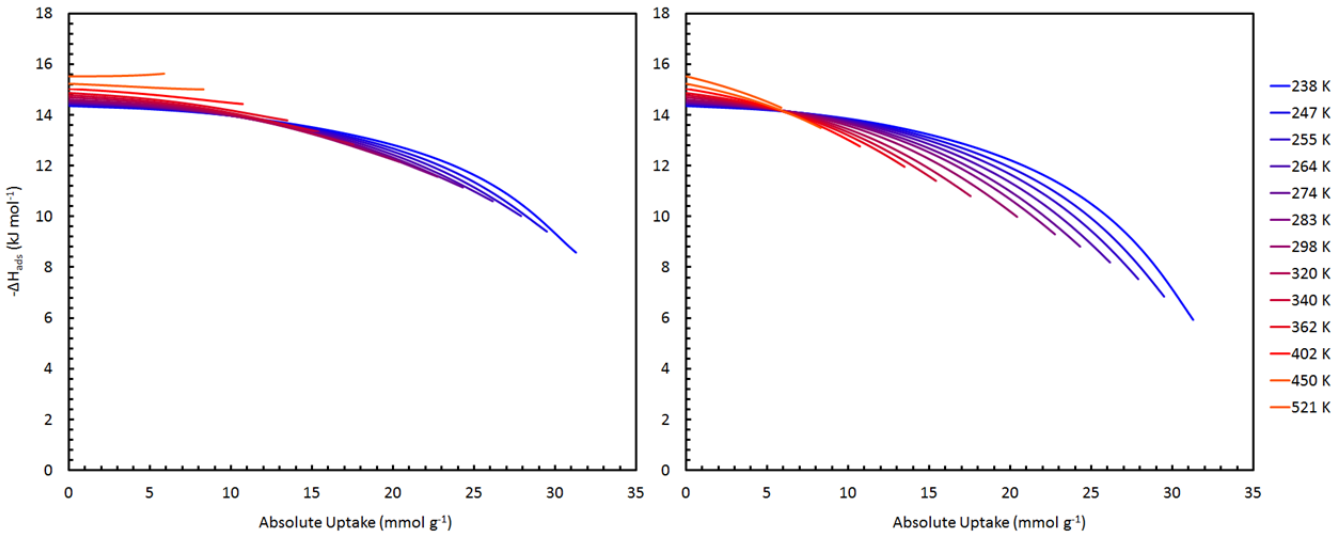

Figure 2.22. Isosteric enthalpy of adsorption, using double-Langmuir fits and real gas density: (left) with the typical molar volume assumption (Equation 2.32), and (right) with the suggested liquid methane approximation (Equation 2.36).

omitted from the calculations in this study. We suggest that a general exception be made for adsorption in the significantly non-ideal gas regime where there is no reason to suggest that the isosteric enthalpy of adsorption would persist to a plateau value.

Secondly, the change in molar volume on adsorption must also be carefully considered at high pressure for certain adsorptives, where the molar volume in the gas phase approaches that of its liquid. This is not the case across a wide temperature and pressure regime for hydrogen, for example, but is highly relevant to methane even at temperatures near ambient. For methane adsorption on MSC-30 in this study, the usual approximation, treating the adsorbed phase volume as negligible compared to that of the gas phase, holds in the low pressure limit but becomes invalid beyond 1 MPa. The difference in isosteric heat calculated with or without the approximation is >1% beyond 1 MPa, as shown in Figure 2.22. To approximate the molar volume of the adsorbed phase, we suggest to use that of liquid methane (see Equations 2.36-37), a fixed value that can be easily determined and which is seen as a reasonable approximation in numerous gas-solid adsorption systems. Specifically for methane, we use $v_a = v_{liq} = 38$ mL mol^{-1}, the value for pure methane at 111.5 K and 0.1 MPa. For our data of methane on MSC-30, the difference between the molar volume of the gas and the adsorbed phases becomes significant at all temperatures since v_a is 5-30% the magnitude of v_g at 10 MPa. The variation of the liquid molar volume with temperature and pressure was considered; the density along the vaporization line is ~20%, and so can be considered a negligible complication within the error of the proposed assumption. A fixed molar volume of the adsorbed phase was used throughout all temperatures and pressures.

2.6 Conclusions

In summary, the method used to determine the uptake and temperature dependence of the isosteric (or isoexcess) enthalpy of adsorption of methane on MSC-30 had a significant effect on the results. The virial-type fitting method has the advantage that with few parameters, one can fit experimental isotherm data over a large range of P and T in many systems. The best fits to Equation 2.42 are found for systems with a weakly temperature dependent isosteric heat. For high temperatures (near the critical temperature and above) and up to modest pressures, this equation often suffices with only 2-4 parameters (i = 0-1). However, application of this fitting procedure to moderately high (defined as near-critical) pressures or low temperatures (where a Gibbs excess maximum is encountered) lends substantial error to the interpolated results even with the addition of many parameters. In every case implementing the isoexcess assumption, the enthalpy diverged at high uptake where the assumption is fundamentally invalid. It is simple to show that since $n_e < n_a$, the slope of the excess isosteres in the van't Hoff plot will be more negative than that of the correct absolute isosteres (since the pressure necessary to achieve a given state of uptake will be underestimated), effecting a perceived increase in the calculated enthalpy of adsorption. Pitfalls such as these are commonly ignored, or the data beyond moderate quantities of surface coverage are discarded. In any case, the isosteric enthalpy is not accessible for high pressures using this method, and quantities calculated using excess uptake data must be referred to as "isoexcess" quantities to distinguish them from true isosteric values based on absolute adsorption.[33]

A double-Langmuir-type equation with a built-in definition of Gibbs surface excess was a suitable fitting equation of methane uptake on MSC-30 in the model-independent case, and could also be used as a model to determine the absolute quantity of adsorption and to perform a true isosteric enthalpy analysis. In both the isoexcess and absolute results, the enthalpy of adsorption showed physically justifiable characteristics, and gave a Henry's law value closest to that for a model-free analysis of the low-pressure data. All simplifying approximations within the derivation of the isosteric enthalpy of adsorption were found to be extremely limited in validity for methane adsorption within a pressure and temperature range close to ambient. Therefore, real gas equation of state data must be used and a simple approximation of the finite molar volume of the adsorbed phase was proposed.

2.7 References

(1) J. E. Lennard-Jones, 'Processes of adsorption and diffusion on solid surfaces', *Trans. Faraday Soc.,* **28**, 333-359 (1932).

(2) J. D. van der Waals, 'Over de continuiteit van den gas- en vloeistoftoestand', thesis, Leiden (1873).

(3) J. C. Maxwell, 'On the dynamical evidence of the molecular constitution of bodies', *Nature,* **11**, 357-359 (1875).

(4) H. K. Onnes, 'Expression of the equation of state of gases by means of series', *Proc. Sect. Sci. Konink. Akad. Weten. Amsterdam,* **4**, 125-147 (1901).

(5) J. E. Jones, 'On the determination of molecular fields. II. From the equation of state of a gas', *Proc. R. Soc. Lond. A,* **106**, 463-477 (1924).

(6) J. E. Lennard-Jones, 'Cohesion', *Proc. Phys. Soc.,* **43**, 461 (1931).

(7) A. W. Gauger and H. S. Taylor, 'The influence of temperature, pressure, and supporting material for the catalyst on the adsorption of gases by nickel', *J. Am. Chem. Soc.,* **45**, 920-928 (1923).

(8) R. A. Beebe and H. S. Taylor, 'A rapid method for the determination of heats of adsorption and some values for hydrogen on nickel and copper', *J. Am. Chem. Soc.,* **46**, 43-52 (1924).

(9) F. London, 'Zur theorie und systematik der molekularkräfte', *Z. Phys. A,* **63**, 245-279 (1930).

(10) F. London, 'The general theory of molecular forces', *Trans. Faraday Soc.,* **33**, 8b-26 (1937).

(11) V. A. Parsegian, *Van der Waals forces*, Cambridge University Press, New York (2006).

(12) J. K. Johnson and M. W. Cole, 'Hydrogen adsorption in single-walled carbon nanotubes', *Adsorption by carbons*, Elsevier, 369-401 (2008).
(13) O. Talu and A. L. Myers, 'Molecular simulation of adsorption: Gibbs dividing surface and comparison with experiment', *AIChE J.,* **47**, 1160-1168 (2001).
(14) R. Rajter and R. H. French, 'Van der Waals-London dispersion interaction framework for experimentally realistic carbon nanotube systems', *Int. J. Mat. Res.,* **101**, 27-42 (2010).
(15) F. Rouquerol, J. Rouquerol, and K. S. W. Sing, *Adsorption by powders and porous solids: principles, methodology, and applications*, Academic Press, San Diego (1999).
(16) S. J. Gregg and K. S. W. Sing, *Adsorption, surface area, and porosity*, Academic Press, London (1982).
(17) S. Brunauer, P. Emmett, and E. Teller, 'Adsorption of gases in multimolecular layers', *J. Am. Chem. Soc.,* **60**, 309-319 (1938).
(18) J. W. Gibbs, 'On the equilibrium of heterogeneous substances', *Trans. Conn. Acad.,* **III**, 108-248 (1876), 1343-1524 (1878).
(19) S. Sircar, R. Mohr, C. Ristic, and M. B. Rao, 'Isosteric heat of adsorption: theory and experiment', *J. Phys. Chem. B,* **103**, 6539-6546 (1999).
(20) F. O. Mertens, 'Determination of absolute adsorption in highly ordered porous media', *Surf. Sci.,* **603**, 1979-1984 (2009).
(21) R. J. Olsen, 'Investigations of novel hydrogen adsorption phenomena', thesis, University of Missouri (2011).
(22) J. Purewal, D. Liu, A. Sudik, M. Veenstra, J. Yang, S. Maurer, U. Müller, and D. J. Siegel, 'Improved hydrogen storage and thermal conductivity in high-density MOF-5 composites', *J. Phys. Chem. C,* **116**, 20199-20212 (2012).
(23) R. T. Jacobsen and R. B. Stewart, 'Thermodynamic properties of nitrogen including liquid and vapor phases from 63K to 2000K with pressures to 10,000 bar', *J. Phys. Chem. Ref. Data,* **2**, 757-922 (1973).
(24) E. W. Lemmon, M. L. Huber, and M. O. McLinden, 'NIST standard reference database 23: reference fluid thermodynamic and transport properties − REFPROP', Number Version 8.0 in Standard Reference Data Program (2007).
(25) L. Czepirski and J. Jagiello, 'Virial-type thermal equation of gas-solid adsorption', *Chem. Eng. Sci.,* **44**, 797-801 (1989).
(26) S. Tedds, A. Walton, D. P. Broom, and D. Book, 'Characterisation of porous hydrogen storage materials: carbons, zeolites, MOFs, and PIMs', *Faraday Discuss.,* **151**, 75-94 (2011).
(27) D. H. Everett and W. A. House, 'Adsorption on heterogeneous surfaces', *Colloid Science,* **4**, 1-58 (1983).
(28) G. Aranovich and M. Donohue, 'Determining surface areas from linear adsorption isotherms at supercritical conditions', *J. Colloid Interface Sci.,* **194**, 392-397 (1997).
(29) D. Saha, Z. Wei, and S. Deng, 'Equilibrium, kinetics, and enthalpy of hydrogen adsorption in MOF-177', *Int. J. Hydrogen Energy,* **33**, 7479-7488 (2008).
(30) S. Ono and S. Kondo, *Molecular theory of surface tension in liquids*, Springer-Verlag, Berlin (1960).
(31) G. L. Aranovich and M. D. Donohue, 'Adsorption isotherms for microporous adsorbents', *Carbon,* **33**, 1369-1375 (1995).
(32) A. Chakraborty, B. B. Saha, S. Koyama, K. C. Ng, and S.-H. Yoon, 'Thermodynamic trends in the uptake capacity of porous adsorbents on methane and hydrogen', *Appl. Phys. Lett.,* **92**, 201911-201913 (2008).
(33) S. Sircar, 'Gibbsian surface excess for gas adsorption – revisited', *Ind. Eng. Chem. Res.,* **38**, 3670-3682 (1999).

Chapter 3

Hydrogen Spillover in Platinum-Doped Superactivated Carbon

3.1 Overview

Effective storage of hydrogen by physisorbent materials has remained limited to cryogenic temperatures since hydrogen binding interactions are not significantly larger than the average thermal energy at 298 K: typically 4-6 kJ (mol H_2)$^{-1}$. The excess adsorption capacities of known materials are less than 10 mmol g^{-1} (2 wt%), and less than 5 mmol g^{-1} in all but a few select cases. These figures do not include the added mass of the storage vessel and delivery apparatus, and are far from the targets suggested by the DOE for mobile vehicle applications. The volumetric density enhancement from hydrogen adsorption at room temperature has also not been shown to be significant enough to overcome the penalty in mass of including the sorbent.

It was proposed that an enhancement of the hydrogen storage capacities of physisorptive materials can be gained by hydrogen spillover from a metal catalyst onto the adsorbing surface.[1-7] Hydrogen spillover is dissociative chemisorption of dihydrogen onto a metal particle followed by migration of hydrogen atoms onto the surface of the bulk material and subsequent diffusion away from the receptor site,[8-10] as shown in

Figure 3.1. Platinum, palladium, and nickel have been studied as metal catalysts for spillover, while materials including zeolites, metal-organic frameworks (MOFs), and carbons were used as host materials.

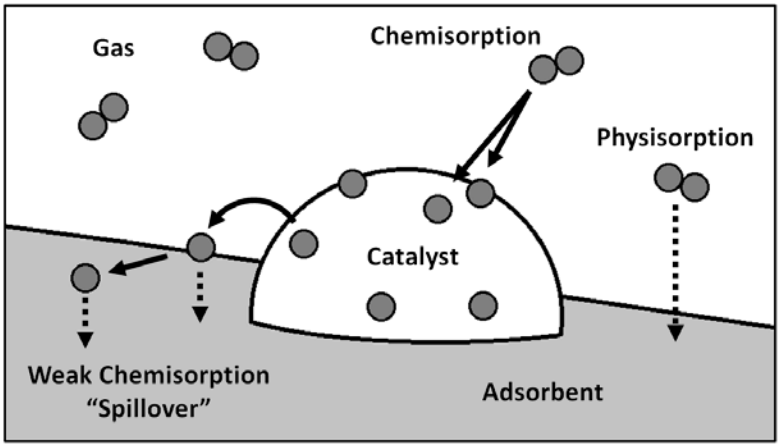

Figure 3.1. Spillover of the dissociated atoms of a diatomic molecule following chemisorption at the site of a catalyst particle, onto the surface of the support material.

The spillover concept is well documented in heterogeneous catalysis,[10] but has only recently been studied as a hydrogen storage mechanism. Reports of remarkable increases in hydrogen uptake for these systems have generated much further research, even toward enhancing contact between the metal sites and the substrate surface via carbonized "bridges".[4] However, the details of hydrogen spillover are not understood. This is partly because of the challenging task of detecting atomic hydrogen in spillover systems and partly because of the inherent difficulties in accurately measuring small changes in hydrogen uptake at room temperature. Although direct observation of atomic hydrogen has been recently demonstrated by transmission electron microscopy on a single graphene sheet,[11] volumetric measurements of hydrogen uptake are never this sensitive. Investigations using inelastic neutron scattering also recently yielded

evidence of the formation of new C-H bonds on the surface of activated carbon fibers after spillover from palladium clusters; however, reversibility was unclear and enhancement attributed to spillover was not tested at high pressures.[5] Interestingly, theoretical models cannot account for the remarkable enhancement of hydrogen uptake capacity in carbon materials due to spillover reported by experimental investigation.[5, 12-14]

In the present study, the hydrogen spillover effect was tested in the simplest experimental system. Platinum nanoparticles directly dispersed on high surface area superactivated carbon were used as the metal receptor sites for hydrogen dissociation. Platinized carbon was the standard system studied in the discovery of the spillover phenomenon,[8] the benzene hydrogenation experiments that later confirmed the spillover mechanism,[9] and in the first reports of spillover enhancement to hydrogen storage capacity.[1, 2] Platinum metal does not form a bulk hydride phase and therefore only surface chemisorption is expected (unlike palladium where absorbed hydrogen is a complication). While “bridging” is reported to increase hydrogen uptake by spillover,[4] this phenomenon is not essential for spillover to occur and was not the topic of this study. A commercially available superactivated carbon (Maxsorb MSC-30) was selected for its close similarity to AX-21, a high surface area carbon material previously used in spillover experiments. Hydrogen uptake isotherms of the platinum containing samples (Pt-MSC-30) were measured at room temperature (296 K), where spillover is expected. Synthesis and adsorption experiments were carried out in the most straightforward and standard way for corroborating the effect, following the steps reported by Li and Yang.[3]

In all 0.2 g samples, the size used in previous spillover studies, H_2 uptake was not substantially above instrumental background as measured by standard volumetric techniques. In experiments using a larger sample (>3 g), specific excess hydrogen uptake in Pt-MSC-30 was well above background, but was found to be less than in unmodified MSC-30 at high pressures.

3.2 Materials Processing and Synthesis

3.2.1 MSC-30 and AX-21

Maxsorb MSC-30 superactivated carbon was obtained from Kansai Coke & Chemicals Company, since it is a suitable support material for catalyst nanoparticles, essentially equivalent to AX-21 (from Anderson Development Co.) previously used in spillover experiments.[3] Both materials are produced by activation of petroleum coke with molten KOH, using a process patented by Standard Oil Company (later, Amoco Corporation).[15] Both have a surface area near 3000 m^2g^{-1}, exhibit similar chemical character and textural morphology, and are classified as "superactivated" or "AX-21 type" carbon.[16] The oxygen content of superactivated carbon, a characteristic which may be important to the hydrogen spillover mechanism,[17] is proportional to the BET surface area and is expected to be similar for both materials.[18]

3.2.2 Synthesis Methods

Maxsorb MSC-30 superactivated carbon (obtained from Kansai Coke & Chemicals Company, Ltd.) was stored at 393 K under vacuum in a Buchi glass oven. The Pt-MSC-30 samples were prepared by incipient wetness impregnation, in an analogous method as

for Pt/AX-21.[3] For each sample, 200 mg of dried MSC-30 was dispersed in acetone and magnetically stirred for 30 min at room temperature. A 2 mL solution consisting of 50 mg H_2PtCl_6 in acetone was then added dropwise to the stirring MSC-30 solution over 5 min. The slurry was removed and placed in an ultrasonic bath (50 W, 42 kHz, 1.9 L capacity) for 60 min and then magnetically stirred at room temperature for 24 h. The acetone was evaporated by heating the sample at 333 K for 12 h. The dry mixture was transferred to a ceramic boat and immediately placed in He flow inside a horizontal quartz tube furnace to prevent moisture uptake. The furnace was pre-heated to 393 K and held for 2 h under constant He flow. For reduction, the gas flow was switched to H_2 and the furnace was heated to 573 K and held for 2 h. The flow was again returned to He and the furnace allowed to cool to room temperature over 30 min. Each sample (~0.2 g) was sealed in a glass vial in Ar atmosphere and stored in a glovebox. A large number of 0.2 g Pt-MSC-30 samples (~40) were prepared and then combined to achieve sample sizes up to 3.2 g. Adapting the synthesis procedures of Pt/AX-21[3] to make large sample sizes required the use of multiple ceramic boats placed in a large diameter (5 cm) tube furnace. Sample characterization was undertaken to assure that individual syntheses yielded consistent products before combining them. Prior to hydrogen adsorption, the samples were degassed in vacuum at 623 K for 12 h. Sample mass, measured in the degassed state, was varied from 0.2-3.4 g for isotherm experiments of Pt-MSC-30 and pure MSC-30.

3.3 Materials Characterization

3.3.1 Nitrogen Adsorption

Nitrogen isotherms were measured at 77 K for MSC-30 and Pt-MSC-30. These measurements were made with a Micromeritics ASAP 2420 and surface areas were calculated using the BET method as implemented by Micromeritics ASAP 2420 version 2.02 software. The BET surface areas of MSC-30 and Pt-MSC-30 were measured to be 3420 m^2g^{-1} and 2810 m^2g^{-1}, respectively. The surface area of MSC-30 is larger than that of Anderson AX-21, reported as 2880 m^2g^{-1}.[3] The decrease in surface area of MSC-30 upon adding Pt nanoparticles is consistent with the reported data for AX-21. This can be explained by Pt particles blocking or filling pores in the superactivated carbon.

3.3.2 X-Ray Diffraction

X-ray diffraction (XRD) experiments were performed using a PANalytical X'Pert Pro powder diffractometer with Cu $K\alpha_{1,2}$ radiation. Diffraction patterns of MSC-30 and

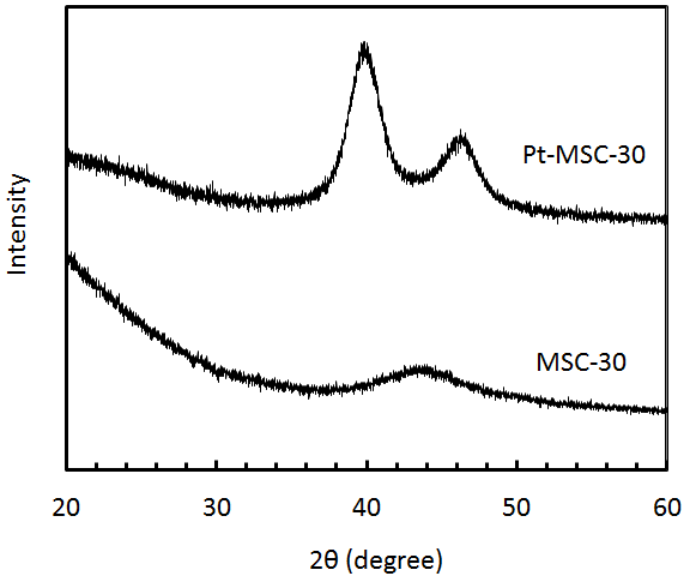

Figure 3.2. XRD patterns of Pt-MSC-30 and unmodified MSC-30.

Pt-MSC-30 are shown in Figure 3.2. The broad peak centered at 2ϑ = 43° for pure MSC-30 is consistent with that reported for AX-21. The peaks in the Pt-MSC-30 pattern at 2ϑ = 39.9° and 46.4° are the (111) and (200) reflections of the cubic platinum crystal structure. No platinum oxide peaks were detected, suggesting fully reduced Pt metal nanoparticles in the sample. From the widths of the diffraction peaks, the mean crystallite diameter was calculated with the Scherrer equation to be 3.6 nm (using the Scherrer constant K = 0.83 for spherical particles).[19]

3.3.3 Transmission Electron Microscopy

High resolution transmission electron microscopy (TEM) images were collected on a Tecnai TF30 operated at 300 keV. Scanning transmission electron microscopy (STEM) images were acquired with a high angle annular dark field (HAADF) detector. Samples were prepared for TEM by dispersing a finely ground mixture of Pt-MSC-30 and isopropanol on a holey carbon grid. TEM studies on Pt-MSC-30 showed a distribution in size of Pt particles from 2-10 nm in diameter, consistent with the 7 nm size from the Scherrer equation. TEM images at three magnifications are shown in Figure 3.3. The nanoparticles were highly dispersed on the surface of the activated carbon in all areas examined. This was further verified by HAADF microscopy, where intensity is proportional to Z^2 (Z is atomic number); platinum scatters electrons much more strongly than the carbon support and was readily observed in the form of small nanoparticles throughout the material.

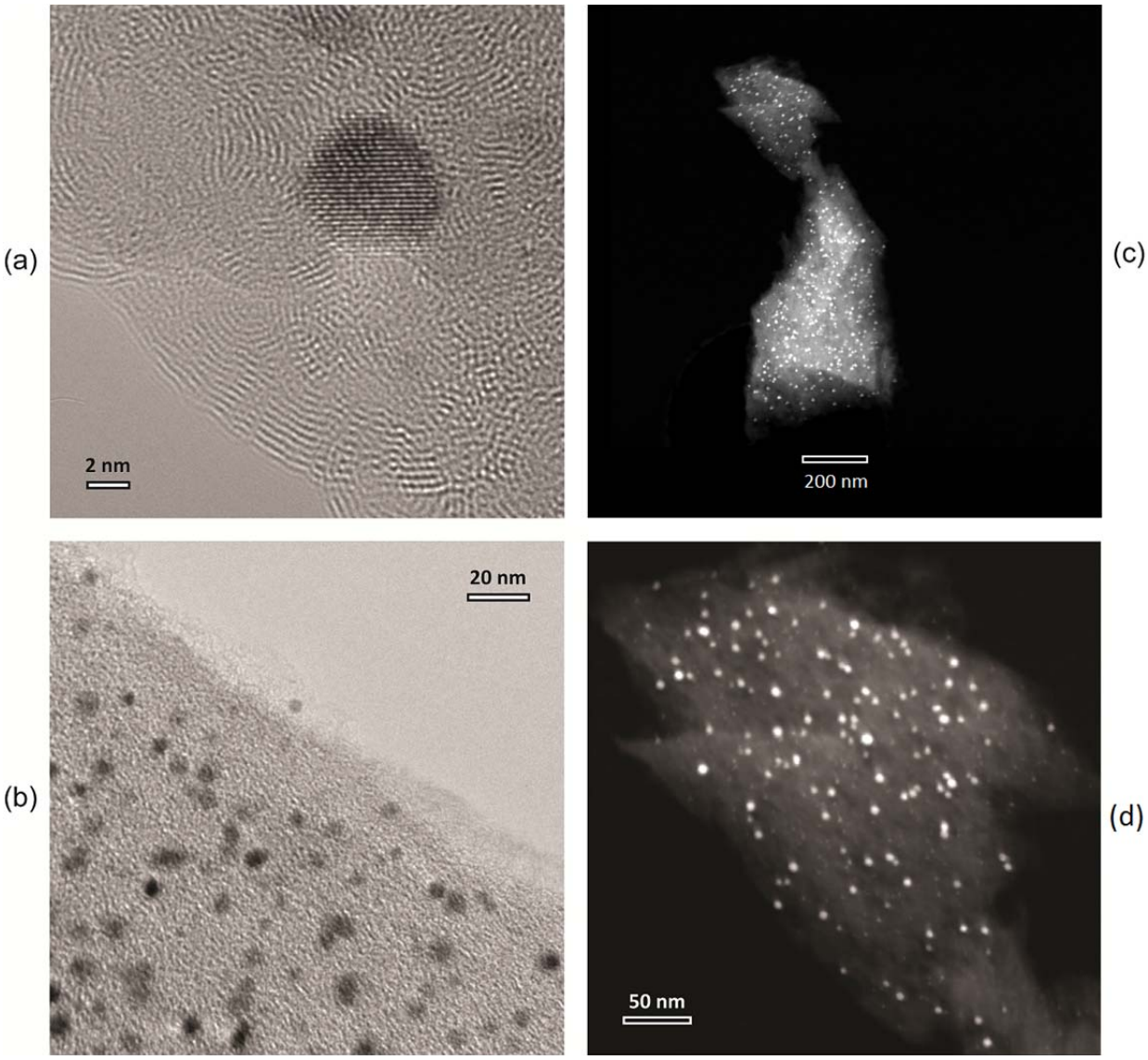

Figure 3.3. TEM micrographs of Pt-MSC-30 at (a) 4753000× and (b) 676600× magnifications. (c) STEM image obtained using a HAADF detector, verifying the successful dispersion of Pt nanoparticles throughout sample. (d) Higher magnification STEM image of an area in (c).

3.3.4 Thermal Gravimetric Analysis

Thermogravimetric analysis (TGA) was performed using a TA Instruments Q500 analyzer with a purge mixture of Ar/air in low flow (20 mL min^{-1}) and normal flow (70 mL min^{-1}) conditions, respectively. The temperature ramp was 10 °C min^{-1} to 100 °C, held at 100 °C for 30 min, then increased 10 °C min^{-1} to 1000 °C and held for 10 min. EDX data

was not consistent from region to region and was not a reliable method to determine the Pt content in Pt-MSC-30. Rather, platinum content was resolved from TGA data which showed a marked loss of mass between 375-415 °C, presumably oxidation of the organic components. The remaining mass at 1000 °C was attributed entirely to platinum and was 7.4% of the total. This value is less than the value of 12% predicted by stoichiometry for the synthesis.

3.4 Hydrogen Sorption

3.4.1 Experimental Methods

Hydrogen uptake isotherms were measured using a volumetric Sieverts apparatus. The system was leak tested over 1-20 h steps up to 7 MPa and showed a maximum leak rate of 1.4×10^{-5} mol h^{-1} of H_2. If fitted to an exponential decay function,

$$n(t) = n_0 \, \mathrm{e}^{-\mathrm{k}\,\mathrm{t}}$$

Equation 3.1

where k is the leak rate, this corresponds to a maximum leak of $k \sim 10^{-8}$ s^{-1} which is negligible for short time measurement.[20] The total volume of the apparatus, depending on the pressure gauge and sample holder selected, was 50-80 mL. The true volume of the sample was subtracted from the empty volume of the sample holder using a skeletal density of 2.1 g mL^{-1} measured by helium expansion. Hydrogen was exposed to the sample at incrementally higher pressures over the course of each isotherm in uniform equilibration steps, ranging from 0.5-24 h per step in different experiments. The system was not returned to vacuum in between steps and the measured hydrogen uptake was

cumulative from step to step. Hydrogen desorption was measured by an analogous method. The sample was evacuated to <1 mPa at room temperature between cycles.

3.4.2 Long-Duration Experiments

To measure the magnitude of the spillover effect at room temperature, unusually long measurements were necessary, sometimes exceeding 1 week in total duration. Even modest pressure (0.1-3 MPa) adsorption measurements of over 12 h duration showed significant scatter in all samples smaller than 0.5 g. Leakage, pressure history, and background adsorption were investigated. It was found that background adsorption in the empty sample holder at room temperature over long steps was comparable to the total uptake measured in 0.2 g samples. Equilibration time between isotherm steps and number of steps were varied to analyze these effects. Increasing the number of adsorption points and the duration of time for equilibration at each point significantly affected measured uptake, for measurements both with and without sample. The most effective approach to minimizing effects of background adsorption was to increase sample mass. It has been recommended that to avoid numerous pitfalls of hydrogen sorption experiments on carbon materials,[20, 21] a sample mass >1 g is best.

A custom-designed 20 mL sample holder was obtained for spillover measurements, accommodating approximately 3 g of sample. This allowed for significant increase in signal due to larger samples, but only a small increase in background. Of course, it is always necessary to subtract a unique background of empty sample holder adsorption from each isotherm measurement of a sample using the same number of isotherm points at roughly the same pressures and with identical technique.

3.4.3 Hydrogen Cycling

High-pressure hydrogen adsorption/desorption cycles were performed for multiple gram quantities of both MSC-30 and Pt-MSC-30, and are shown in Figures 3.4 and 3.5. Hydrogen uptake and delivery were identical after many cycles for MSC-30. Hydrogen uptake capacity for MSC-30 at room temperature and 7 MPa was 3.2 mmol g^{-1} (0.64 wt%). Using the same sample and degassing under vacuum at room temperature for 20 min between cycles, the standard deviation in this value was 0.0003 wt%. Complete desorption to 0.00 wt% at 0 MPa was achieved, with a standard deviation of 0.0006 wt%. Reloading the sample and performing the same adsorption/desorption cycles resulted in combined data which had a standard deviation of 0.003 wt%. This suggests that errors in determining the mass of the dried sample after cycling contributed to a small scatter in the data of different samples, a value within the bounds of usual experimental error.

Hydrogen uptake capacity in Pt-MSC30 was found to change on cycling. It was greatest during the first cycle (after degassing at 623 K under vacuum): 2.6 mmol g^{-1} (0.53 wt%) at 7 MPa and room temperature. Upon desorption, a hysteresis was observed. The desorption curve was extrapolated to 0 MPa, yielding a value of 0.02 wt% which could not be desorbed at room temperature for the first cycle. Using the same sample and degassing under vacuum at room temperature for 20 min between cycles, the uptake capacity at 7 MPa decreased to 0.52 wt% for subsequent cycles. Desorption under these conditions was possible to 0.02 wt% at 0 MPa in all cycles. If the sample is

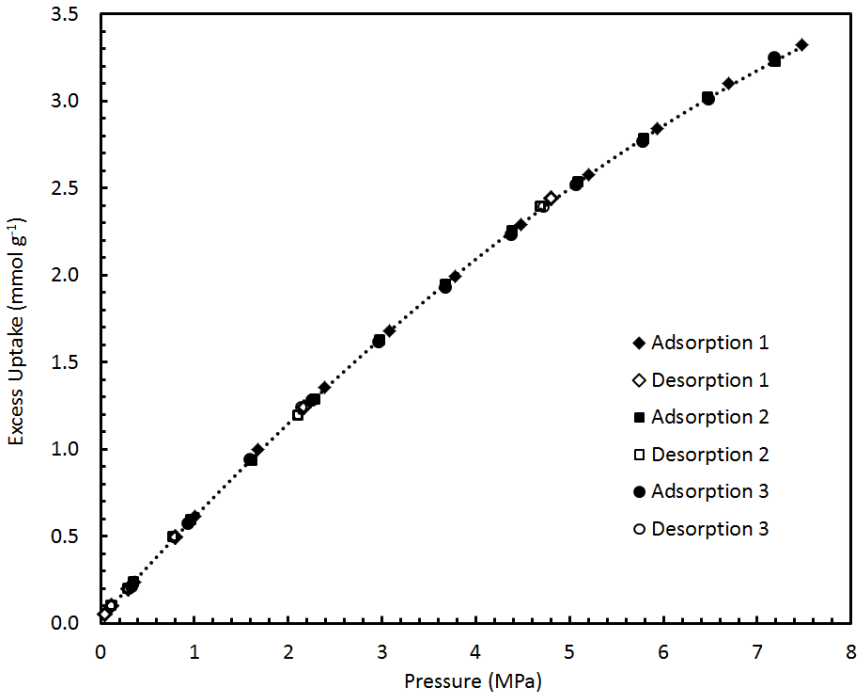

Figure 3.4. Equilibrium adsorption/desorption isotherms of H_2 on MSC-30 at 296 K during three consecutive cycles between 0-8 MPa.

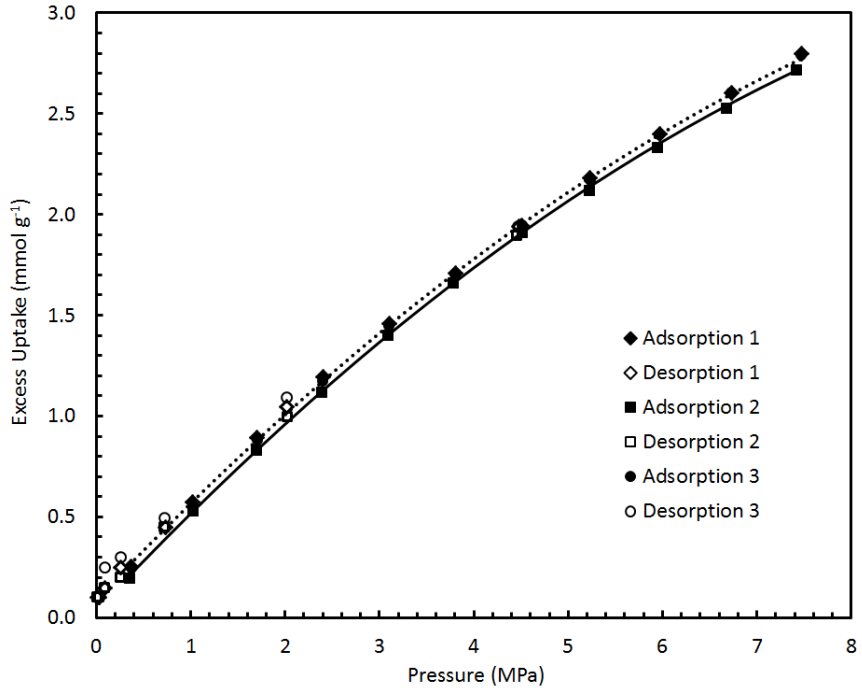

Figure 3.5. Equilibrium adsorption/desorption isotherms of H_2 on Pt-MSC-30 at 296 K during three consecutive cycles between 0-8 MPa.

instead degassed for 8 h between cycles, uptake at 7 MPa is again 0.53 wt%. The amount remaining after desorption is approximately equal to the amount chemisorbed by Pt-MSC-30 at low pressure (0-0.1 MPa). This implies that some hydrogen remains chemisorbed on the surface of the Pt nanoparticles during degassing after short times, but can be removed by evacuating the sample under vacuum overnight.

In the low-pressure regime hydrogen uptake data are collected by a high resolution pressure manometer that is then blocked off for measurements above 0.1 MPa. It can be seen that the high resolution data are consistent with the high-pressure data for large (~3 g) samples in Figure 3.6. Together, the data are used to interpolate the point of intersection of the two isotherm curves.

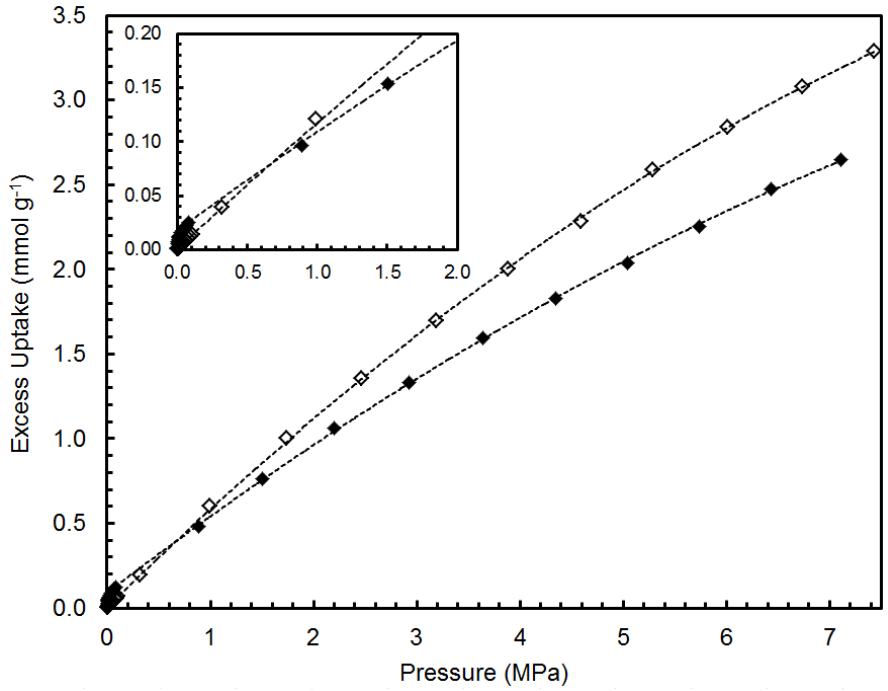

Figure 3.6. Fitted equilibrium adsorption isotherms for MSC-30 and Pt-MSC-30 at 296 K. The data is interpolated to intersect at 0.7 MPa and 0.08 wt%.

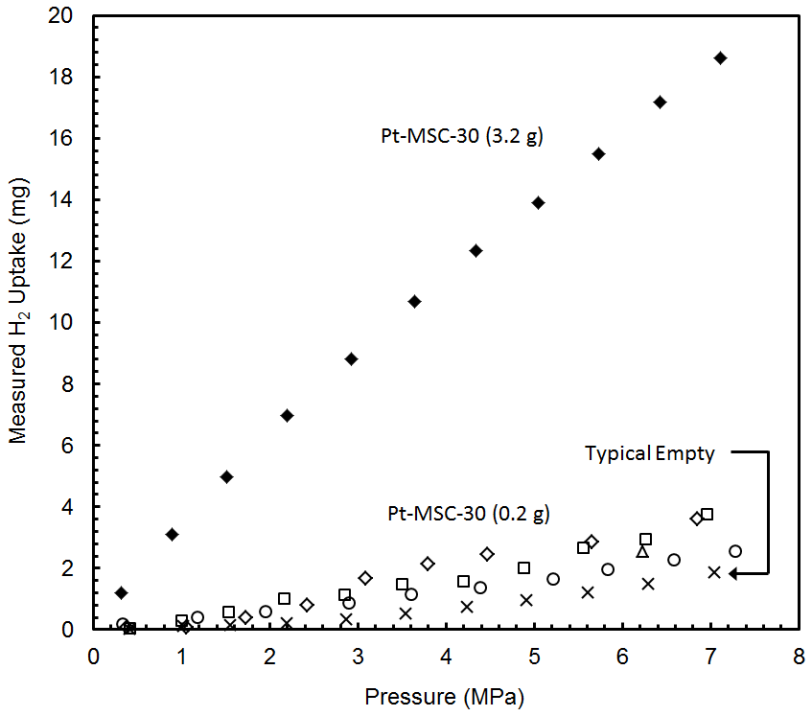

Figure 3.7. Equilibrium adsorption isotherms of H_2 on Pt-MSC-30 samples of varying mass compared to background adsorption by the empty sample holder (containing an aluminum blank) at 296 K. Uptake is shown in units of mass of H_2 detected as missing from the gaseous state, or "adsorbed" by the system.

3.4.4 Hydrogen Sorption Results

Hydrogen uptake isotherms were measured for MSC-30 and Pt-MSC-30 at room temperature, varying the sample size from 0.2-3.4 g. Similar isotherm measurements for aluminum blanks of comparable volume (0.1-1.5 mL) were used to determine the background adsorption of the empty sample holder. A comparison of measured hydrogen uptake (in mg H_2) as a function of pressure is shown for Pt-MSC-30 and an empty sample holder in Figure 3.7. In measurements with small samples (0.2 g), adsorption equilibrium was difficult to determine as room temperature fluctuations continued to slowly change pressure readings even after 60 minutes. Therefore,

equilibration step durations between 0.5-24 h were performed, and results compared. The room temperature isotherm data for small samples of Pt-MSC-30 showed uptake varying from 2.5-3.7 mg H_2 at 7 MPa with larger apparent uptake for longer time of measurement. Temperature changes of even 1 °C over the course of an isotherm step were also found to be highly correlated with large apparent uptake during that step. The problem may originate with the small temperature dependence of the pressure readings. This becomes a very important error for small samples at room temperature where the resolution of the pressure measurement has an important effect on the very small amount of uptake calculated. Hydrogen uptake in 0.2 g samples was a factor of 2 greater than the empty sample holder (background), but variations were also of this order (see Figure 3.7). In samples of mass >3 g, uptake was a factor of 10 greater than background and showed smooth curvature over the course of the experiment despite fluctuations in temperature.

Hydrogen uptake isotherms for large samples (>3 g) of Pt-MSC-30 and unmodified MSC-30 at room temperature, corrected for empty sample holder adsorption, are shown in Figure 3.8. Equilibrium was reached in less than 60 min between each isotherm step and was easily distinguished from continued adsorption. In pure MSC-30, the isotherm showed constant uptake as a function of pressure between 0-2 MPa. At pressures above 2 MPa, the slope decreased. At 6.7 MPa, hydrogen uptake in MSC-30 was 3.1 mmol g^{-1}, consistent with reported values for MSC-30 to within 0.3 mmol g^{-1}.[22, 23] This value was reproducible upon cycling to well within experimental error, to which we assign an upper bound of ±0.05 mmol g^{-1}. In Pt-MSC-30, low-pressure data showed a

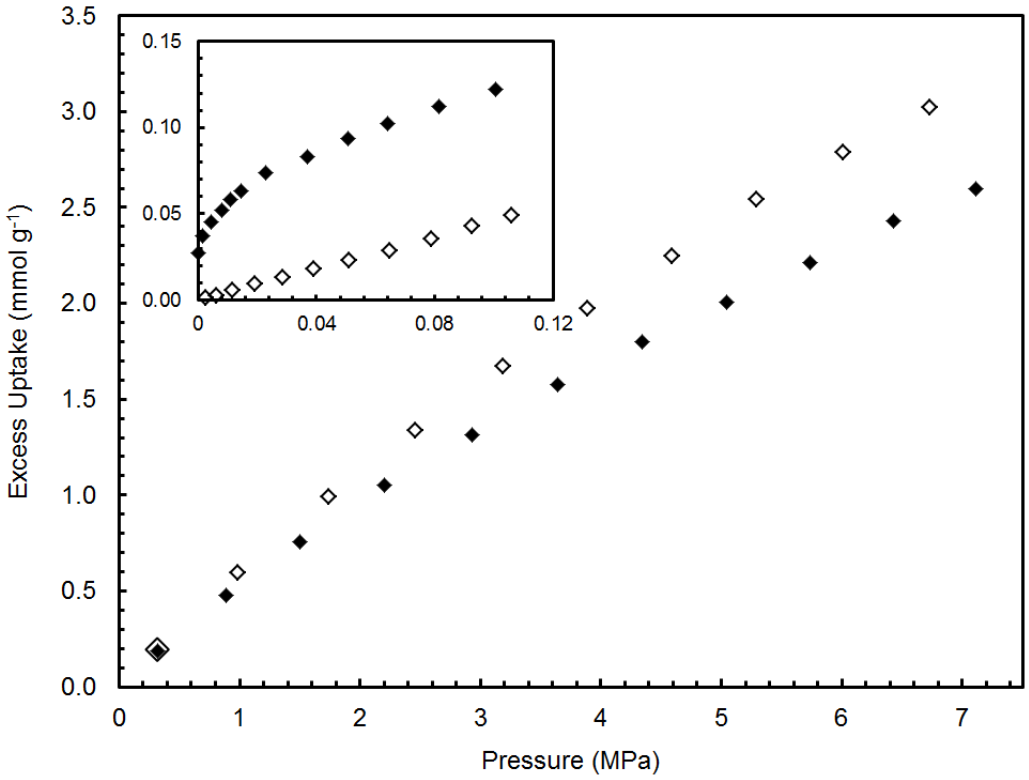

Figure 3.8. Equilibrium adsorption isotherms of H_2 on MSC-30 and Pt-MSC-30 at pressures up to 7 MPa at 296 K. Uptake is shown for large samples (>3 g).

steep initial uptake of hydrogen between 0-0.01 MPa and then a similar constant slope region to MSC-30 between 0.04-2 MPa. The slope of the isotherm in Pt-MSC-30 also decreased slowly at pressures above 2 MPa. Hydrogen uptake at 7.1 MPa was 2.7 mmol g^{-1} in the Pt containing sample on the first adsorption cycle, lower than for the unmodified MSC-30. This value decreased by up to 0.05 mmol g^{-1} in subsequent adsorption cycles. Interpolated hydrogen uptake values at 7 MPa are summarized in Table 3.1.

Table 3.1: BET surface areas (SA) and hydrogen uptake capacities reported for MSC-30, Pt-MSC-30, a similarly prepared Pt doped superactivated carbon, Pt/AX-21, and its precursor, AX-21.

Material	BET SA[†] (m^2g^{-1})	H_2 Uptake[‡] (mmol g^{-1})
MSC-30 [4]	2680	2.8-2.9
MSC-30 [5]	3250	3.0
MSC-30 *	3420	3.2
Pt-MSC-30 *	2810	2.6
AX-21 [8]	2880	2.5
Pt/AX-21 [8]	2518	4.5

* From this study. [†] Measured using N_2 at 77 K. [‡] Measured using H_2 at 300 K and 7 MPa.

3.5 Discussion

In pure MSC-30 at room temperature, the uptake of hydrogen showed Henry's law behavior in the low-pressure region as expected for low coverage physisorption on activated carbon. The Henry's law constant was 0.1 kg kg^{-1} MPa^{-1} at 296 K. The steep hydrogen uptake between 0-0.01 MPa in Pt-MSC-30 indicated very favorable initial chemisorption of hydrogen onto Pt nanoparticle surface sites. After these sites were filled, Henry's law physisorption of H_2 on the carbon surface occurred in Pt-MSC-30 as in unmodified MSC-30. The Henry's law constant for this physisorptive region was also found to be 0.1 kg kg^{-1} MPa^{-1} at 296 K, suggesting that the same adsorption mechanism is responsible for uptake in both the Pt-containing and unmodified samples at pressures above 0.01 MPa. As pressure increased, the slopes of both isotherms decreased from the Henry's law value due to increased interactions between adsorbed molecules. In Pt-MSC-30, this effect was more apparent because of the additional mass of the platinum.

At 0.7 MPa, the H_2 uptake isotherms intersected at 0.4 mmol g^{-1}. Similar results were also reported for Pd particles on a lower surface area Maxsorb variant.[24]

The addition of Pt nanoparticles to MSC-30 affects only the initial chemisorption at low pressure. The reduced uptake for the room temperature Pt-MSC-30 system at 7 MPa can be readily estimated by making the assumption that the individual contributions of the heavier Pt particle mass (7.4% of the sample) and reduced surface area carbon support (linearly rescaled) were simply additive. In this way, the H_2 uptake was calculated to be 2.5 mmol g^{-1}, close to the measured value. The difference between these values is attributed to a small amount of hydrogen chemisorbed on the surface of the Pt particles.

Spillover has been reported to dramatically enhance H_2 uptake in a similar system, Pt/AX-21, at room temperature, high pressure, and for 0.2 g samples over long (~1 h) equilibration steps between isotherm points.[3] All of these conditions risk substantial error accumulation using a standard Sieverts apparatus. Importantly, the sources of this error (leaks, temperature fluctuations, pressure hysteresis, and empty sample holder adsorption) are expected to cause an apparent *increase* in measured uptake, as opposed to a decrease. Small samples (0.2 g) of Pt-MSC-30 used in this study showed varying hydrogen uptake capacities in different experiments depending on the time allowed for equilibration, up to ±0.6 mg H_2 at 7 MPa and 296 K. Error of this magnitude may normally not be encountered at low (cryogenic) temperature and short equilibration time, or simply ignored when overall uptake mass is much higher in the material. However, for 0.2 g samples of Pt-MSC-30, this contributed an error in reported

uptake of ±1.5 mmol g^{-1} at 7 MPa and 296 K; this error is unacceptably high when the total uptake is 3.0 mmol g^{-1}.

Experiments that require adsorption measurements of carbonaceous materials at room temperature over relatively long equilibration steps must utilize large sample masses to remedy these errors. The same error of ±0.6 mg H_2 at 7 MPa and 296 K observed for a 3.2 g sample of Pt-MSC-30 is a factor of ten smaller in specific uptake (mmol g^{-1}), contributing a possible increase in measured uptake of up to 0.1 mmol g^{-1}. In large sample experiments, after an initial chemisorption at low pressure, platinum served only to increase the total mass of the sample and decrease available surface area for physisorption, thereby effecting a lower specific uptake of H_2 at high pressures.

3.6 Conclusions

If spillover occurred during hydrogen uptake in Pt-MSC-30, it was below the detection limit of volumetric gas adsorption experiments. The upper bound on the amount of hydrogen that participates in spillover is 0.005 mmol g^{-1} which is outside of the accuracy of storage capacity measurements and is not a substantial enhancement for practical applications. The presence of Pt particles on superactivated carbon proved ineffective for increasing hydrogen uptake by spillover. After a small chemisorption at pressures below approximately 0.1 MPa, the platinum served to increase the overall mass of the material and decrease the available surface area, thereby decreasing the overall capacity. Further studies of spillover, and a response to this work, is given in Appendix B.

3.7 References

(1) J. A. Schwarz, U.S. Patent 4,716,736 (1988).

(2) A. D. Lueking and R. T. Yang, 'Hydrogen spillover to enhance hydrogen storage – study of the effect of carbon physicochemical properties', *Appl. Catal., A,* **265**, 259-68 (2004).

(3) Y. Li and R. T. Yang, 'Hydrogen storage on platinum nanoparticles doped on superactivated carbon', *J. Phys. Chem. C,* **111**, 11086-94 (2007).

(4) Y. Li and R. T. Yang, 'Hydrogen storage in metal-organic frameworks by bridged hydrogen spillover', *J. Am. Chem. Soc.,* **128**, 8136-37 (2006).

(5) C. I. Contescu, C. M. Brown, Y. Liu, V. V. Bhat, and N. C. Gallego, 'Detection of hydrogen spillover in palladium-modified activated carbon fibers during hydrogen adsorption', *J. Phys. Chem. C,* **113**, 5886-90 (2009).

(6) D. Saha and S. Deng, 'Hydrogen adsorption on ordered mesoporous carbons doped with Pd, Pt, Ni, and Ru', *Langmuir,* **25**, 12550-60 (2009).

(7) M. Zieliński, R. Wojcieszak, S. Monteverdi, M. Mercy, and M. M. Bettahar, 'Hydrogen storage in nickel catalysts supported on activated carbon', *Int. J. Hydrogen Energy,* **32**, 1024-32 (2007).

(8) A. J. Robell, E. V. Ballou, and M. Boudart, 'Surface diffusion of hydrogen on carbon', *J. Phys. Chem.,* **68**, 2748-53 (1964).

(9) S. T. Srinivas and P. K. Rao, 'Direct observation of hydrogen spillover on carbon-supported platinum and its influence on the hydrogenation of benzene', *J. Catal.,* **148**, 470-77 (1994).

(10) W. C. Conner and J. L. Falconer, 'Spillover in heterogeneous catalysis', *Chem. Rev.,* **95**, 759-88 (1995).

(11) J. C. Meyer, C. O. Girit, M. F. Crommie, and A. Zettl, 'Imaging and dynamics of light atoms and molecules on graphene', *Nature,* **454**, 319-22 (2008).

(12) L. Chen, A. C. Cooper, G. P. Pez, and H. Cheng, 'Mechanistic study on hydrogen spillover onto graphitic carbon materials', *J. Phys. Chem. C,* **111**, 18995-9000 (2007).

(13) A. K. Singh, M. A. Ribas, and B. I. Yakobson, 'H-spillover through the catalyst saturation: an ab initio thermodynamics study', *ACS Nano,* **3**, 1657-62 (2009).

(14) G. M. Psofogiannakis and G. E. Froudakis, 'DFT study of the hydrogen spillover mechanism on Pt-doped graphite', *J. Phys. Chem. C,* **113**, 14908-15 (2009).

(15) A. N. Wennerberg and T. M. O'Grady, U.S. Patent 4,082,694 (1978).

(16) R. T. Yang, *Adsorbents: fundamentals and applications*, John Wiley & Sons, Inc. (2003).

(17) L. Wang, F. H. Yang, R. T. Yang, and M. A. Miller, 'Effect of surface oxygen groups in carbons on hydrogen storage by spillover', *Ind. Eng. Chem. Res.,* **48**, 2920-26 (2009).

(18) T. Otowa, Y. Nojima, and T. Miyazaki, 'Development of KOH activated high surface area carbon and its application to drinking water purification', *Carbon,* **35**, 1315-19 (1997).

(19) J. I. Langford and A. J. C. Wilson, 'Scherrer after sixty years: a survey and some new results in the determination of crystallite size', *J. Appl. Crystallogr.,* **11**, 102-13 (1978).

(20) T. Kiyobayashi, H. T. Takeshita, H. Tanaka, N. Takeichi, A. Züttel, L. Schlapbach, and N. Kuriyama, 'Hydrogen adsorption in carbonaceous materials – how to determine the storage capacity accurately', *J. Alloys Compd.,* **330-332**, 666-69 (2002).

(21) G. G. Tibbetts, G. P. Meisner, and C. H. Olk, 'Hydrogen storage capacity of carbon nanotubes, filaments, and vapor-grown fibers', *Carbon,* **39**, 2291-301 (2001).

(22) H. Nishihara, P. X. Hou, L. X. Li, M. Ito, M. Uchiyama, T. Kaburagi, A. Ikura, J. Katamura, T. Kawarada, K. Mizuuchi, and T. Kyotani, 'High-pressure hydrogen storage in zeolite-templated carbon', *J. Phys. Chem. C,* **113**, 3189-96 (2009).

(23) Y. Kojima, Y. Kawai, A. Koiwai, N. Suzuki, T. Haga, T. Hioki, and K. Tange, 'Hydrogen adsorption and desorption by carbon materials', *J. Alloys Compd.,* **421**, 204-08 (2006).

(24) A. Ansón, E. Lafuente, E. Urriolabeitia, R. Navarro, A. M. Benito, W. K. Maser, and M. T. Martínez, 'Hydrogen capacity of palladium-loaded carbon materials', *J. Phys. Chem. B,* **110**, 6643-48 (2006).

Chapter 4

Zeolite-Templated Carbon: Characterization and Hydrogen Adsorption

4.1 Overview

4.1.1 Background

Carbons with remarkably high surface areas (up to ~3000 $m^2\ g^{-1}$) can be made by conventional chemical activation, among other methods. However, weak hydrogen binding interactions (typically 4-6 kJ $(mol\ H_2)^{-1}$) limit the effective use of carbon materials to cryogenic temperatures and it is predicted that an ideal heat of adsorption for effective storage near ambient conditions is ~15 kJ mol^{-1}.[1] At 77 K, the Gibbs excess hydrogen uptake in carbon sorbents increases until a maximum value is reached, typically between 1-4 MPa; this value correlates linearly with the specific surface area of the material. "Chahine's rule" predicts ~2 wt% excess uptake of hydrogen, and is valid for a large number of different materials.[2, 3] This capacity is consistent with the theoretical value expected for hydrogen adsorbed in a $\sqrt{3}$ configuration on double-sided graphene sheets. Deviations from this trend are usually explained by increased or decreased surface binding interactions for a given surface chemistry or pore character, or by inaccuracies in measurement techniques.[4]

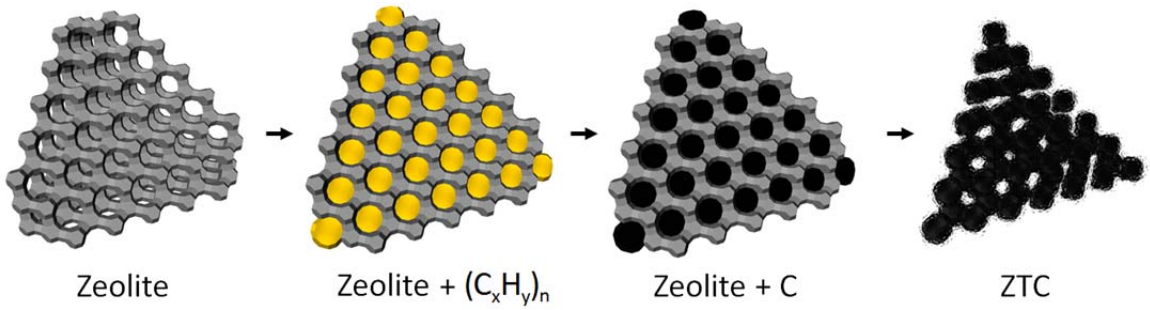

Figure 4.1. A schematic of template-carbonization in a porous zeolite framework, to produce zeolite-templated carbon (ZTC).

4.1.2 High-Pressure Hydrogen Storage

Significant hydrogen sorption capacity at or near room temperature is an important target for candidate storage materials, and numerous strategies to enhance adsorption in carbons have been proposed (e.g., "spillover," light-atom doping, etc.), but none has yet proven to be a viable technology. Since adsorption of hydrogen at room temperature is very weak, excess uptake in physisorbent materials at modest pressures (<10 MPa) is usually below 1 wt%. There is no general rule relating specific surface area to excess hydrogen uptake capacity at 298 K because a Gibbs surface excess maximum is not achieved. However, hydrogen uptake at a given pressure and 298 K is indeed known to be linearly correlated with specific surface area: ~0.2 wt% excess uptake of hydrogen per 1000 $m^2 g^{-1}$ at 6.5 MPa,[3] for example, an order of magnitude lower than at 77 K.

4.1.3 Zeolite-Templated Carbons

Template carbonization, among other methods of structural control, has also been explored as a technique to produce carbonaceous materials with exceptionally large specific surface area and finely tuned porosity.[5-12] It was reported in 2009 that a particular class of templated materials, zeolite-templated carbons (ZTCs), exhibits

remarkable hydrogen storage capacities at room temperature under high-pressure conditions (10-34 MPa).[7] This result was promising for applications of hydrogen storage at room temperature where modestly high pressures are not a barring limitation, and was highly relevant for mobile vehicle applications since hydrogen delivery has already been established up to 70 MPa on the public market (e.g., at the UC Irvine hydrogen station, since 2006).

The reported substantial increase of hydrogen uptake in ZTC "P7(2)-H" could not be explained by surface area alone; the uptake in ZTCs exceeded that of commercially available superactivated carbon of similar surface area, Maxsorb® MSC-30, by nearly 100% at 34 MPa. Extremely narrow microporosity in ZTCs was credited with the improvement, exhibiting optimal pore size for the accommodation of two layers of hydrogen in each pore.[8] However, heats of adsorption in these ZTCs did not show an increase, remaining below 8 kJ mol^{-1}, and the lack of any substantial changes to the thermodynamics is consistent with this explanation. Additionally, BET surface area is notoriously susceptible to error in highly microporous materials such as ZTCs, and may be a significant source of error in the characterization of uptake capacity per surface area at room temperature.

4.1.4 Further Investigation

Measurements of hydrogen adsorption in sorbent materials beyond 15 MPa are few, and most tend towards a plateau beyond 10 MPa at room temperature, while ZTCs are reported to continually increase in this high-pressure regime.[7] Further investigation of this effect was undertaken to ascertain the nature of this anomalous behavior. In the

present study, high surface area carbon sorbents were prepared by the zeolite-templating method; materials with BET surface areas of up to 3600 m^2 g^{-1} were produced in multi-gram quantities. Hydrogen uptake measurements of these materials at 77, 87, and 298 K were performed with multiple instruments to assess the viability of ZTCs as hydrogen storage materials for room temperature applications. A specially designed volumetric apparatus was constructed for this work and commissioned for measurements up to 70 MPa.

4.2 Materials Synthesis

To characterize the potentially unique hydrogen adsorption in ZTCs, materials which had properties meeting or exceeding those used in the previous report were necessary. It was found that synthesis of materials up to ~3000 m^2 g^{-1} was readily accomplished with simple laboratory infrastructure, but a limit was reached. High template fidelity was fully realized when experiments were performed together with HRL Laboratories using a converted CVD apparatus which could perform heating under high vacuum or in high purity inert gas conditions: materials with surface areas up to 3600 m^2 g^{-1} were synthesized. The method was readily scalable in both cases, yielding multi-gram quantities of product with ease.

4.2.1 Raw Materials

Zeolum® zeolite molecular sieve materials were obtained from Tosoh Corporation, specifically HSZ-320NAA (faujasite structure, Na cation, SiO_2/Al_2O_3 = 5.5 mol/mol) (NaY) and HSZ-930NHA (beta structure, NH_4 cation, SiO_2/Al_2O_3 = 27 mol/mol) (NHβ). Maxsorb

MSC-30 superactivated carbon was obtained from Kansai Coke & Chemicals Company, Ltd. Activated carbon CNS-201 was obtained from A. C. Carbons Canada Inc. These materials were stored at 150°C under vacuum in a Buchi glass oven before use. Zeolite-templated carbon (ZTC) materials were prepared at HRL and Caltech by previously established methods (a representative schematic is shown in Figure 4.1).[7]

4.2.2 Caltech Experiments

At Caltech, dried zeolite (<1 wt% H_2O) and furfuryl alcohol (98%, Sigma Aldrich) were combined at room temperature under reduced pressure. In the largest batches, 3 g of dried zeolite were added to 60 mL of furfuryl alcohol and magnetically stirred for 24 h. The zeolite-furfuryl alcohol mixture was collected by vacuum filtration and washed with excess mesitylene (99.0%, Sigma Aldrich) yielding 3.5 g of a white-gray powder. The dry powder was transferred to ceramic boats and placed in N_2 flow inside a horizontal alumina tube furnace, pre-heated to 80°C. Polymerization was performed under N_2 flow at 150°C for 12 h. Temperature was increased at 2°C min^{-1} to 700°C, and gas flow was then switched to a propylene/N_2 mixture (7% propylene) for 2 h. Gas flow was switched back to pure N_2 and temperature was increased at 10°C min^{-1} to 900°C. Carbonization at 900°C was performed for 3 h. The product, referred to as Z-C, was cooled to room temperature and transferred to a PTFE beaker, yielding 2.5 g. A 3 mL aqueous solution of HF (48%, EM Industries) was added dropwise to the Z-C, stirred, and allowed to dissolve for 2 h. The aqueous solution was further diluted in a large flask to 1200 mL. The remaining solid product, ZTC, was collected by vacuum filtration and washed with water. The ZTC was dried and stored at 150°C under vacuum in a Buchi glass oven. HF

treatment was repeated until no zeolite peaks remained in the x-ray diffraction (XRD) pattern, yielding 1 g of final product. By this method, two different ZTC samples were prepared: ZTC-1 from zeolite NHβ and ZTC-2 from zeolite NaY.

Experiments at Caltech lasted approximately 12 months until it was clear that limitations in control of inert atmosphere conditions during the synthetic process proved to be a barrier to achieving ultra-high surface areas. We reached ~2900 $m^2 g^{-1}$, but could not proceed to higher surface area or greater template fidelity. Further synthetic efforts were undertaken at HRL Laboratories, described below.

4.2.3 HRL Experiments

At HRL, 6.0 g of zeolite NaY was further dried at 450°C under vacuum for 8 h to <0.02 wt% H_2O. After cooling to room temperature, 12 mL of furfuryl alcohol (98%, Sigma Aldrich) was added by injection and the mixture was stirred under Ar atmosphere for 24 h. The zeolite-furfuryl alcohol mixture was collected via vacuum filtration and washed 4 times with 100 mL aliquots of xylenes. The washed powder was placed in a 8×8 cm shallow quartz boat and loaded into a 10 cm diameter quartz tube furnace/CVD reactor. The reactor was purged with Ar at room temperature, and was held at 80°C under Ar flow (2 L min^{-1}) for 24 h. Polymerization was performed at 150°C under Ar flow (2 L min^{-1}) for 8 h. Temperature was increased at 5°C min^{-1} to 700°C under Ar flow (2 L min^{-1}), and gas flow was then switched to a propylene/N_2 mixture (7% propylene, 3.2 L min^{-1}) for 4 h. Holding the temperature at 700°C, the reactor was purged under Ar flow (4 L min^{-1}) for 10 min. Temperature was increased to 900°C under Ar flow (2 L min^{-1}) and held for 3 h. The NaY-C product was cooled to room temperature and transferred to a

PTFE beaker where 200 mL of aqueous HF (48%, Sigma-Aldrich) were added. After 16 h, the ZTC was collected by vacuum filtration and washed 10 times with 50 mL aliquots of water. The ZTC was dried and stored at 150°C under vacuum in a Buchi glass oven, yielding 1.4 g of final product. A TGA measurement conducted in air up to 1000°C yielded a residual mass of ~2%, indicating nearly complete dissolution of the zeolite template. By this method, samples such as ZTC-3 were prepared.

By improving inert atmosphere conditions during combination of raw materials, polymerization, and carbonization, such as for ZTC-3, significant improvements in templating fidelity were observed. Careful control of inert atmosphere as well as thorough drying of the zeolite precursor was found to be critical for obtaining a product with surface area beyond 3000 $m^2 g^{-1}$.

4.3 Materials Characterization

4.3.1 Nitrogen Adsorption

Nitrogen isotherms were measured at 77 K with a BELSORP-max volumetric instrument (BEL-Japan Inc.) and surface areas were calculated using the BET method.[13] Equilibrium adsorption isotherms of N_2 at 77 K are shown in Figure 4.2. Pore-size distributions were calculated by the non-local density functional theory (NLDFT) method[14] from high-resolution data collected on a Micromeritics ASAP 2020, using a carbon slit pore model and software provided by Micromeritics. Other geometrical models were also explored, notably a unique carbon cylindrical pore model, but none showed a better fit to the data. Pore-size distributions of ZTC-3 and MSC-30 calculated

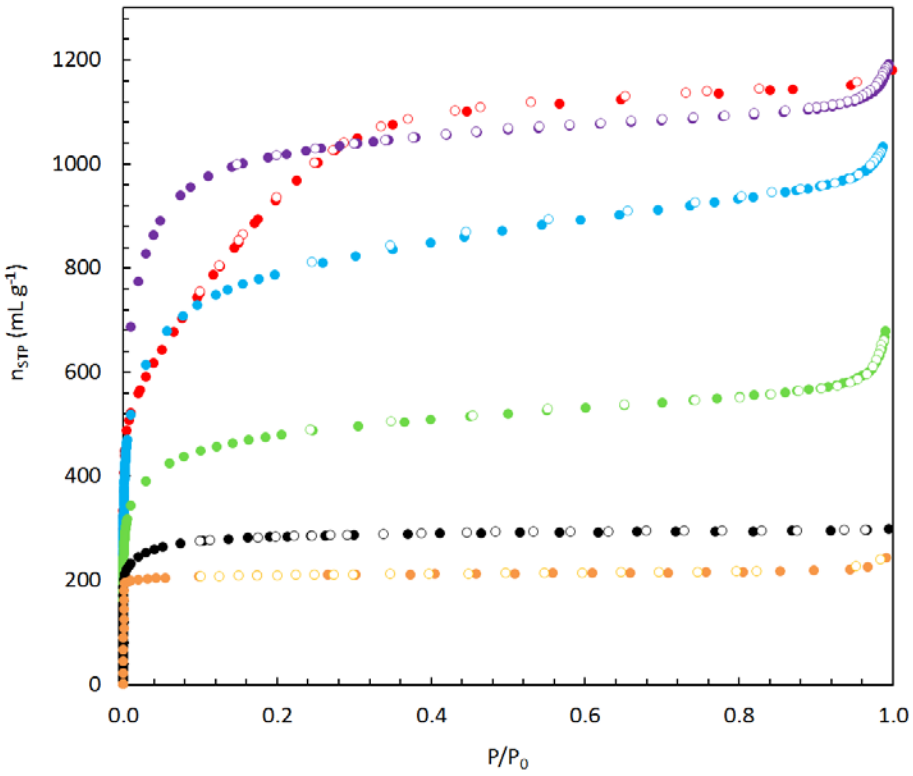

Figure 4.2. Equilibrium adsorption (closed) and desorption (open) isotherms of N_2 at 77 K on MSC-30 (red), ZTC-1 (green), ZTC-2 (blue), ZTC-3 (purple), CNS-201 (black), and zeolite NaY (orange). Uptake is expressed in units of volume of N_2 (at STP) per unit mass.

by the DFT method are shown in Figure 4.3. Distinct regularity of pore-size, centered at a width of 1.5 nm, can be seen for ZTC-3, which is consistent with other reports.[7] MSC-30 shows a broader and larger pore size distribution with significant pore volume in pores up to 3.5 nm wide. The BET surface area and Dubinin-Radushkevich (DR) micropore volume of each of the materials studied are summarized in Table 4.1. MSC-30 and CNS-201 were measured to have 3240 m^2g^{-1} and 1100 m^2g^{-1} BET surface areas, respectively. The BET surface area of MSC-30 was calculated in the region $0.0005 < P/P_0 < 0.35$, and is discussed further elsewhere[15]. All materials measured show high BET surface area and high relative uptake of N_2 in the linear region of the isotherm, among

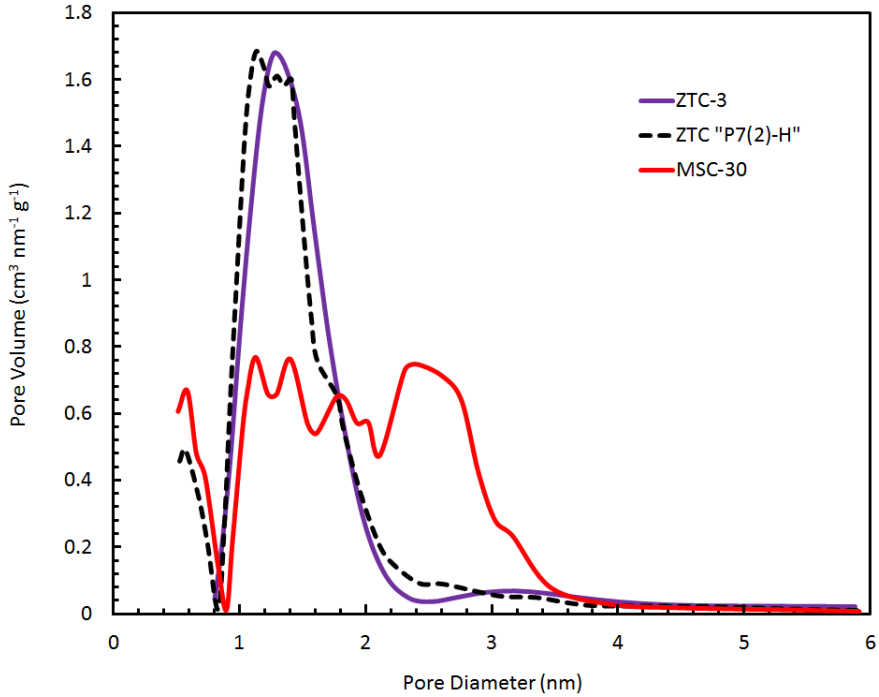

Figure 4.3. DFT pore-size distribution of ZTC-3 (purple) compared to MSC-30 (red) and ZTC "P7(2)-H" (dashed black), an equivalent reference material.[7]

Table 4.1. BET surface area (SA) and hydrogen uptake capacity reported for carbonaceous sorbent materials: CNS-201, MSC-30, and ZTCs.

Material	Density[◊] ($g\ mL^{-1}$)	BET SA ($m^2 g^{-1}$)	H_2 Capacity[†] ($mmol\ g^{-1}$)	High P H_2 Uptake[‡] ($mmol\ g^{-1}$)	$-\Delta H_0$ ($kJ\ mol^{-1}$)
CNS-201 *	2.1	1095 ± 8	12.7	2.48	8.6
MSC-30 *	2.1	3244 ± 28	27.9	7.66	6.7
ZTC-1 *	1.9	1691 ± 21	18.5	3.99	-
ZTC-2 *	1.9	2964 ± 18	26.1	6.45	6.6
ZTC-3 *	1.8	3591 ± 60	28.6	8.27	6.5
CNS-201 [20]	2.2	1440	12.9	-	-
MSC-30 [20]	2.2	3000	26.5	-	-
MSC-30 [7]	2.1	2680	-	5.5	7.3
P7(2)-H [7]	1.9	3800	-	10.7	8

* From this study. [◊] Skeletal density measured using He at 300 K between 0-3 MPa. [†] Measured using H_2 at 77 K and Gibbs excess surface maximum pressure. [‡] Measured using H_2 at 296-303 K and 30 MPa.

the highest known for carbonaceous materials. The DR calculations were found to be susceptible to similar pitfalls as the BET method, especially for MSC-30 which shows multiple stages of different slopes in the DR curve.

4.3.2 Carbon Dioxide Adsorption

Carbon dioxide adsorption studies were carried out on early samples of ZTC, specifically ZTC-1 and ZTC-2, for comparison to MSC-30, as discussed in Appendix C.

4.3.3 Skeletal Density Measurements

Helium pycnometry measurements were performed using a standard Sieverts apparatus at pressures between 0.1-3 MPa at 298 K. Ten to thirty measurements were performed and the average skeletal densities of the materials studied are summarized in Table 4.1. ZTC-1 and ZTC-2 were measured to be 1.9 g mL^{-1}, while ZTC-3 was measured to be 1.8 g mL^{-1} , a significant difference from the activated carbons studied (both 2.1 g mL^{-1}); the standard error was ±0.06 g mL^{-1} between samples. Previous measurements of carbon materials in our laboratory gave values of 2.12 ± 0.05 g mL^{-1} over numerous different carbon types, including MSC-30. The significantly lower skeletal densities in ZTCs result in ~1 mmol g^{-1} difference in the calculated excess hydrogen uptake at 30 MPa and 298 K. This significant difference must be taken into account for uptake calculations, and seems to be unique to ZTCs as discussed in Section 4.5.1.

4.3.4 X-Ray Diffraction

X-ray diffraction (XRD) experiments were performed using a PANalytical X'Pert Pro powder diffractometer with Cu $K\alpha_{1,2}$ radiation. Diffraction patterns of ZTC-2 and ZTC-3 are shown in Figure 4.4, compared to the pure zeolite NaY precursor and the composite

NaY-C material before HF treatment. Also shown is the calculated crystal structure of the faujasite (FAU) framework. The sharp peak centered at 2θ = 6° is the (111) reflection of the cubic zeolite structure. In the final products, ZTC-2 and ZTC-3, no zeolite peaks were detected except this longest periodicity corresponding to the channel-to-channel structure of the template (14 Å), suggesting complete removal of the template from the sample; the remaining peak verifies successful templating of the zeolitic framework in the ZTC. From the width of this diffraction peak, the length scale of the zeolitic order was calculated with the Scherrer equation to be 24 nm (using the Scherrer constant K = 0.83 for spherical particles) for ZTC-3.[16] The absence of other peaks confirms the amorphous nature of C-C bonding in ZTCs, and suggests the likelihood of a turbostratic microstructure between regions of pore-to-pore periodicity.

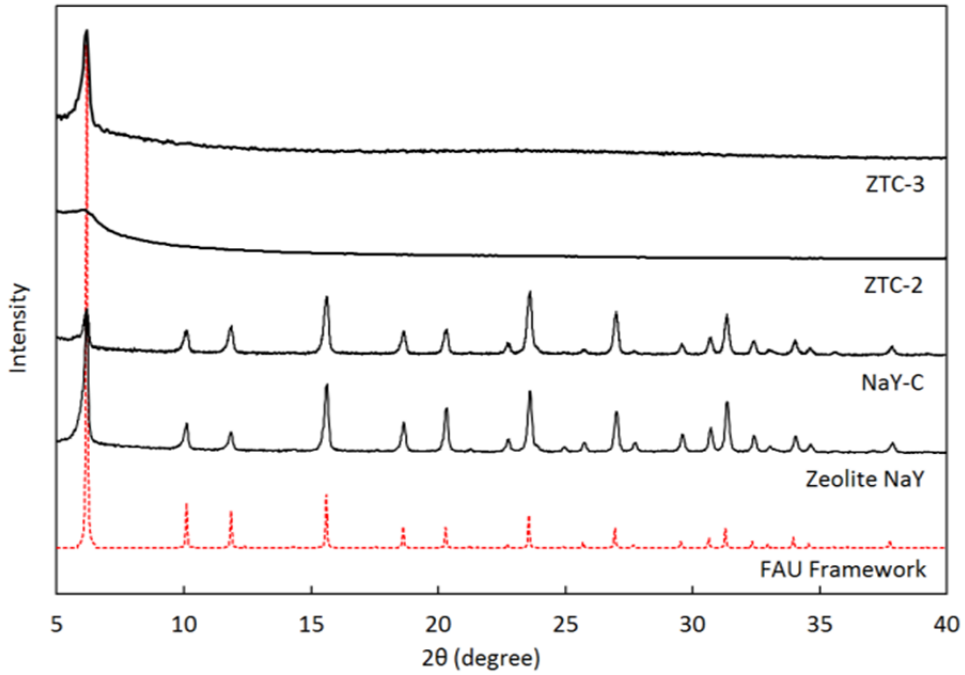

Figure 4.4. XRD patterns of final products ZTC-2 and ZTC-3, a composite zeolite-carbon intermediate product (NaY-C), pure zeolite NaY (as received), and the FAU zeolitic framework (calculated).

4.3.5 X-Ray Photoelectron Spectroscopy

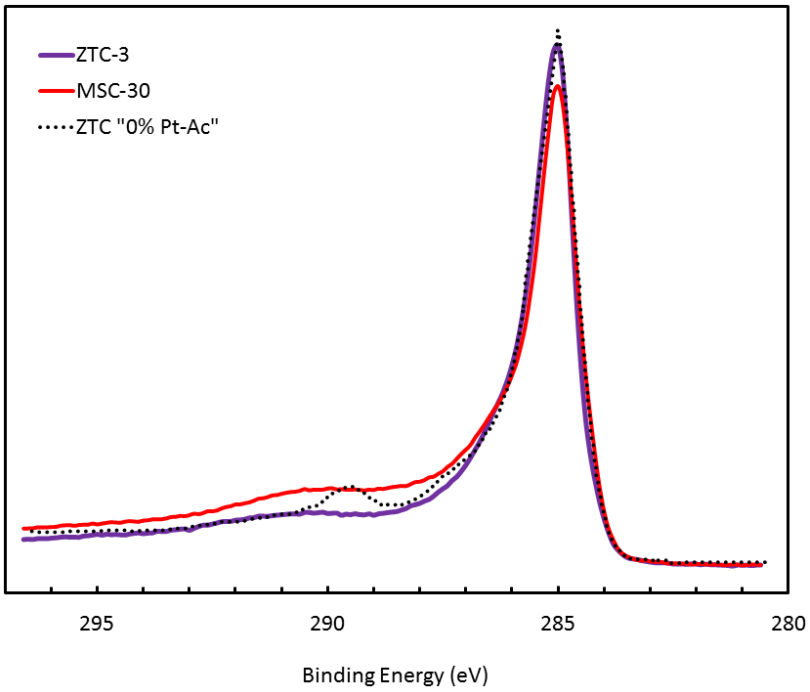

Figure 4.5. XPS data comparing ZTC-3, MSC-30, and an equivalent reference material, ZTC "0% Pt-Ac.".[16]

X-ray photoelectron spectroscopy (XPS) was performed to compare ZTCs to MSC-30, but no appreciable difference was found (see Figure 4.5). XPS studies were performed on a Kratos AXIS Ultra DLD spectrometer with a monochromatic Al-Kα source operating at 150 W, with a 20 eV pass energy, and 0.1 eV step (after brief survey spectra were collected). The binding energy was corrected to the most intense peak, which is from sp^2 hybridized carbon, at 285.0 eV. The intensity was not rescaled since identical instrumental conditions were used across all samples. For peak fitting analysis, a Shirley-type background was subtracted and 8 component peaks were fitted, following a previously reported procedure.[17] An example of peak fits is shown in Figure 4.6. The

results are summarized in Table 4.2, indicating 18% and 19% sp^3 hybridized carbon in ZTC-3 and MSC-30, respectively.

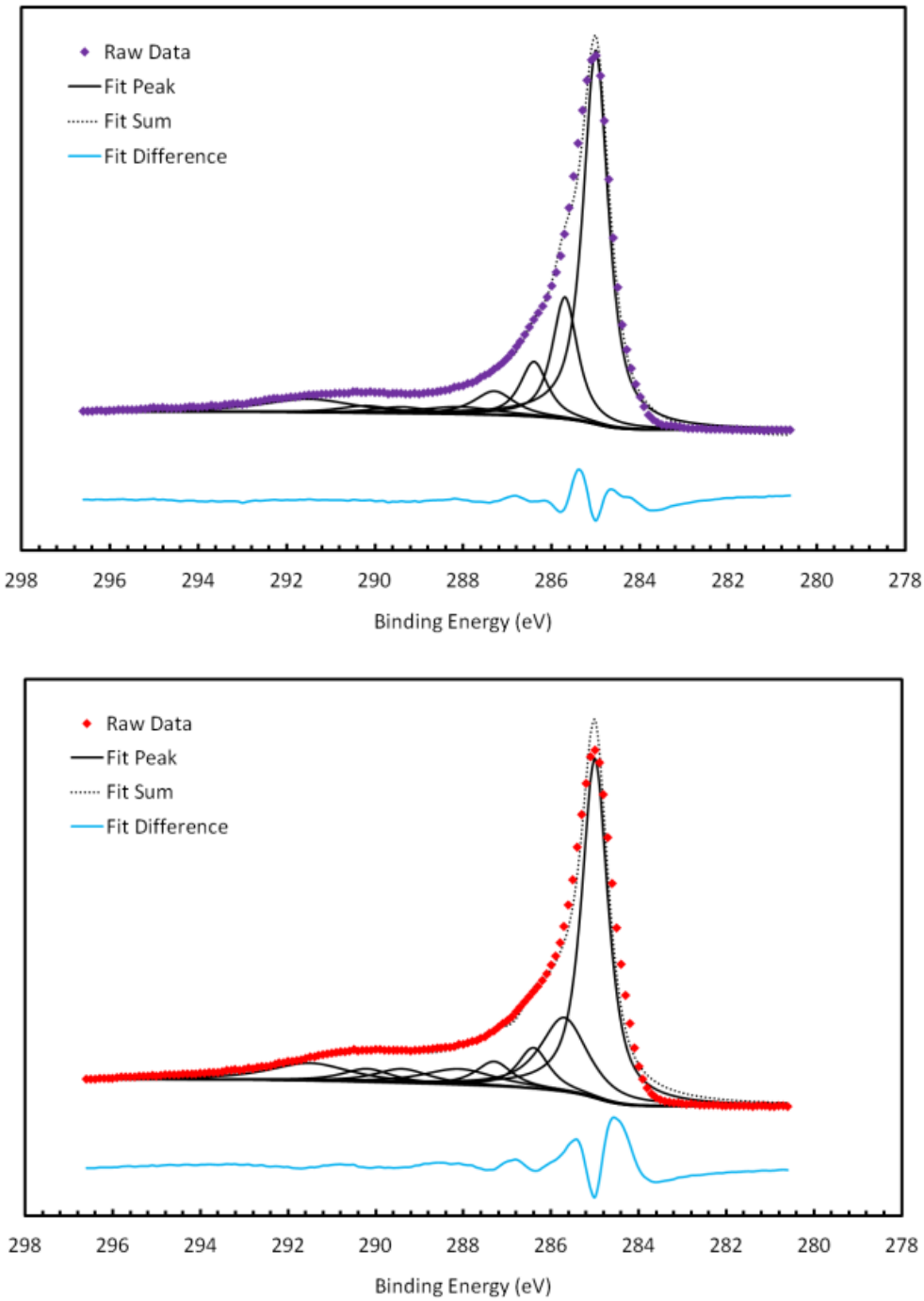

Figure 4.6. XPS analyses for the carbon 1s regions in ZTC-3 (top) and MSC-30 (bottom).

Table 4.2. Summary of the XPS analysis results for ZTC-3 and MSC-30.

	Component Fraction (at%)							
Peak Position (eV)	285.0	285.7	286.4	287.3	288.1	289.4	290.2	291.5
Component	C-C sp^2	C-C sp^3	C-OR	C-O-C	C=O	COOR	-	-
ZTC-3	53.4	18.0	8.6	6.0	1.1	4.2	1.0	7.7
MSC-30	48.0	18.8	6.8	4.8	6.1	4.2	3.6	7.7

4.3.6 Electron Microscopy

SEM studies were performed on a Hitachi S-4800 instrument operated at 4.0 keV. Samples were prepared for SEM by dispersing in isopropanol on a holey carbon grid. Evidence can be seen of the superficial likeness between particles of ZTC and the zeolite template from which they were synthesized (shown in Figure 4.7), similar to that reported by Ma et al.[18]

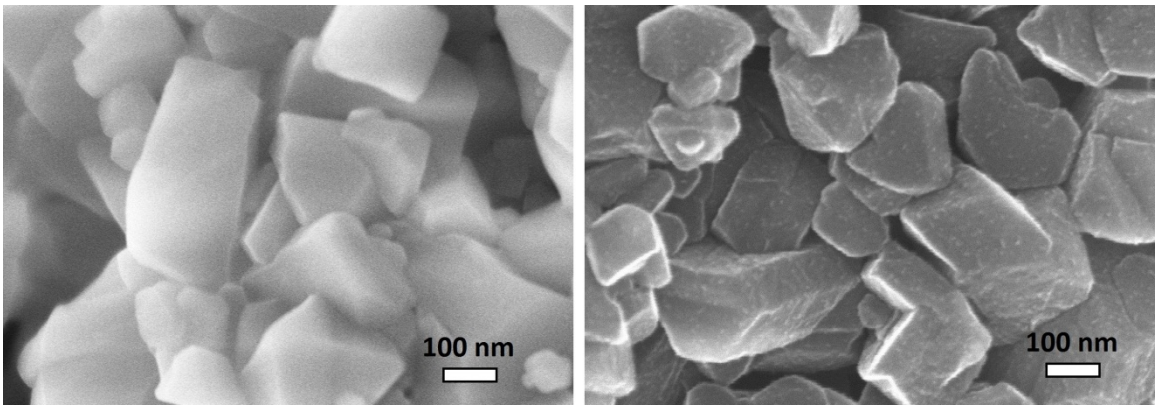

Figure 4.7. SEM micrographs of zeolite precursor (left) and ZTC product (right), showing similar particle size and shape.

TEM studies were performed on a FEI Tecnai F20 instrument operated at 200 keV. Samples were prepared for TEM by dispersing a finely ground mixture of ZTC and isopropanol on a holey carbon grid. Low magnification TEM studies were consistent with the SEM data. A high magnification micrograph of a thin region of ZTC-3 is shown in

Figure 4.8, with an inset showing the Fourier transform of the image. The spots in the transformed image confirm the periodicity of the porous structure. The pore-to-pore spacing of 1.0 nm is consistent with that calculated from DFT treatment of the N_2 adsorption isotherms at 77 K (see Figure 4.3), and with data reported by Ma et al.[18]

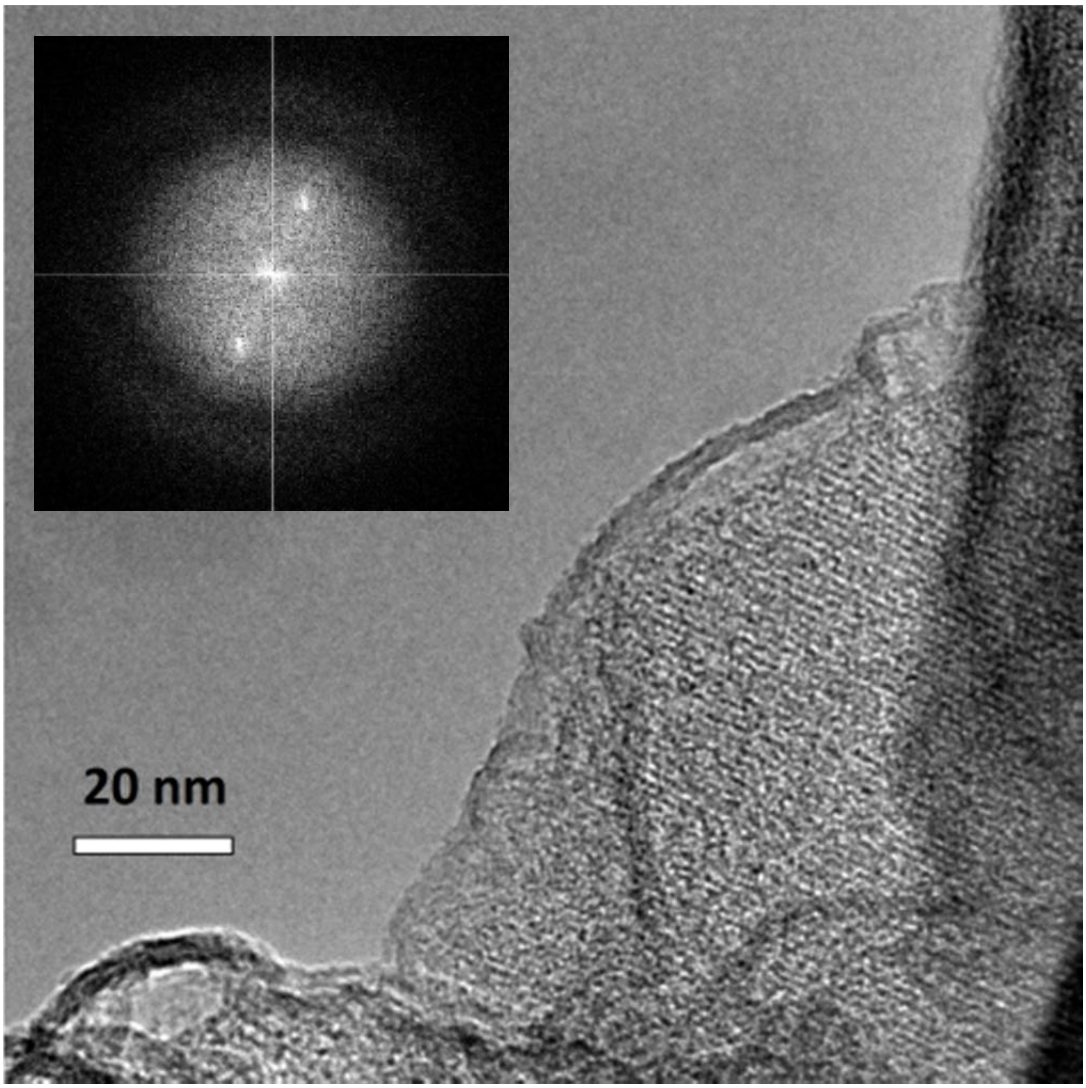

Figure 4.8. TEM micrograph of ZTC-3 showing pore-to-pore periodicity of 1.0 nm, and the Fourier transform of the image (inset).

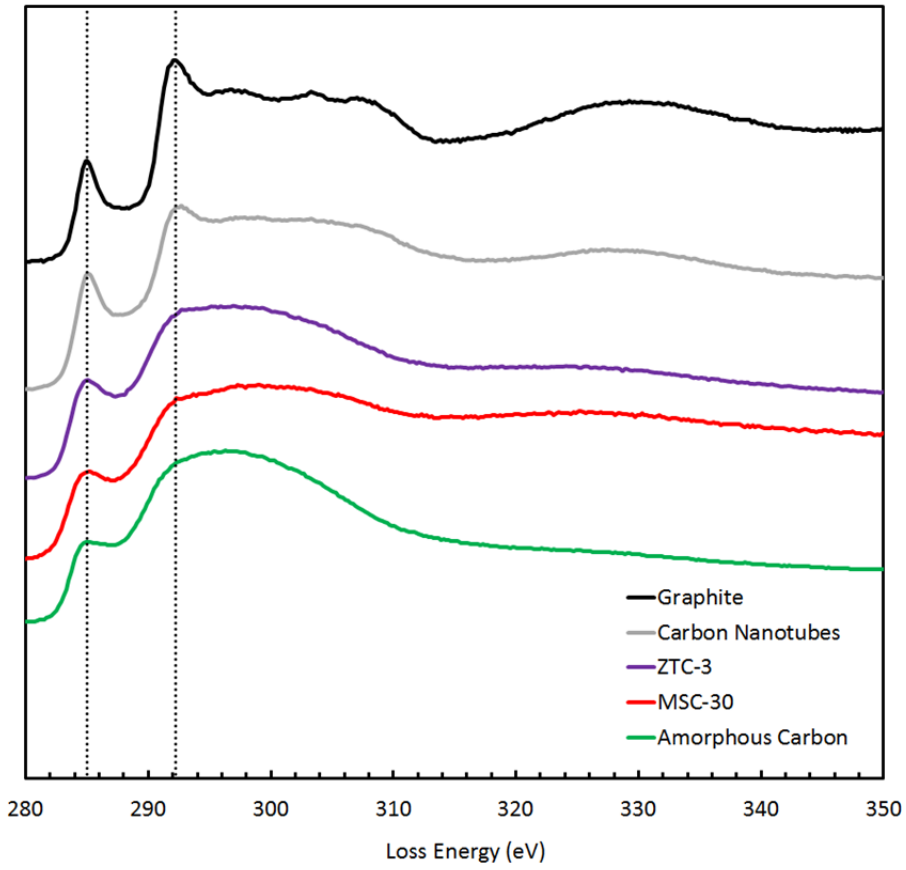

Figure 4.9. EELS spectra showing the carbon 1s edge in ZTC-3 compared to MSC-30, graphite, carbon nanotubes, and the amorphous holey carbon grid.

4.3.7 Electron Energy-Loss Spectroscopy

Electron energy-loss spectroscopy (EELS) was performed to compare ZTCs to MSC-30 and other carbon materials, shown in Figure 4.9. EELS measurements were performed on a FEI Tecnai F20 instrument operated at 200 keV and equipped with a Gatan Imaging Filter system. To acquire these spectra, the aperture size was 0.6 mm, the dispersion was 0.2 eV pixel^{-1}, and the energy shift was 175 eV. Samples were prepared by dispersing a finely ground mixture of sample material and isopropanol on a holey carbon grid. The pre-edge peak was calibrated to 285.0 eV in all samples, a power-law

background was subtracted, and the signal intensity was normalized to the same value at high loss. The ratio of the areas of the pre-edge peak to the main carbon 1s edge (>289 eV) was used to determine the relative content of sp^2 and sp^3 hybridized carbon (see Figure 4.10). This study also shows only a small difference in the amount of sp^2 and sp^3 hybridized carbon between ZTC-3 and MSC-30: approximately 18% and 16% sp^3 content, respectively.

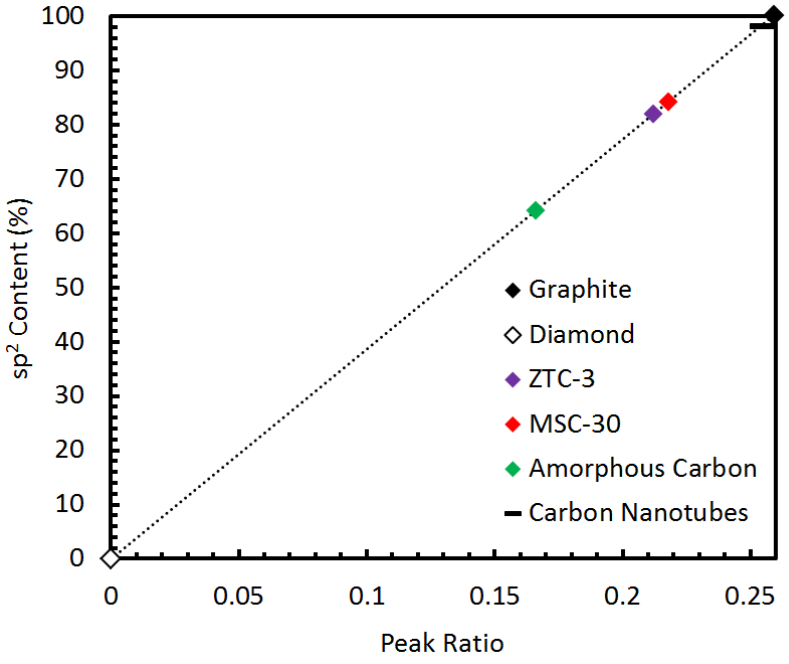

	◆	◇	◆	◆	◆	▬
P1 Area = I_{π^*}	1.54	0	1.96	1.95	1.55	2.08
P2 Area = I_{σ^*}	4.41	1	7.30	6.97	7.75	6.09
P1/P2	0.35	0	0.27	0.28	0.20	0.34
$I_{\pi^*}/(I_{\pi^*}+I_{\sigma^*})$	0.26	0	0.21	0.22	0.17	0.25
Normalized	1	0	0.82	0.84	0.64	0.98
sp^2 Content (%)	100	0	81.8	84.2	64.2	98.3

Figure 4.10. Summary of sp^2 content in carbon materials studied by EELS, based on the integrated peak areas of the 1s→π* peak at ~285 eV to the 1s→σ* peak at ~292 eV, and fit to a calibration curve established by graphite and diamond.

4.3.8 Solid-State Nuclear Magnetic Resonance

Solid-state ^{13}C NMR experiments were performed on ZTC-3 and MSC-30 using a Bruker DSX-500 spectrometer equipped with a Bruker 4 mm MAS probe (see Figure 4.11). The sample spinning rates were 12 kHz and 5 kHz for MAS and CPMAS, respectively, performed at room temperature under dry nitrogen gas. CPMAS measurements were performed with a RF field of 62.5 kHz during the CP contact period (0.1 ms). The chemical shifts are given in parts per million (ppm) externally referenced to tetramethylsilane. No significant sp^3 hybridized carbon (10-50 ppm region) in either ZTC-3 or MSC-30 was detected, consistent with previous measurements.[19]

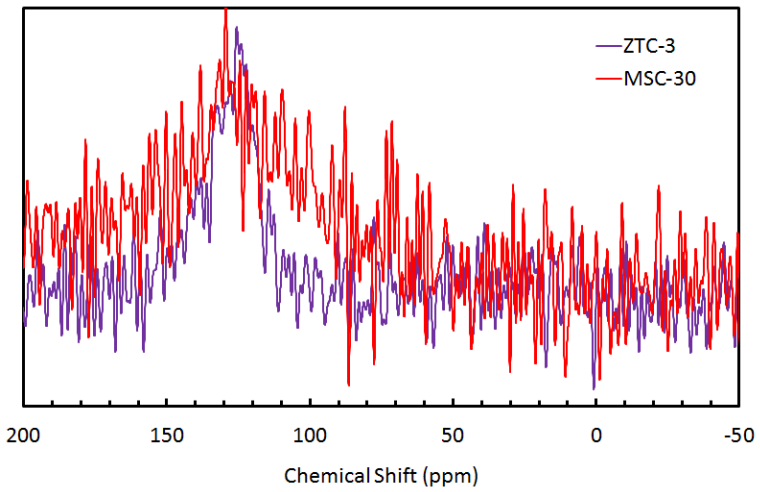

Figure 4.11. Solid-state ^{13}C NMR (MAS) spectra of ZTC-3 and MSC-30.

A cross-polarization ^{13}C MAS (CPMAS) study was also carried out, and compared to the MAS data, shown in Figure 4.12. The results are consistent with a previous report.[19] A peak fitting analysis was performed to determine the protonated content of carbon in the sp^2 peak. By deconvolution of the main peak into 3 components, it is calculated that ~89% of carbon ZTC-3 is protonated, from the contribution of the fit peak centered at

138 ppm. While an overestimate, this is consistent with results confirming high H content in ZTCs by elemental analysis experiments (see Section 4.5.1).

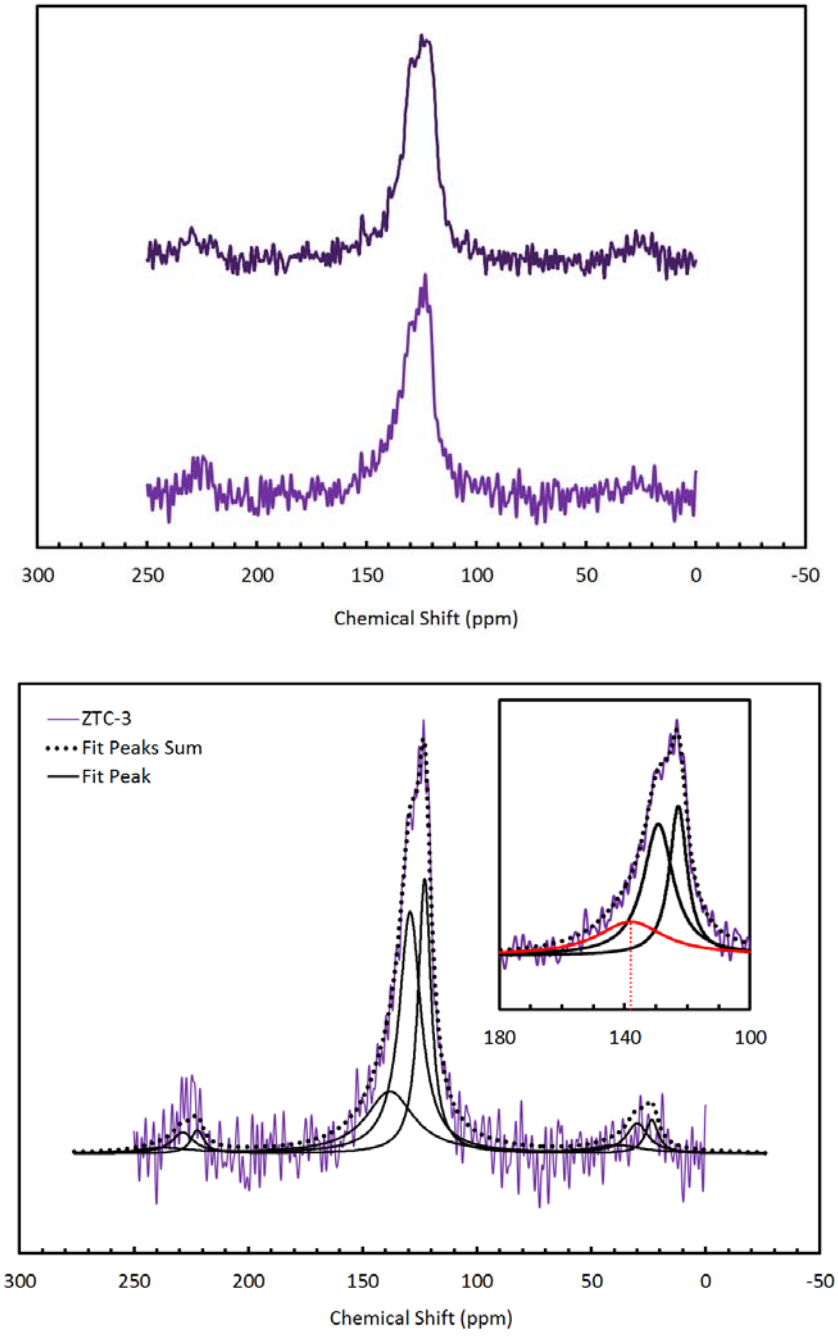

Figure 4.12. Solid-state ^{13}C MAS NMR spectrum of ZTC-3, fitted to three peaks (centered at 130, 136, and 138 ppm). The peak at 138 ppm was not present in CPMAS spectra, and is attributed to non-protonated sp^2 hybridized carbon, accounting for ~11% of the area of the total signal.

4.4 Hydrogen Adsorption

4.4.1 Standard-Pressure Experiments

Hydrogen adsorption isotherms were measured at 77 and 87 K from 0-7 MPa on the Sieverts I apparatus. Temperature baths of liquid nitrogen (77 K) and liquid argon (87 K) were continually filled throughout experiments to maintain low temperature conditions in the sample cell if necessary. The system was leak checked up to 7 MPa and showed a maximum leak rate of 6.0×10^{-7} mol h^{-1} of H_2. If fitted to an exponential decay function (see Equation 3.1) where k is the leak rate, this corresponds to a maximum leak of k ~ 10^{-9} s^{-1} which is well within the acceptable limit for accurate measurements.[20] During measurements, the system was not returned to vacuum between steps, and the measured hydrogen uptake was cumulative.

4.4.2 High-Pressure Experiments

Hydrogen adsorption isotherms at 298 K were measured up to 30 MPa on the Sieverts II apparatus. The temperature of the sample was not controlled, but remained within ±0.3 K. High pressures were achieved by gas densification in a coil submerged in a liquid nitrogen bath that was removed to allow the coil to return to ambient temperature. Hydrogen uptake was determined in cumulative steps, as in Section 3.4.1. The system was leak tested up to 45 MPa and showed a maximum leak rate of 2.2×10^{-7} mol h^{-1} of H_2. This corresponds to a maximum leak of k ~ 10^{-8} s^{-1}. Hydrogen uptake isotherms measured on MSC-30 using Sieverts II were compared to isotherms collected on Sieverts I and the gravimetric balance at EMPA, and were consistent from 0-10 MPa.

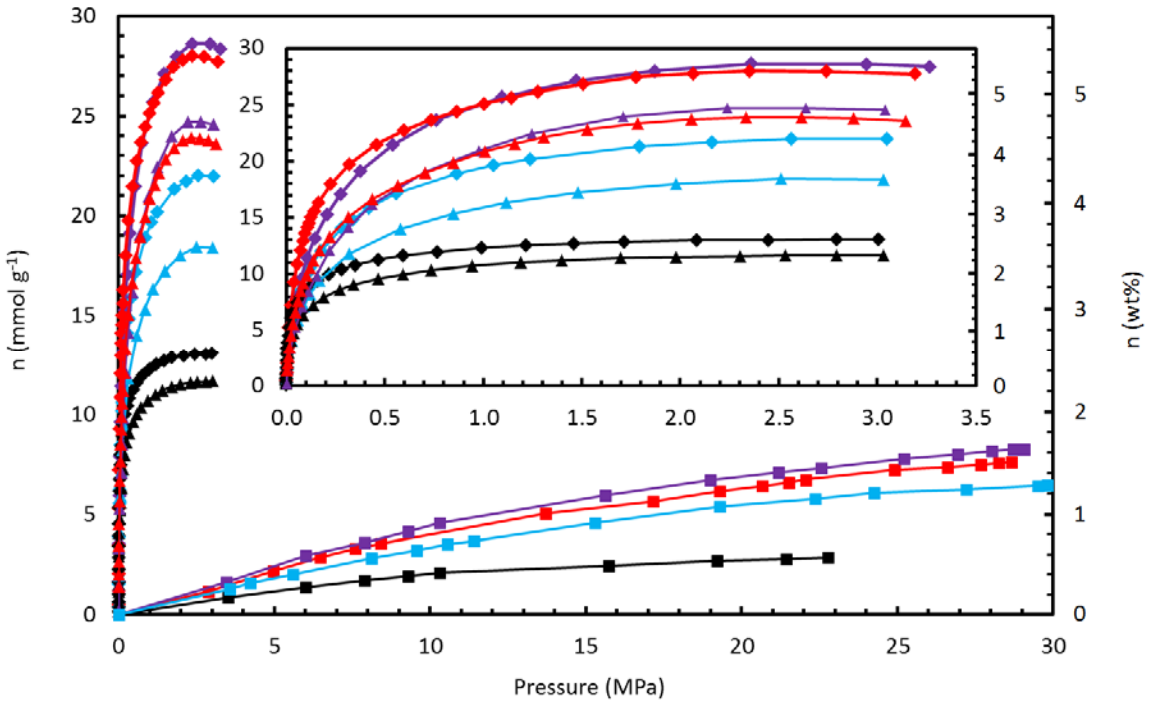

Figure 4.13. Equilibrium adsorption isotherms of hydrogen on MSC-30 (red), ZTC-2 (blue), ZTC-3 (purple), and CNS-201 (black) at 77 K (diamond), 87 K (triangle), and 298 K (square) between 0-30 MPa (inset shows detail between 0-3.5 MPa).

4.4.3 Hydrogen Adsorption Results

The complete set of equilibrium adsorption isotherms of hydrogen on CNS-201, MSC-30, ZTC-2, and ZTC-3 is shown in Figure 4.13. Hydrogen adsorption at all temperatures and pressures was fully reversible in all materials studied after numerous cycles. The Gibbs surface excess maximum hydrogen capacities of the materials are summarized in Table 4.1. The highest measured was for ZTC-3: 28.6 mmol g^{-1} (5.5 wt%) at 2.4 MPa. Maximum uptake was higher in ZTC-3 than MSC-30 despite a more gradual initial increase at low pressure.

Equilibrium adsorption isotherms of H_2 on ZTCs, MSC-30, and CNS-201 were measured up to 30 MPa at room temperature, and are shown in Figure 4.14 (the same

data as in Figure 4.13, isolated for clarity). Excess hydrogen capacities of the materials were calculated by extrapolation of the data to 30 MPa and are summarized in Table 4.1. The highest measured was for ZTC-3: 8.3 mmol g^{-1} (1.6 wt%) at 30 MPa and 298 K.

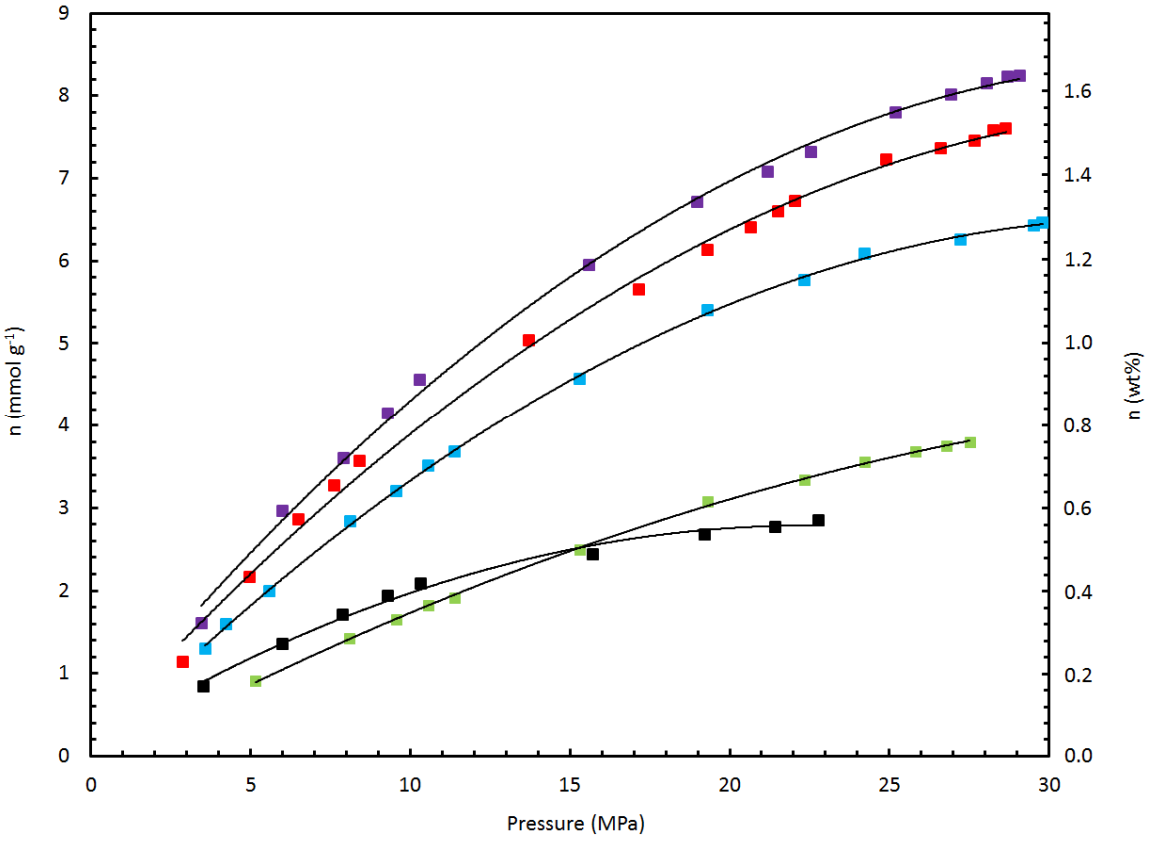

Figure 4.14. Equilibrium adsorption isotherms of H_2 on MSC-30 (red), ZTC-1 (green), ZTC-2 (blue), ZTC-3 (purple), and CNS-201 (black) at 298 K between 0-30 MPa.

Verification of the calibration of our high-pressure volumetric apparatus was by measurements of commercial materials MSC-30 and CNS-201. However, comparison of standard materials to references was found to be reliable only in some instances. The superactivated carbon MSC-30, a material processed similarly to Anderson AX-21, is reported to have a BET surface area ranging from 2600-3400 m^2 g^{-1}.[2, 7, 21-23] This variation is not only due to differences in the analysis of the N_2 adsorption isotherms at

77 K, but is also reflected in differences in hydrogen adsorption isotherms at temperatures from 77-298 K, implying that different batches of MSC-30 have different properties. Hydrogen capacities of MSC-30 at 298 K range from 3-4 mmol g^{-1} (0.6-0.8 wt%) at 10 MPa; in this report, it was measured to be 3.9 mmol g^{-1} which is consistent with the upper end of this range. Hydrogen uptake in CNS-201 was 2.0 mmol g^{-1}, compared to a reference value of 2.1 mmol g^{-1}.[21]

4.4.4 Enthalpy of Adsorption

The equilibrium excess hydrogen adsorption data for ZTC-3, MSC-30, and CNS-201 were fitted in two ways: using a typical "isoexcess" model-independent virial-type fitting equation (to 3rd order terms), and using a generalized double-Langmuir fitting equation which allows the determination of the absolute adsorption quantity. The enthalpy of adsorption was calculated by the isoexcess and isosteric method, respectively (see Sections 2.4-5).

Plots of the isoexcess enthalpy of adsorption of hydrogen on CNS-201, MSC-30, ZTC-2 and ZTC-3 are shown in Figure 4.15. The isosteric enthalpy of adsorption calculated using the real gas density of hydrogen on CNS-201, MSC-30, and ZTC-3 is shown in Figure 4.16. In both cases, the calculations were performed by fitting the data from the entire range of temperature between 77-298 K. For the isoexcess method, only an average enthalpy was accessible while the isosteric enthalpy could be calculated at arbitrary temperatures within the temperature range measured. The average Henry's law values, $-\Delta H_0$, for the materials studied are summarized in Table 4.1.

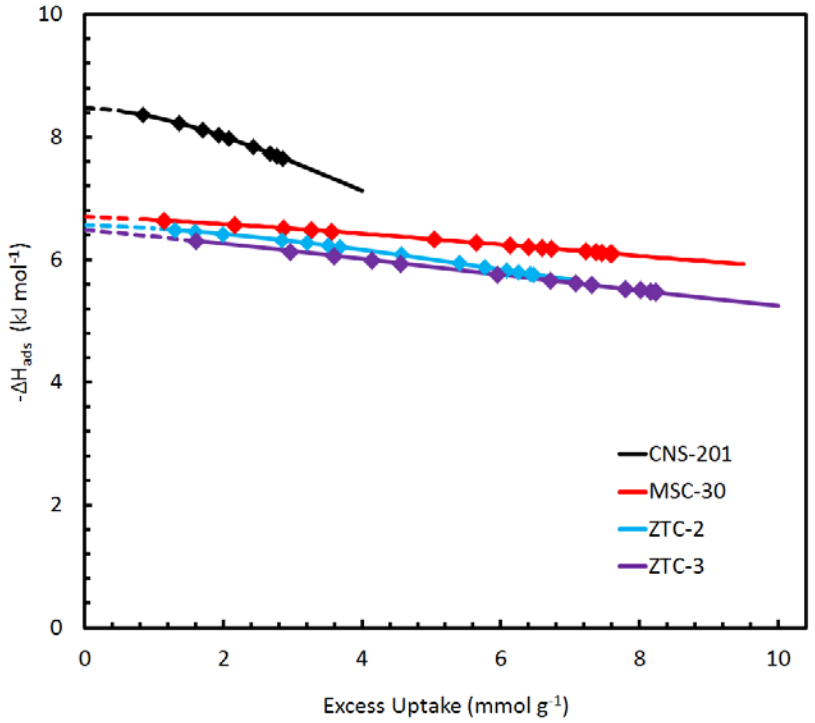

Figure 4.15. Average isoexcess enthalpy of adsorption of hydrogen on CNS-201 (black), MSC-30 (red), and ZTC-3 (purple) as a function of excess uptake between 77-298 K.

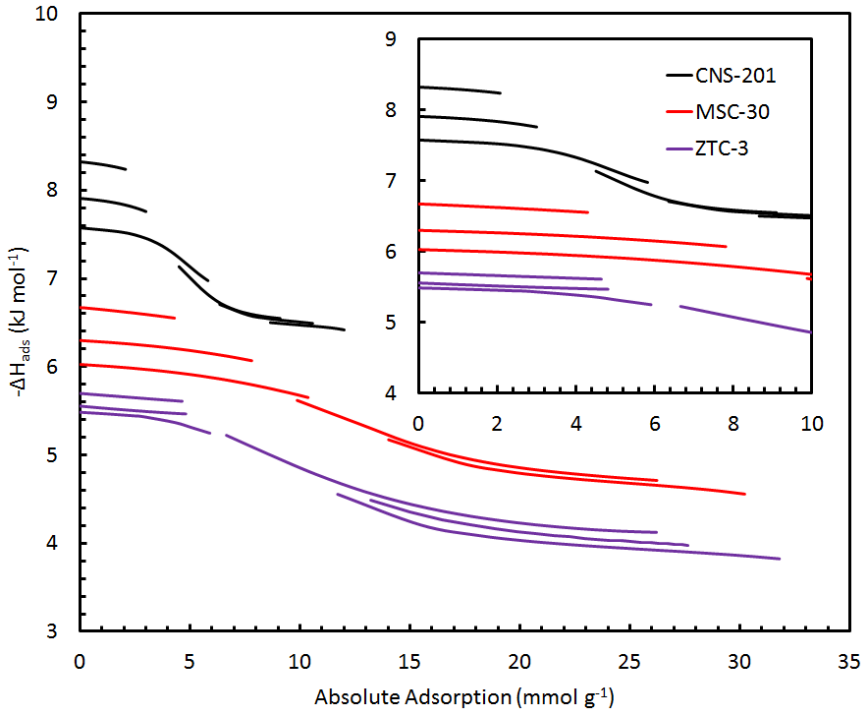

Figure 4.16. Isosteric enthalpy of adsorption of hydrogen on CNS-201 (black), MSC-30 (red), and ZTC-3 (purple) as a function of absolute uptake, at temperatures from 77-298 K.

Similar results are found using both methods due to the near-ideal properties of hydrogen in the temperature and pressure range measured. The highest value reported is for CNS-201 which is known to have an exceptionally high binding energy for hydrogen.[24] It decreases substantially as uptake increases, which is also reflected in the shape of the hydrogen uptake curves for CNS-201 at all temperatures. The adsorption enthalpy calculated for ZTCs and MSC-30 decreases only slightly and is relatively constant as uptake increases; the continued increase in uptake at 30 MPa compared to CNS-201 can be attributed to this characteristic of the higher surface area materials.

4.5 Discussion

The addition of sorbent material to a storage tank has two consequences: the volume available for gaseous storage is decreased (by the material's skeletal density) and the surface available for van der Waals interactions is increased (by the material's specific surface area). With enthalpy of adsorption in the range of 4-9 kJ mol^{-1}, as is observed for carbon materials, careful measurements of sample density and surface area are critical for characterizing sorption capacity and can be used together to readily predict material performance in the temperature and pressure conditions studied: 77-298 K and 0-30 MPa.

4.5.1 Skeletal Density

Skeletal density is the only material specific variable required, and therefore the most important variable in accurate determination of excess hydrogen uptake in adsorption measurements. Carbonaceous materials often have a similar skeletal density

to graphite, 2.1-2.2 g mL^{-1}.[21] However, skeletal densities in ZTCs are significantly lower, 1.8 g mL^{-1}. This indicates a less graphitic nature of ZTCs, but is not easily explained since ZTCs are predominantly sp^2 carbon.[17, 18] Distortions such as bond stretching or vacancy defects which could alter the ratio of sp^2 to sp^3 bonding of carbon atoms would have to be large to account for this difference. However, the fractions of sp^2 and sp^3 bonding were found to be similar through auxiliary measurements by x-ray photoelectron spectroscopy (XPS), electron energy-loss spectroscopy (EELS), and solid-state ^{13}C NMR.

One explanation of the significantly lower skeletal density of ZTCs can be given by recent results from elemental analysis experiments. Elemental composition (CHN) of MSC-30 and ZTC-3 was determined by triplicate combustion experiments, using the Dumas method.[25] Samples were prepared by degassing at 250°C and sealed in foil packets in an argon glovebox with < 1 ppm H_2O, a critical step for obtaining an accurate estimate of the H content since any adsorbed H_2O would contribute to detected H. Average hydrogen content in ZTC-3 was 2.4 wt% H, approximately twice that in MSC-30: 1.2 wt% H. If each atomic site where carbon is substituted for hydrogen retains its original skeletal volume, the difference in skeletal density would be 11%, a decrease from 2.1 to 1.9 g mL^{-1}. Additional decrease in skeletal density could be due to the presence of hanging C-H groups which have a larger atomic volume than a pair of sp^2 hybridized carbon atoms. This approximation gives a representative figure for the significance of increased H content to the skeletal density, an effect that is large enough to account for the difference between MSC-30 and ZTC-3.

4.5.2 Surface Area

Hydrogen uptake at 77 K and 298 K is generally proportional to surface area in the materials studied, as shown in Figure 4.17. The relationship for ZTCs at 77 K is ~9 mmol g^{-1} (1.8 wt%) Gibbs surface excess maximum hydrogen capacity per 1000 m^2 g^{-1} BET surface area, the same as for other carbonaceous materials.[3] This corresponds to 5.4 molecules of H_2 per nm^2 of BET surface area. The relationship for ZTCs at 30 MPa and 298 K is 2.3 mmol g^{-1} (0.46 wt%) excess hydrogen uptake per 1000 m^2 g^{-1} BET surface area, the same as for other carbonaceous materials in this study. Importantly, this result is contrary to a previous result[7] which reports higher uptake in ZTCs at 303 K: 2.8 mmol g^{-1} (0.55 wt%) excess hydrogen uptake per 1000 m^2 g^{-1} BET surface area in "P7(2)-H," compared to 2.0 mmol g^{-1} (0.41 wt%) per 1000 m^2 g^{-1} in MSC-30. In this previous report, a 100% increase in uptake was measured for ZTCs compared to MSC-30, and it could not be explained by surface area. Compared to the results in this study, the measurement of uptake in ZTC "P7(2)-H" was erroneously high, while uptake in MSC-30 was underestimated, contributing to a large apparent enhancement in hydrogen capacity of ZTC compared to MSC-30.

While ZTCs measured in the present study show increased uptake compared to MSC-30, this was consistent with their larger specific surface area. These relationships are critically dependent on the accurate and consistent determination of specific surface area of the sorbent material and the assumptions inherent to BET theory. The known shortcomings of this method for microporous materials are thought to be approximately equal in the materials studied. However, extreme care must still be taken in analysis of

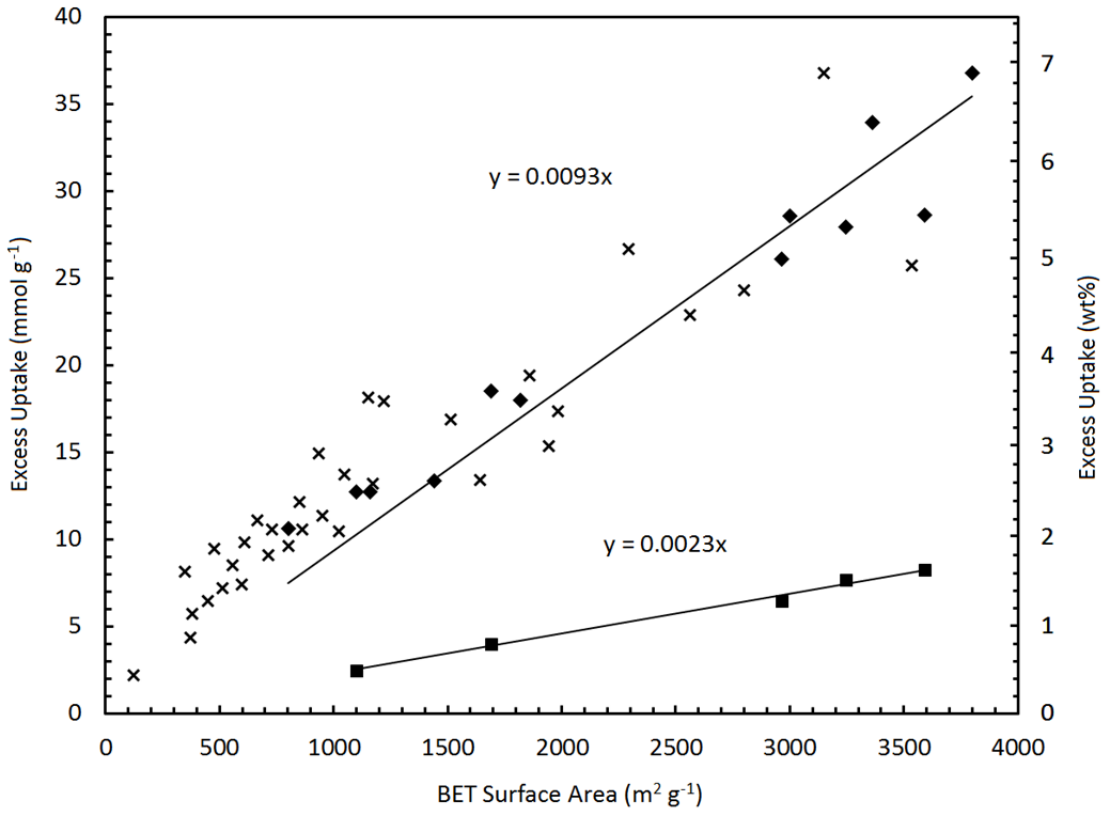

Figure 4.17. Equilibrium excess adsorption uptake of hydrogen as a function of BET surface area at 77 K (Gibbs excess surface maximum capacity: diamond) and 298 K (at 30 MPa: square). An × indicates a reported value from the literature, at 77 K.

the nitrogen isotherms at 77 K; assumption of a standard pressure range over which to fit the BET equation is not appropriate. The region from low pressure up to the knee of the isotherm ("point B" for a type II isotherm) must be included as this pressure range is different for each material. For MSC-30, the calculation is especially sensitive to the range chosen because the knee is rounded and there are two nearly linear regions in the isotherm (type IV like character). Even for classic type II isotherms, BET surface area is often miscalculated: in "CB850h," a ZTC which was reported to have a maximum excess hydrogen capacity of 8.33 wt% at 77K, the BET surface area is calculated to be 3150 m^2 g^{-1}.[26] This value would represent an extreme outlier on a plot of hydrogen capacity at

77K as a function of surface area; however, our analysis of the reported N_2 isotherm data gives a BET surface area of 3800 $m^2 g^{-1}$, much closer to the expected value for such a high capacity sorbent. Similarly, "P7(2)-H" was reported to have a BET surface area of 3800 (while our analysis yields a value of 3538 ± 50) $m^2 g^{-1}$.[7] Another method of ranking similar sorbents of the same material class is by comparing the nitrogen uptake capacity at 77 K and an intermediate pressure, say P/P_0 = 0.5. This analysis also shows "CB850h" to be among the highest performance sorbent materials and explains the large excess hydrogen capacity at 77 K. ZTC-3 was found to be nearly identical to "P7(2)-H" in this comparison and explains the similar surface area when a consistent calculation method is used.

4.5.3 Enthalpy of Adsorption

The similarity of isoexcess enthalpies of adsorption between ZTCs and MSC-30 in Figures 4.15 and 4.16 implies that there are no significant differences in the dispersion forces responsible for hydrogen physisorption. The high-pressure data at 298 K allows the unique contribution of high temperature data to the calculation of isoexcess enthalpy of adsorption. However, dispersion forces are known to have a significant temperature dependence.[27, 28] For instance, the heat of adsorption of hydrogen on MOF-5 is reported to increase by up to 1 kJ mol^{-1} between cryogenic and room temperatures.[27] Therefore, the values given in Table 4.1 are to be understood as averages over the whole temperature range for the given material. Indeed, when a more sophisticated method was used to determine isosteric enthalpy of adsorption, the double-Langmuir fitted results shown in Figure 4.16, a similar temperature dependence

of the enthalpy was calculated between all materials: 2-4 J mol^{-1} K^{-1}. It is important to note that this analysis method works best on data sets with numerous isotherms in a close temperature range, preferably spaced by 10-20 K. The three temperatures collected in this study were much further apart, and the fits were difficult to optimize; the data plotted in a narrow range for each temperature (as in Figure 4.16) was the best representation of the dependence of enthalpy with uptake.

The hydrogen uptake character in ZTCs at 77 K, especially ZTC-3, is slightly different from MSC-30 because the uptake is lower between 0-1.0 MPa, but exceeds MSC-30 between 1.0-2.4 MPa. For effective hydrogen delivery by a sorbent material between two finite pressures, P_f - P_i, it is favorable to have an excess uptake slope that is gradual below P_f and steep in the cycled region of uptake/delivery; the quantity of hydrogen delivered is the difference between the amount in the initial (fully charged) state at P_i and the final (considered "empty") state at P_f. For delivery to a fuel cell, P_f is often taken to be 0.3 MPa.[29] Therefore, ZTCs used for this purpose at 77 K exhibit higher hydrogen delivery than MSC-30 by 15% when cycled between 0.3-2.4 MPa.

4.6 Conclusions

Equilibrium hydrogen uptake capacities of ZTCs at room temperature are among the highest of known physisorbent materials due to their large specific surface area. Hydrogen adsorption capacity in ZTCs is approximately proportional to surface area at 298 K between 0-30 MPa, and is consistent with a large variety of carbonaceous materials, including activated carbons, carbon fibers, graphite, aerogels, and nanotubes.

That is, a “Chahine’s rule” type of trend is observed at room temperature and fixed pressure for carbon-based materials, including ZTCs. This trend is found to be 2.3 mmol g^{-1} (0.46 wt%) excess hydrogen uptake per 1000 m^2 g^{-1} BET surface area at 298K and 30 MPa. ZTCs were found to have an isoexcess enthalpy of adsorption comparable to MSC-30 when measured between 77-298 K: 6.5 kJ mol^{-1} in the Henry’s law limit. This implies that there are no significant differences in the dispersion forces responsible for hydrogen physisorption in ZTCs compared to MSC-30. Unlike other carbons, ZTCs were measured to have significantly lower skeletal density; this has the effect of increasing calculated uptake and straightening the uptake curve with increasing pressure. This is beneficial for gravimetric hydrogen delivery by ZTCs during cycling between two finite pressures in an engineering application, especially at 77 K.

4.7 References

(1) J. Purewal, J. Keith, C. Ahn, B. Fultz, C. Brown, and M. Tyagi, 'Adsorption and melting of hydrogen in potassium-intercalated graphite', *Phys. Rev. B,* **79** (2009).

(2) E. Poirier, R. Chahine, and T. K. Bose, 'Hydrogen adsorption in carbon nanostructures', *Int. J. Hydrogen Energ.,* **26**, 831-835 (2001).

(3) B. Panella, M. Hirscher, and S. Roth, 'Hydrogen adsorption in different carbon nanostructures', *Carbon,* **43**, 2209-2214 (2005).

(4) R. Ströbel, J. Garche, P. T. Moseley, L. Jörissen, and G. Wolf, 'Hydrogen storage by carbon materials', *J. Power Sources,* **159**, 781-801 (2006).

(5) T. Kyotani, 'Control of pore structure in carbon', *Carbon,* **38**, 269-286 (2000).

(6) T. Kyotani, T. Nagai, S. Inoue, and A. Tomita, 'Formation of new type of porous carbon by carbonization in zeolite nanochannels', *Chem. Mater.,* **9**, 609-615 (1997).

(7) H. Nishihara, P. X. Hou, L. X. Li, M. Ito, M. Uchiyama, T. Kaburagi, A. Ikura, J. Katamura, T. Kawarada, K. Mizuuchi, and T. Kyotani, 'High-pressure hydrogen storage in zeolite-templated carbon', *J. Phys. Chem. C,* **113**, 3189-3196 (2009).

(8) M. A. de la Casa-Lillo, F. Lamari-Darkrim, D. Cazorla-Amorós, and A. Linares-Solano, 'Hydrogen storage in activated carbons and activated carbon fibers', *J. Phys. Chem. B,* **106**, 10930-10934 (2002).

(9) B. Liu, H. Shioyama, T. Akita, and Q. Xu, 'Metal-organic framework as a template for porous carbon synthesis', *J. Am. Chem. Soc.,* **130**, 5390-5391 (2008).

(10) B. Liu, H. Shioyama, H. Jiang, X. Zhang, and Q. Xu, 'Metal-organic framework (MOF) as a template for syntheses of nanoporous carbons as electrode materials for supercapacitors', *Carbon,* **48**, 456-463 (2010).

(11) H.-L. Jiang, B. Liu, Y. Q. Lan, K. Kuratani, T. Akita, H. Shioyama, F. Zong, and Q. Xu, 'From metal-organic framework to nanoporous carbon: toward a very high surface area and hydrogen uptake', *J. Am. Chem. Soc.,* **133**, 11854-11857 (2011).

(12) H. Nishihara and T. Kyotani, 'Templated nanocarbons for energy storage', *Adv. Mater.,* **24**, 4473-4498 (2012).

(13) S. J. Gregg and K. S. W. Sing, *Adsorption, surface area, and porosity*, Academic Press, London (1982).

(14) P. Tarazona, U. M. B. Marconi, and R. Evans, 'Phase equilibria of fluid interfaces and confined fluids', *Mol. Phys.,* **60**, 573-595 (1987).

(15) N. P. Stadie, J. J. Vajo, R. W. Cumberland, A. A. Wilson, C. C. Ahn, and B. Fultz, 'Zeolite-templated carbon materials for high-pressure hydrogen storage', *Langmuir,* **28**, 10057-10063 (2012).

(16) J. I. Langford and A. J. C. Wilson, 'Scherrer after sixty years: a survey and some new results in the determination of crystallite size', *J. Appl. Crystallogr.,* **11**, 102-113 (1978).

(17) Y. Yang, C. M. Brown, C. Zhao, A. L. Chaffee, B. Nick, D. Zhao, P. A. Webley, J. Schalch, J. M. Simmons, Y. Liu, J.-H. Her, C. E. Buckley, and D. A. Sheppard, 'Micro-channel development and hydrogen adsorption properties in templated microporous carbons containing platinum nanoparticles', *Carbon,* **49**, 1305-1317 (2011).

(18) Z. Ma, T. Kyotani, and A. Tomita, 'Synthesis methods for preparing microporous carbons with a structural regularity of zeolite Y', *Carbon,* **40**, 2367-2374 (2002).

(19) Z. Ma, T. Kyotani, Z. Liu, O. Terasaki, and A. Tomita, 'Very high surface area microporous carbon with a three-dimensional nano-array structure: synthesis and its molecular structure', *Chem. Mater.,* **13**, 4413-4415 (2001).

(20) L. Schlapbach, 'Hydrogen as a fuel and its storage for mobility and transport', *MRS Bull.,* **27**, 675-679 (2002).

(21) M.-A. Richard, D. Cossement, P.-A. Chandonia, R. Chahine, D. Mori, and K. Hirose, 'Preliminary evaluation of the performance of an adsorption-based hydrogen storage system', *AlChE J.,* **55**, 2985-2996 (2009).

(22) Y. Li and R. T. Yang, 'Hydrogen storage on platinum nanoparticles doped on superactivated carbon', *J. Phys. Chem. C,* **111**, 11086-11094 (2007).

(23) N. P. Stadie, J. J. Purewal, C. C. Ahn, and B. Fultz, 'Measurements of hydrogen spillover in platinum doped superactivated carbon', *Langmuir,* **26**, 15481-15485 (2010).

(24) J. J. Purewal, H. Kabbour, J. J. Vajo, C. C. Ahn, and B. Fultz, 'Pore size distribution and supercritical hydrogen adsorption in activated carbon fibers', *Nanotechnology,* **20**, 204012 (2009).

(25) J. B. Dumas, 'A method of estimating nitrogen in organic material', *Ann. Chim. et Phys.,* **58**, 171 (1833).

(26) Z. Yang, Y. Xia, and R. Mokaya, 'Enhanced hydrogen storage capacity of high surface area zeolite-like carbon materials', *J. Am. Chem. Soc.,* **129**, 1673-1679 (2007).

(27) F. O. Mertens, 'Determination of absolute adsorption in highly ordered porous media', *Surf. Sci.,* **603**, 1979-1984 (2009).

(28) J. M. Obrecht, R. J. Wild, M. Antezza, L. P. Pitaevskii, S. Stringari, and E. A. Cornell, 'Measurement of the temperature dependence of the Casimir-Polder force', *Phys. Rev. Lett.,* **98**, 063201 (2007).

(29) J. Purewal, D. Liu, A. Sudik, M. Veenstra, J. Yang, S. Maurer, U. Müller, and D. J. Siegel, 'Improved hydrogen storage and thermal conductivity in high-density MOF-5 composites', *J. Phys. Chem. C,* **116**, 20199-20212 (2012).

Chapter 5

Zeolite-Templated Carbon: Anomalous Methane Adsorption

5.1 Introduction

5.1.1 Background

For effective energy storage by physical adsorption, a high total capacity (corresponding to a large number of binding sites) is necessary for high potential delivery. Additionally, the characteristic binding energies of the sorbent-adsorbate interactions are crucial to the practical deliverable capacity because the storage tank must be cycled between two finite pressures, and the amount stored in the system at the lower bound (e.g., 0.3 MPa) should ideally be low. The optimal material for physisorptive energy storage can been assumed to have a high binding energy that is constant with increased loading. For hydrogen, the average enthalpy of adsorption across a wide variety of carbon materials (activated carbon, nanofibers, aerogels, templated-carbons, etc.) is 4-6 kJ (mol H_2)$^{-1}$,[1, 2] which is not significantly higher than the average thermal energy at 298 K and limits their effective use to cryogenic temperatures. Physical adsorption of methane is much stronger, typically 12-20 kJ mol^{-1},[1, 2] and near-ambient temperature applications for methane storage are promising.

In microporous carbonaceous materials, the pore structure and surface chemistry are the characteristics that offer the potential to adjust the thermodynamic properties of adsorption. Boron- and nitrogen-doped materials have shown promise in exhibiting higher enthalpies of adsorption.[3-5] However, as in pure carbon-based materials, the enthalpy declines rapidly with loading. A more effective approach for tuning the thermodynamics of adsorption is by controlling the pore-size distribution and mean pore width to achieve optimal binding interactions. Theoretical models of adsorption in graphitic slit pores show that pore-widths corresponding to three molecular diameters of the adsorptive gas are ideal for maximizing adsorbate-adsorbate interactions and increasing the total energy of adsorption.[6-8] However, adsorption measurements on engineered graphene-scaffolds[9] and other microporous materials[10, 11] have never shown an appreciably increasing binding energy in the high surface coverage regime.

Template carbonization is an effective technique for producing carbonaceous materials with exceptionally large specific surface area and controlled porosity.[12, 13] Zeolite-templated carbons (ZTCs) are microporous, amorphous carbon materials with extremely high surface area and a periodic array of pores complementary to the structure of the zeolite used in the template-carbonization synthesis, and are extensively described in Chapter 4. We synthesized numerous ZTCs with varying properties, and here we present a study of their thermodynamic properties during methane adsorption, a secondary application that is well suited to this particular class of materials. A key property of faujasite-templated ZTCs, such as ZTC-3, is the sharp pore-size distribution centered at 1.2 nm, markedly differing from other microporous carbons

which typically have a wide distribution of pore-widths. While the nature of the microstructure of carbonaceous materials has not been previously reported to have a significant effect on their adsorptive capacities for methane,[14] pore widths in ZTCs approach the optimal value suggested by theoretical studies to be 1.14 nm.[6, 7] Recent calculations of methane adsorption on metal-organic framework CPO-27-Mg, a crystalline material with well-characterized adsorption sites within small (~1.1 nm) cages, show that strong adsorbate-adsorbate interactions play an important role in the enthalpy of methane adsorption, resulting in a 15% increase in excess capacity at near 298 K.[15] By performing detailed adsorption measurements of methane adsorption in ZTC-3 at 13 temperatures between 238-526 K, we find that in fact the precise conditions for enhanced enthalpy of adsorption from lateral interactions have been achieved, an effect that had been elusive to experimental groups up until the time of this study. The implications are significant since ZTCs have both extremely high surface area and well-adapted porosity for methane adsorption, giving them a strong advantage over typical carbons in deliverable methane capacity at high pressure.

5.1.2 Materials

Zeolite-templated carbon, ZTC-3, was synthesized by the impregnation of zeolite NaY with poly-furfuryl alcohol, undergoing a propylene CVD step at 700°C, and carbonization was performed at 900°C. The template was removed by dissolution in HF. Details of the synthesis, and the important steps for attaining high template fidelity, are found in Section 4.2, following the standard procedure.[16] For comparison, two other commercial activated carbons were also investigated: CNS-201, a modest surface area

carbon with extremely narrow micropores, and MSC-30, a superactivated carbon with extremely high surface area that is often measured as a standard. These materials were degassed at 250°C under vacuum to < 0.1 mPa before use. The surface and pore characteristics of the materials used in this study are given in Table 5.1.

Table 5.1: Material properties of activated carbons CNS-201 and MSC-30, and zeolite-templated carbon ZTC-3.

Material	Skeletal Density[◊] ($g\ mL^{-1}$)	Bulk Density[◊◊] ($g\ mL^{-1}$)	BET Surface Area ($m^2 g^{-1}$)	DR Micropore Volume ($mL\ g^{-1}$)	247 K CH_4 Capacity[†] ($mmol\ g^{-1}$)	298 K CH_4 Capacity[††] ($mmol\ g^{-1}$)	~523 K CH_4 Capacity[†††] ($mmol\ g^{-1}$)
CNS-201	2.1	0.50	1095 ± 8	0.45	7.45	5.98	2.48
MSC-30	2.1	0.27	3244 ± 28	1.54	20.2	14.5	5.16
ZTC-3	1.8	0.18	3591 ± 60	1.66	20.5	14.1	4.76

[◊] Skeletal density measured using He at 298 K between 0-3 MPa. [◊◊] Bulk density measured on maximum packing. [†] Measured at 247 K and Gibbs excess maximum pressure. [††] Measured at 298 K and Gibbs excess maximum pressure. [†††] Measured at 526, 521, and 518 K for CNS-201, MSC-30, and ZTC-3, respectively, at 10 MPa.

The pore-size distribution in CNS-201, obtained by the non-localized density functional theory (NLDFT) method, contains 3 peaks, at 0.54 nm, 0.80 nm, and 1.18 nm, with 50%, 20%, and 15% of the pore volume in each, respectively (see Figure 5.1). MSC-30 contains a broad distribution of pore-widths between 0.6-3.5 nm and 40% of the pore volume is contained in pores > 2.1 nm in width. The distribution of pores in ZTC-3 is

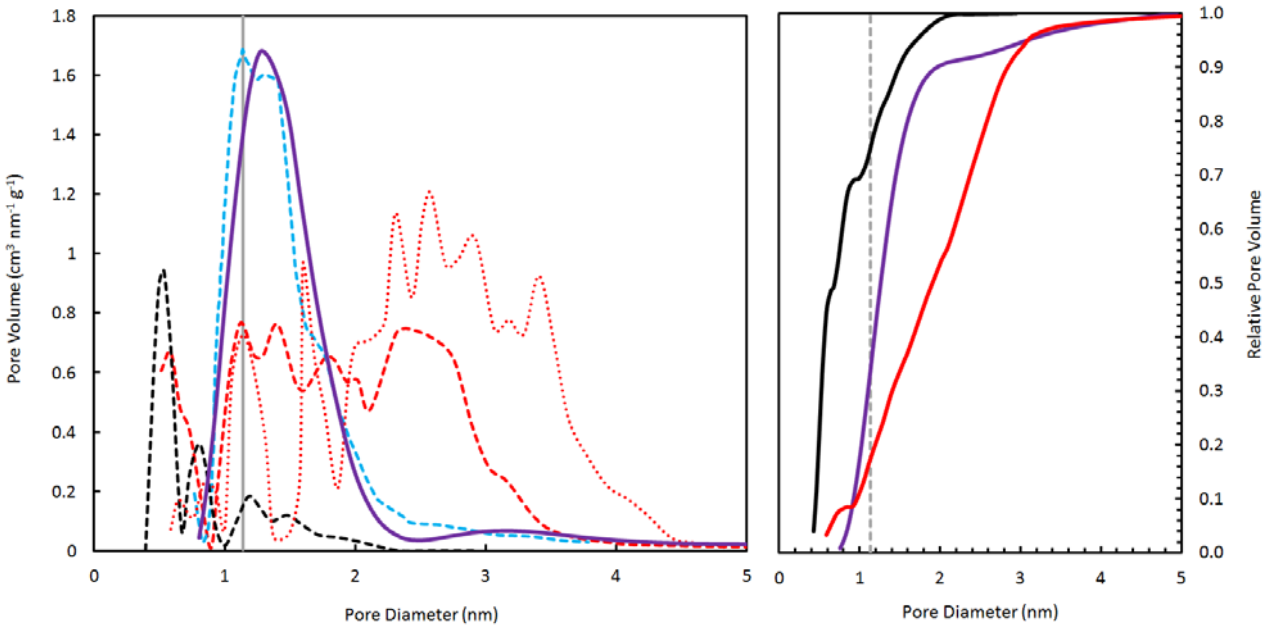

Figure 5.1. The pore-size distribution (left) and relative filling (right) of CNS-201 (black), MSC-30 (red), ZTC "P7(2)-H" (blue), and ZTC-3 (purple), calculated by the NLDFT method.

characterized by a single sharp peak centered at 1.2 nm, with > 90% of the pore volume having a pore width between 0.85-2.0 nm. This regularity of pore-size in ZTC-3 was confirmed by x-ray diffraction (XRD), which shows a sharp peak centered at 2θ = 6° (see Figure 4.4), and transmission electron microscopy (TEM) which shows a periodic spacing of diffraction contrast corresponding to pores of width 1 nm (see Figure 4.8). Skeletal densities of the samples were measured by helium pycnometry; the activated carbons have 2.1 g mL^{-1}, consistent with a wide variety of carbonaceous materials[17], while ZTC-3 has a lower skeletal density (1.8 g mL^{-1}, consistent with other ZTCs[16]) presumably due to increased hydrogen terminations (a detailed discussion can be found in Section 4.5.1).

5.2 Methane Adsorption

5.2.1 High-Pressure Experiments

Methane adsorption isotherms at all temperatures were measured with a volumetric Sieverts apparatus, commissioned and verified for accurate measurements up to 10 MPa.[18-20] The sample was submerged in a chiller bath for sub-ambient temperature isotherms. For high temperatures, the sample was placed inside a cylindrical copper heat exchanger and wrapped with insulated fiberglass heating tape. A PID controller and K-type thermocouples were used to maintain a consistent temperature throughout measurement; fluctuations were less than ±0.1 K at low temperature and no higher than ±0.4 K at high temperatures. The system was leak tested up to 10 MPa and showed a maximum leak rate of 7.0×10^{-6} mol h^{-1} of CH_4. In Equation 3.1, this corresponds to a maximum leak of $k \sim 10^{-8}$ s^{-1} which is negligible for short time measurement.[21] The total inner volume of the apparatus was 66 mL.

Prior to methane adsorption measurements, 0.3-1.5 g of sample was loaded and degassed at 250°C under vacuum to < 0.1 mPa for 12 h. Two adsorption runs using research-grade methane (99.999%) were performed at each temperature and the data were combined for thermodynamic analysis. Multiple adsorption/desorption cycles were also performed at various temperatures to assure full reversibility of methane physisorption in the complete temperature and pressure regime of study and to test the precision of the experiments. Error between cycles was < 1% of the measured value. For example, three independent (non-consecutive) hydrogen adsorption/desorption cycles in ZTC-3 at 298 K are shown in Figure 5.2. The sample was degassed once before cycling

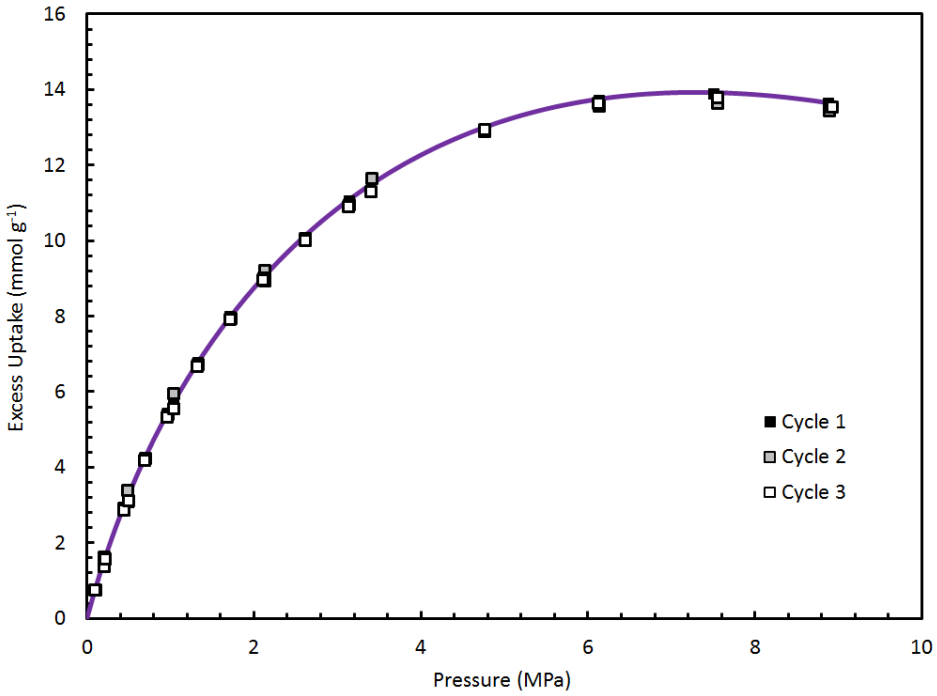

Figure 5.2. Equilibrium excess adsorption/desorption isotherms of methane on ZTC-3 at 298 K. Three cycles are shown, including adsorption and desorption points, displaying complete reversibility of uptake in these materials and showing typical precision between independent measurements.

but was not further treated between cycles. Equilibrium adsorption isotherms at 238, 298, and ~523 K are shown in Figure 5.3 for a direct comparison between the materials.

The complete set of methane adsorption isotherms on CNS-201, MSC-30, and ZTC-3 are shown in Figures 5.4-6. The excess maximum is similar for ZTC-3 and MSC-30 at room temperature, but slightly higher for MSC-30: 14.5 mmol g^{-1} at 8 MPa. While excess adsorption increases faster for MSC-30 at pressures between 0-0.8 MPa, uptake in ZTC-3 increases fastest between 0.8-5.7 MPa. Gravimetric uptake in CNS-201 is substantially less at all temperatures due to its low specific surface area. The highest measured excess uptake of this study is for ZTC-3 at 238 K: 22.1 mmol g^{-1} (26.2 wt%) at 4.7 MPa,

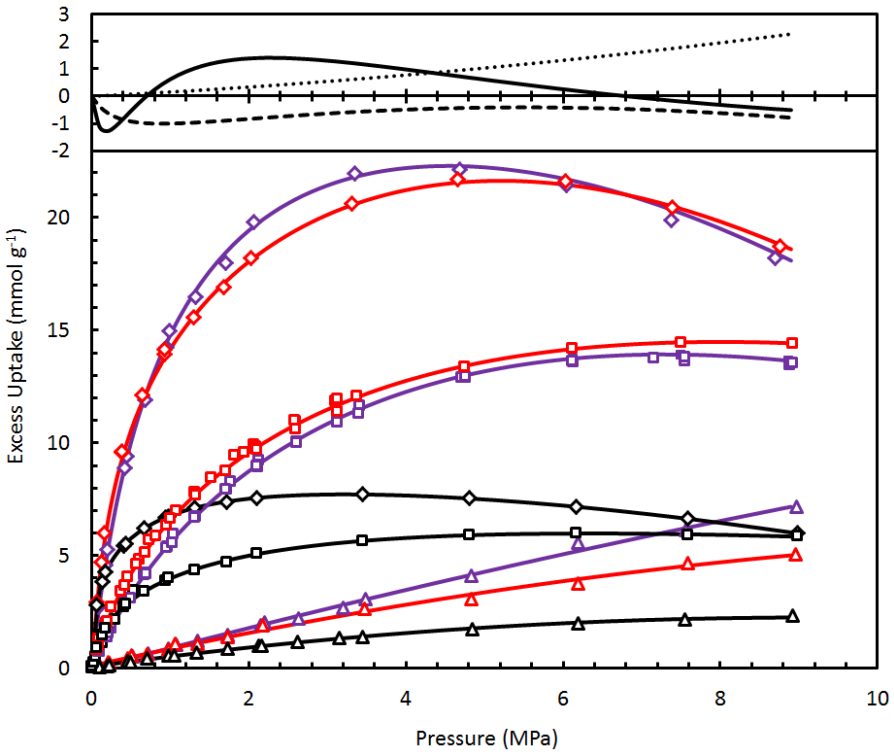

Figure 5.3. Comparison of equilibrium excess adsorption isotherms of methane on CNS-201 (black), MSC-30 (red), and ZTC-3 (purple) at 238 K (diamond), 298 K (square), and ~523 (triangle). The difference between ZTC-3 and MSC-30 is shown at the top: 238 K (full line), 298 K (dashed line), ~523 K (dotted line).

despite a gentler initial increase at low pressure. Interestingly, the excess uptake in ZTC-3 is also greater than MSC-30 at high temperatures although neither reaches a maximum between 0-9 MPa. These values correspond to a significant enhancement of deliverable methane capacity over pure compressed gas storage. At all temperatures, methane uptake in ZTC-3 is characterized by a gradual initial rise and delayed increase at pressures between 0.2-2 MPa, leading to higher eventual methane capacity than MSC-30, a material of comparable specific surface area.

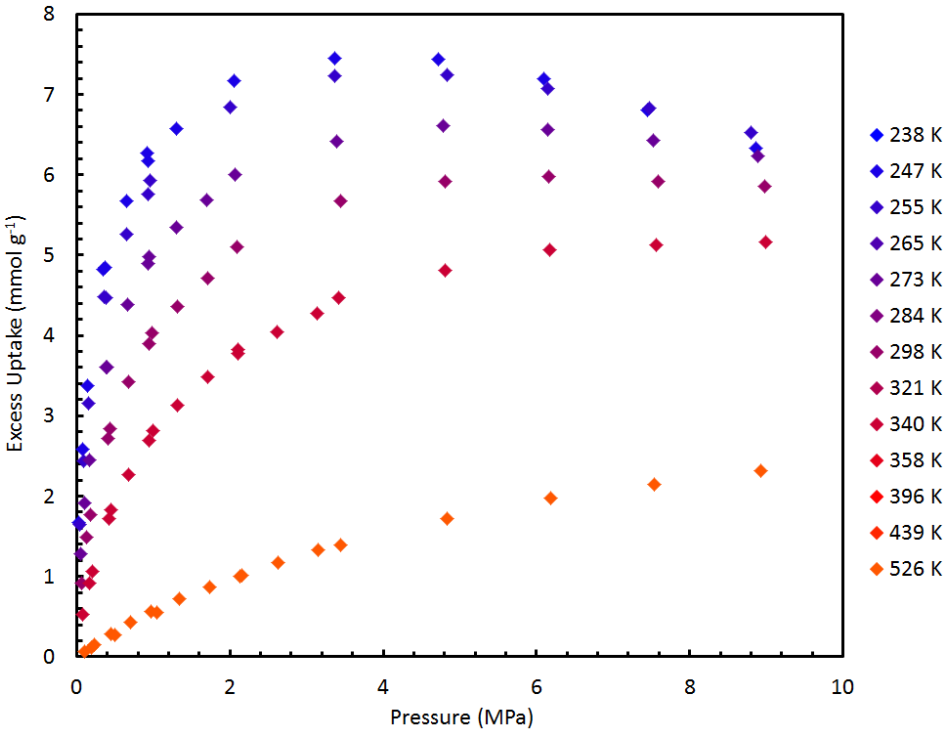

Figure 5.4. Equilibrium adsorption isotherms of methane on CNS-201 between 0-9 MPa.

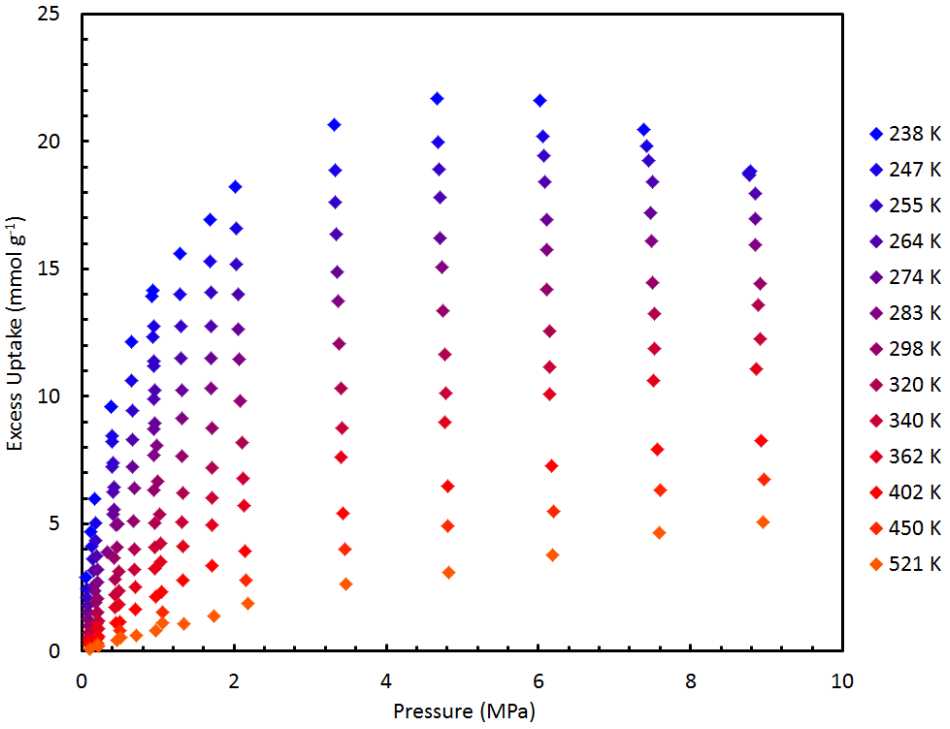

Figure 5.5. Equilibrium adsorption isotherms of methane on MSC-30 between 0-9 MPa.

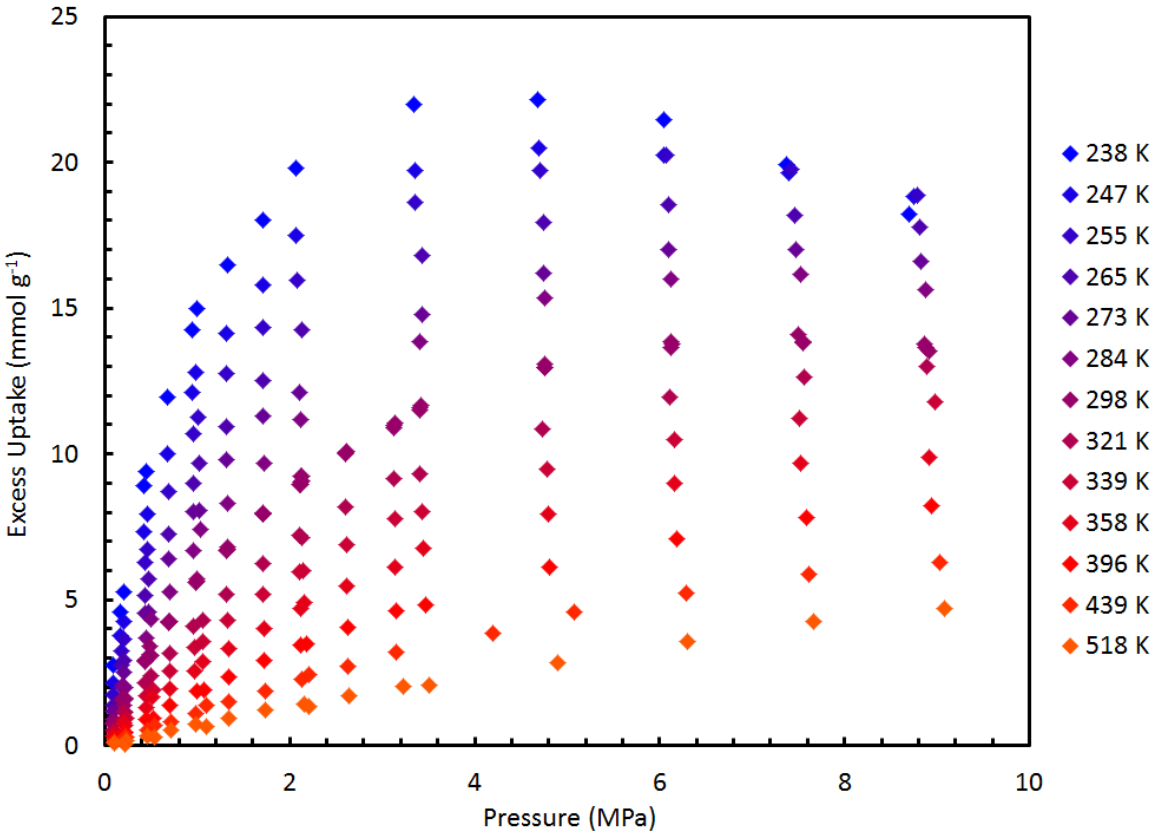

Figure 5.6. Equilibrium adsorption isotherms of methane on ZTC-3 between 0-9 MPa.

5.2.2 Fitting the Experimental Data

The experimental adsorption isotherms were fitted with the generalized-Langmuir equation, following the procedure detailed in Section 2.5. This is a general and very robust approach that allows the adsorption volume be an independent parameter of the fitting equation. The generalized-Langmuir fit was compared to other models, specifically the Unilan[22] and Langmuir-Freundlich type fitting equations, and better fits were given by the generalized-Langmuir equation. This can be considered a model-independent approach (as in Equation 2.47) or an approach to determine the absolute

quantity of adsorption (as in Equation 2.50). The minimum number of independent parameters is desired, and for the materials in this study, we find that i = 2 yields satisfying results. The optimized parameters are given in Table 5.2.

Least squares fits of the methane adsorption isotherms (on CNS-201, MSC-30, and ZTC-3) to the generalized-Langmuir equation are shown in Figure 5.7, the fitted excess adsorption (left) and calculated absolute adsorption (right) at all temperatures measured. The goodness of fit was satisfactory across the entire range of temperature and pressure for all three samples, with a residual sum of squares of <0.04 mmol g^{-1} per data point.

5.2.3 Trends

The maximum in excess adsorption measured in this study at 298 K scales linearly with the specific surface area of the materials studied, a relationship analogous to "Chahine's rule"[23] for the surface excess maximum of hydrogen at 77 K, consistent with the reported linear trend for methane uptake at 3.5 MPa and 298 K (see Figure 5.8).[14] The fit parameters can also be compared with the properties of the materials studied, shown in Figure 5.9. The scaling parameter n_{max} is proportional to the number of binding sites, found to be well approximated by the BET specific surface area. The maximum volume of the adsorbed layer, V_{max}, is also proportional to surface area for the activated carbons, although it is limited by the pore-width. The maximum volume of the adsorbed layer in ZTC-3 corresponds to half of the mean pore diameter that is characteristic of the material: a thickness of 0.6 nm.

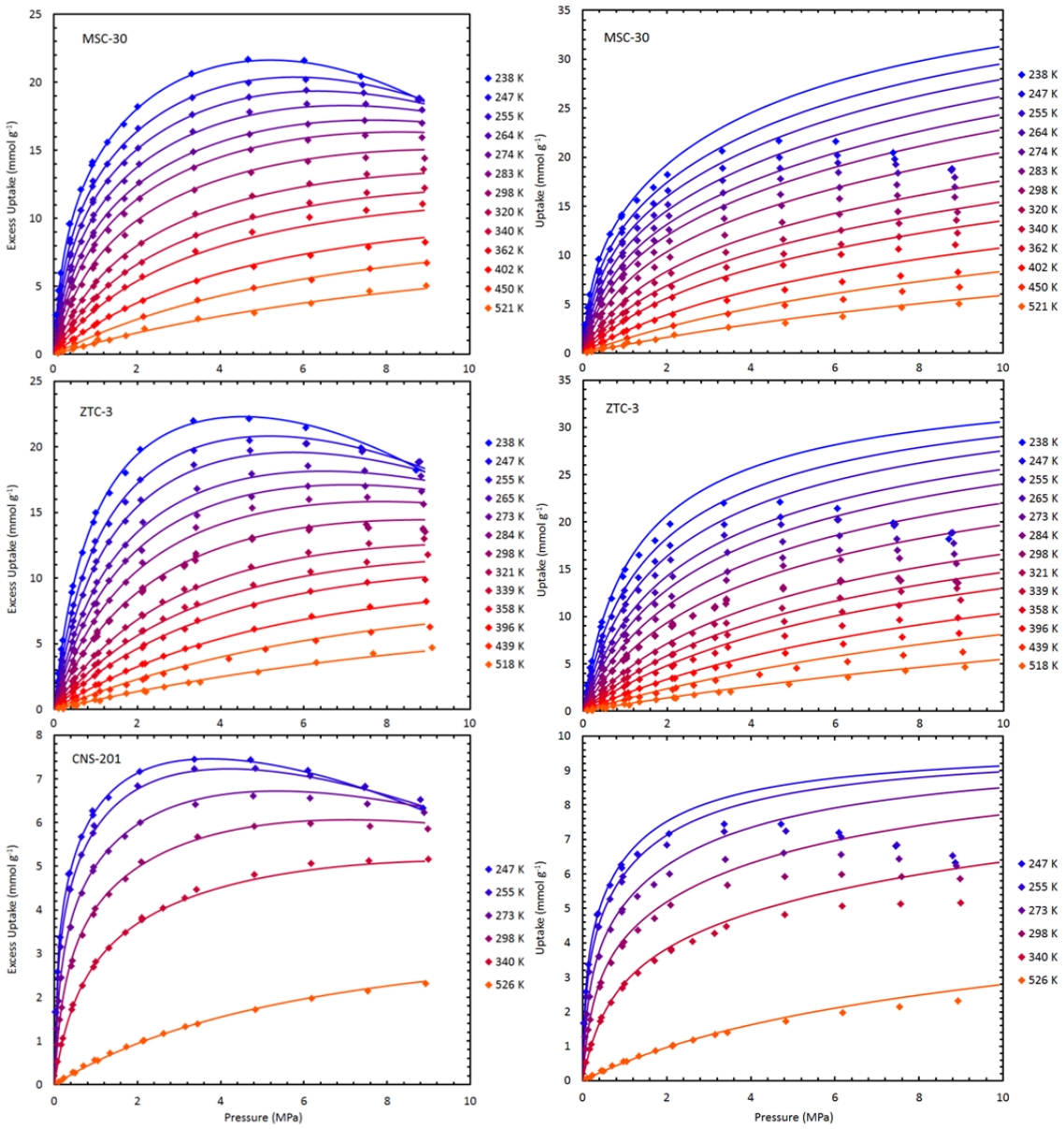

Figure 5.7. The fitted experimental data for MSC-30 (top), ZTC-3 (middle), and CNS-201 (bottom): excess uptake (left) and absolute uptake (right) at temperatures from 238-526 K (blue to orange). The diamonds are measured (excess) uptake.

Table 5.2: Least-squares minimized fit parameters of the generalized-Langmuir equation for methane adsorption on CNS-201, MSC-30, and ZTC-3 between 238-526 K.

Material	n_{max} (mmol g^{-1})	V_{max} (mL g^{-1})	α	A_1 ($K^{1/2}$ MPa^{-1})	E_1 (kJ mol^{-1})	A_2 ($K^{1/2}$ MPa^{-1})	E_2 (kJ mol^{-1})
CNS-201	9.77	0.49	0.58	0.061	17.2	0.0044	16.4
MSC-30	41.0	2.30	0.70	0.068	13.4	0.0046	12.9
ZTC-3	35.6	2.04	0.46	0.059	11.6	0.00018	20.4

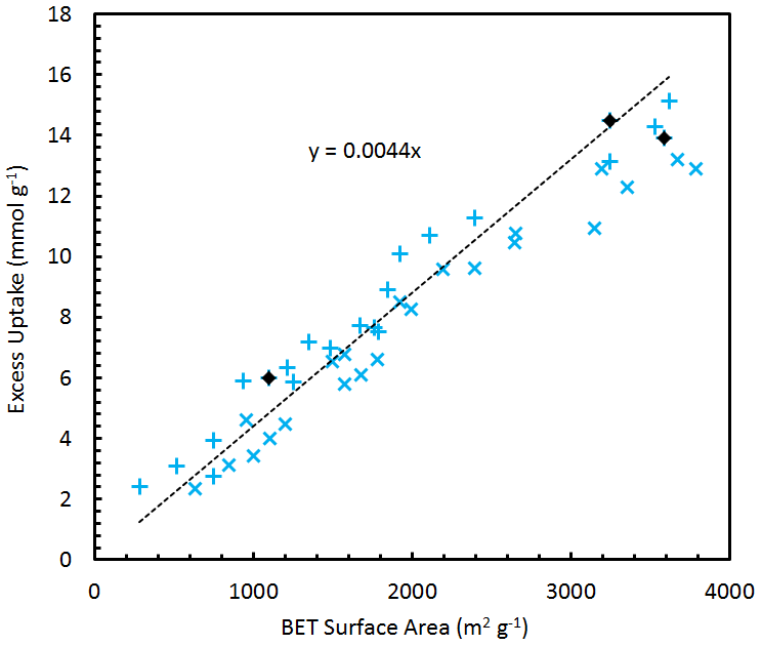

Figure 5.8. Equilibrium excess adsorption uptake of methane as a function of BET surface area, reported at the excess maximum at 298 K for CNS-201, MSC-30, and ZTC-3 (black diamonds). A + indicates a reported value from the literature.[25] A × indicates a reported value of the BET monolayer capacity from the literature.[27]

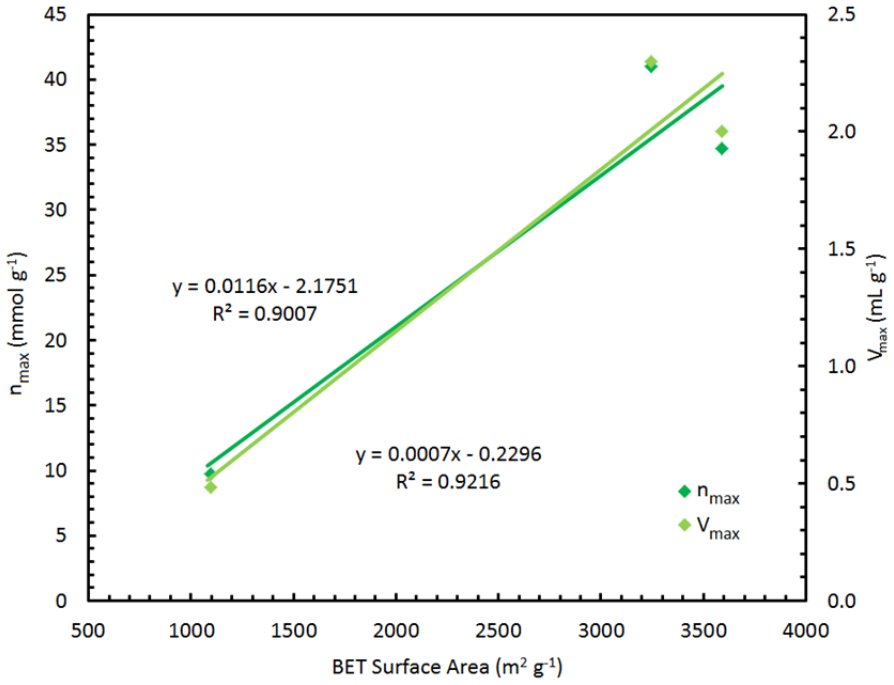

Figure 5.9. The dependence of fit parameters n_{max} and V_{max} on BET surface area for CNS-201, MSC-30, and ZTC-3.

5.3 Enthalpy of Adsorption

The thermodynamic quantity of interest for adsorbent materials is the differential enthalpy of adsorption,[24] ΔH_{ads}, often obtained by the isosteric method and reported as the positive value q_{st}, the isosteric heat of adsorption.[25] We refer to the quantity as "enthalpy" but use the following (positive) definition:

$$q_{st} = -\Delta H_{ads}(n_a) = T\left(\frac{\partial P}{\partial T}\right)_{n_a}\left(v_g - v_a\right)$$

Equation 5.1

It is necessary to use this general form of the Clausius-Clapeyron relationship for methane adsorption at high pressure due to the significant non-ideality of methane gas-state properties, preventing the usual van't Hoff analysis. The real (REFPROP)[26] bulk gas density was used and the adsorbed density was approximated as limited by liquid methane (see Section 2.3.3), giving significantly different results than by assuming ideal gas density. The isosteric enthalpy of adsorption of methane on CNS-201, MSC-30, and ZTC-3 at the temperatures measured is shown in Figure 5.10. A detailed analysis of alternative methods of the calculation of adsorption enthalpy is given in Chapter 2.

The Henry's law values of the isosteric enthalpy of adsorption for CNS-201, MSC-30, and ZTC-3 are 18.0-19.3, 14.4-15.5, and 13.5-14.2 kJ mol^{-1}, respectively. The same temperature dependence of this value is found for both activated carbons: +4.1 J mol^{-1} K^{-1}. The Henry's law values from 238-518 K for ZTC-3 depend nonlinearly on temperature, indicating significantly different thermodynamics of methane adsorption in this range. At low temperatures the trend is negative (-16 J mol^{-1} K^{-1} at 247 K), and

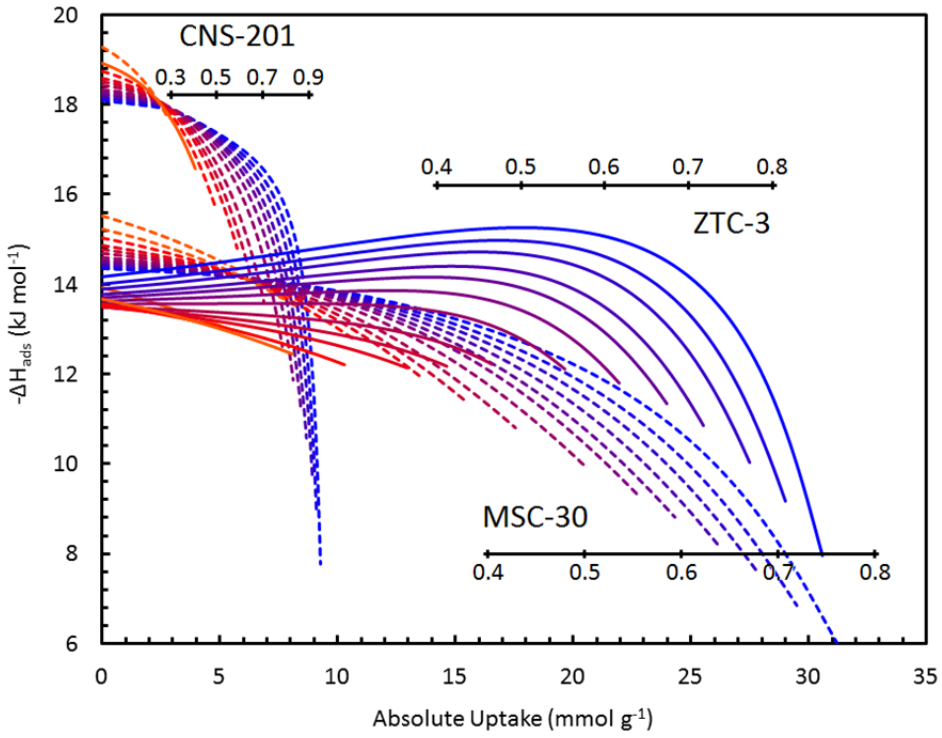

Figure 5.10. Isosteric enthalpy of adsorption of methane on CNS-201, MSC-30, and ZTC-3 from 238-523 K (color indicates the temperature from low to high as blue to red). Scale bars of the fractional site occupancy (specific to each material) are inset.

then increases toward that of the activated carbons (reaching +3.0 J mol^{-1} K^{-1} at 450 K).

The characteristics of methane adsorption as a function of fractional site occupancy, ϑ, in the activated carbons (CNS-201 and MSC-30) are typical of other carbon materials, gradually decreasing with increased uptake. On the contrary, the dependence of the isosteric enthalpy of adsorption on site occupancy in ZTC-3 increases with ϑ at all temperatures, from 238-518 K. The enthalpy increases to a maximum at ϑ = 0.5-0.6, and then declines rapidly at high uptake. The rapid decline is similar in all three materials, occurring at ϑ > 0.7, and is a result of high, non-ideal density in the high-pressure gas; an ideal gas approximation would be completely invalid in this high-pressure regime.

5.4 Entropy of Adsorption

The molar differential entropy of adsorption, while less relevant to engineering applications, is a readily accessible quantity of adsorption via the isosteric method following the procedure in Section 2.3.2. The pressure dependence of the entropy of the pure gas phase can be obtained from the REFPROP database. Together, these quantities can be used to calculate the entropy of methane in the adsorbed phase, given by:

$$S_a(P,T) = \Delta S_{ads}(P,T) + S_g(P,T)$$

Equation 5.2

The entropy of the adsorbed phase, S_a, on CNS-201, MSC-30, and ZTC-3 is shown in Figure 5.11, where the reference state is the normal boiling point of methane, 111.5 K at 0.1 MPa. While all three materials show a similar change in entropy with increased uptake, there are notable differences between that for the small-pore materials (CNS-201 and ZTC-3) and MSC-30, which has pores ranging in width up to > 4 nm. The high-pressure entropy of methane adsorbed on CNS-201 and ZTC-3 at 238 K resembles that at the reference state rather closely, despite being ~100 K above those conditions, indicating a liquid-like behavior of the adsorbed layer. This is, however, a subtle difference and MSC-30 may show a similar effect at slightly lower temperatures. The rise in entropy at the highest pressures measured is not well understood, but corresponds to the sharp decrease in enthalpy shown in Figure 5.10. This regime corresponds to filling the last adsorption sites available, and could reflect some contribution from disorder in the filling of those sites.

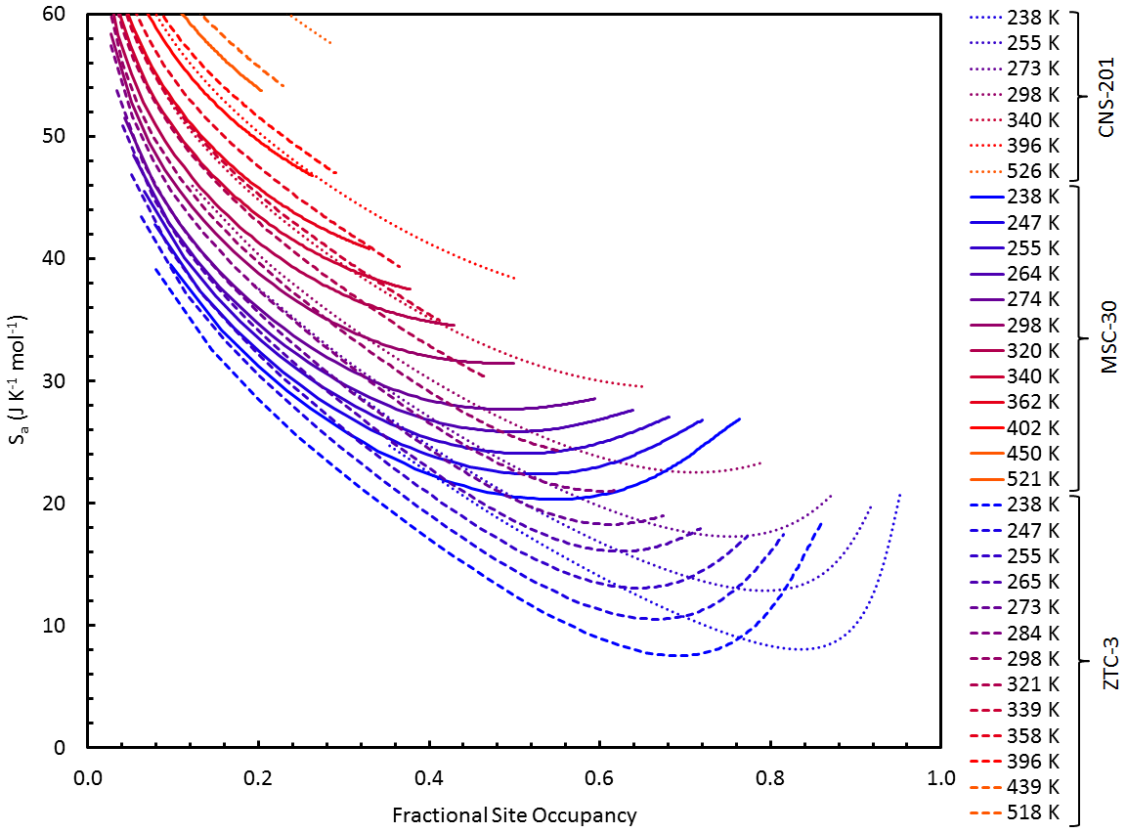

Figure 5.11. Entropy of methane in the adsorbed phase as a function of fractional site occupancy.

5.5 Discussion

The increasing isosteric enthalpy of adsorption in ZTC-3 is anomalous compared to previous experimental reports of methane adsorption on carbon. However, it is consistent with calculations of methane adsorption in graphitic slit pores of fixed width[6, 27] where methane-methane interactions between adsorption sites are expected to have a significant role.[28] Its rise of 1.2 kJ mol^{-1} at 298 K corresponds to a 10% increase, remarkably consistent with recent calculations of the relative contribution of lateral

interactions to the enthalpy of adsorption of methane on CPU-27-Mg[15] and on molecular sieves.[10] The possibility of entropic contributions (e.g., from additional vibrational modes of bound CH_4 molecules) cannot be ruled out and further investigation with deuterated molecules would be interesting.

Surface homogeneity is not a requirement for increased interactions between binding sites, but would certainly enhance the measurable effect on the enthalpy of adsorption at high uptake. The material properties of ZTC-3, such as a narrow distribution of pore-width, periodic pore-spacing, and high content of sp^2 hybridized carbon (as characterized by NMR and numerous other techniques[29]), suggest a high binding site homogeneity is probable. The average distance between adsorbed methane molecules (approximated as the square root of the BET surface area per molecule) at the surface excess maximum was the same in all three materials in this study (e.g., 0.5 nm at 238 K) and well within the distance applicable to attractive lateral interactions.

We therefore assert that lateral interactions play a major role in methane adsorption on ZTC-3, overcoming any heterogeneities in the surface and causing a significant overall rise in enthalpy of adsorption as site occupancy increases, though it is not possible to determine the precise magnitude of this effect since surface homogeneity is unknown.

5.6 Conclusions

An increasing (or even constant) isosteric enthalpy of adsorption over a large regime of temperature and pressures is a highly desirable characteristic of an adsorbent

material. It benefits deliverable storage capacity because a large fraction of the maximum adsorption capacity is contained at pressures above the lower bound of useful storage (e.g., P_f = 0.3 MPa for delivery to a fuel cell) rather than below it, as in materials with a high initial binding energy that decreases with loading. Due to the flexibility of the template-carbonization synthesis, the pore-width can be adapted to other adsorptive gases by simply changing the template, making this a highly promising approach for the design of adsorbent materials for gases with attractive intermolecular forces. Indeed, the deliverable gravimetric methane capacities of ZTC-3 at temperatures near ambient are among the highest of any reported carbonaceous materials, a direct result of enhancing thermodynamic performance in the surface coverage regime of interest ($P > P_f$).

5.7 References

(1) S. K. Bhatia and A. L. Myers, 'Optimum conditions for adsorptive storage', *Langmuir,* **22**, 1688-1700 (2006).

(2) A. Chakraborty, B. B. Saha, K. C. Ng, S. Koyama, and K. Srinivasan, 'Theoretical insight of physical adsorption for a single component adsorbent + adsorbate system: II. The Henry region', *Langmuir,* **25**, 7359-7367 (2009).

(3) T. C. M. Chung, Y. Jeong, Q. Chen, A. Kleinhammes, and Y. Wu, 'Synthesis of microporous boron-substituted carbon (B/C) materials using polymeric precursors for hydrogen physisorption', *J. Am. Chem. Soc.,* **130**, 6668-6669 (2008).

(4) Z. Jin, Z. Z. Sun, L. J. Simpson, K. J. O'Neill, P. A. Parilla, Y. Li, N. P. Stadie, C. C. Ahn, C. Kittrell, and J. M. Tour, 'Solution-phase synthesis of heteroatom-substituted carbon scaffolds for hydrogen storage', *J. Am. Chem. Soc.,* **132**, 15246-15251 (2010).

(5) Y. Xia, G. S. Walker, D. M. Grant, and R. Mokaya, 'Hydrogen storage in high surface area carbons: experimental demonstration of the effects of nitrogen doping', *J. Am. Chem. Soc.,* **131**, 16493-16499 (2009).

(6) K. R. Matranga, A. L. Myers, and E. D. Glandt, 'Storage of natural gas by adsorption on activated carbon', *Chem. Eng. Sci.,* **47**, 1569-1579 (1992).

(7) D. Nicholson, 'Simulation studies of methane transport in model graphite micropores', *Carbon,* **36**, 1511-1523 (1998).

(8) D. Lozano-Castello, D. Cazorla-Amoros, A. Linares-Solano, and D. F. Quinn, 'Influence of pore size distribution on methane storage at relatively low pressure: preparation of activated carbon with optimum pore size', *Carbon,* **40**, 989-1002 (2002).

(9) Z. Jin, W. Lu, K. J. O'Neill, P. A. Parilla, L. J. Simpson, C. Kittrell, and J. M. Tour, 'Nano-engineered spacing in graphene sheets for hydrogen storage', *Chem. Mater.,* **23**, 923-925 (2011).

(10) M. M. K. Salem, P. Braeuer, M. Szombathely, M. Heuchel, P. Harting, K. Quitzsch, and M. Jaroniec, 'Thermodynamics of high-pressure adsorption of argon, nitrogen, and methane on microporous adsorbents', *Langmuir,* **14**, 3376-3389 (1998).

(11) P. Bénard and R. Chahine, 'Determination of the adsorption isotherms of hydrogen on activated carbons above the critical temperature of the adsorbate over wide temperature and pressure ranges', *Langmuir,* **17**, 1950-1955 (2001).

(12) T. Kyotani, 'Control of pore structure in carbon', *Carbon,* **38**, 269-286 (2000).

(13) H. Nishihara and T. Kyotani, 'Templated nanocarbons for energy storage', *Adv. Mater.,* **24**, 4473-4498 (2012).

(14) Y. Sun, C. Liu, W. Su, Y. Zhou, and L. Zhou, 'Principles of methane adsorption and natural gas storage', *Adsorption,* **15**, 133-137 (2009).

(15) K. Sillar and J. Sauer, 'Ab initio prediction of adsorption isotherms for small molecules in metal-organic frameworks: the effect of lateral interactions for methane/CPO-27-Mg', *J. Am. Chem. Soc.*, doi: 10.1021/ja307076t (2012).

(16) H. Nishihara, P. X. Hou, L. X. Li, M. Ito, M. Uchiyama, T. Kaburagi, A. Ikura, J. Katamura, T. Kawarada, K. Mizuuchi, and T. Kyotani, 'High-pressure hydrogen storage in zeolite-templated carbon', *J. Phys. Chem. C,* **113**, 3189-3196 (2009).

(17) B. Panella, M. Hirscher, and S. Roth, 'Hydrogen adsorption in different carbon nanostructures', *Carbon,* **43**, 2209-2214 (2005).

(18) T. P. McNicholas, A. Wang, K. O'Neill, R. J. Anderson, N. P. Stadie, A. Kleinhammes, P. Parilla, L. Simpson, C. C. Ahn, Y. Wang, Y. Wu, and J. Liu, 'H2 storage in microporous carbons from PEEK precursors', *J. Phys. Chem. C,* **114**, 13902-13908 (2010).

(19) J. J. Purewal, H. Kabbour, J. J. Vajo, C. C. Ahn, and B. Fultz, 'Pore size distribution and supercritical hydrogen adsorption in activated carbon fibers', *Nanotechnology,* **20**, 204012 (2009).

(20) N. P. Stadie, J. J. Purewal, C. C. Ahn, and B. Fultz, 'Measurements of hydrogen spillover in platinum doped superactivated carbon', *Langmuir,* **26**, 15481-15485 (2010).

(21) T. Kiyobayashi, H. T. Takeshita, H. Tanaka, N. Takeichi, A. Züttel, L. Schlapbach, and N. Kuriyama, 'Hydrogen adsorption in carbonaceous materials – how to determine the storage capacity accurately', *J. Alloys Compd.,* **330-332**, 666-669 (2002).

(22) J. Purewal, D. Liu, A. Sudik, M. Veenstra, J. Yang, S. Maurer, U. Müller, and D. J. Siegel, 'Improved hydrogen storage and thermal conductivity in high-density MOF-5 composites', *J. Phys. Chem. C,* **116**, 20199-20212 (2012).

(23) E. Poirier, R. Chahine, and T. K. Bose, 'Hydrogen adsorption in carbon nanostructures', *Int. J. Hydrogen Energ.,* **26**, 831-835 (2001).

(24) S. Sircar, R. Mohr, C. Ristic, and M. B. Rao, 'Isosteric heat of adsorption: theory and experiment', *J. Phys. Chem. B,* **103**, 6539-6546 (1999).

(25) F. Rouquerol, J. Rouquerol, and K. S. W. Sing, *Adsorption by powders and porous solids: principles, methodology, and applications*, Academic Press, San Diego (1999).

(26) E. W. Lemmon, M. L. Huber, and M. O. McLinden, 'NIST standard reference database 23: reference fluid thermodynamic and transport properties − REFPROP', Number Version 8.0 in Standard Reference Data Program (2007).

(27) R. F. Cracknell, P. Gordon, and K. E. Gubbins, 'Influence of pore geometry on the design of microporous materials for methane storage', *J. Phys. Chem.,* **97**, 494-499 (1993).

(28) S. A. Al-Muhtaseb and J. A. Ritter, 'Roles of surface heterogeneity and lateral interactions on the isosteric heat of adsorption and adsorbed phase heat capacity', *J. Phys. Chem. B,* **103**, 2467-2479 (1999).

(29) N. P. Stadie, J. J. Vajo, R. W. Cumberland, A. A. Wilson, C. C. Ahn, and B. Fultz, 'Zeolite-templated carbon materials for high-pressure hydrogen storage', *Langmuir,* **28**, 10057-10063 (2012).

Chapter 6

Conclusions

6.1 Summary of Results

The motivation of the studies presented in this thesis was twofold: to gain thermodynamic insights into the mechanism of physical adsorption at the solid-gas interface that can be effectively applied to the design of future energy storage materials, and to accurately determine the adsorptive properties of key materials that have received attention for their reported extraordinary physisorptive storage of hydrogen toward understanding the key material properties that can be tuned to reach maximum adsorption densities. We seek to assist in determining if physisorptive materials can be developed to meet the needs of the transportation sector.

It is long established that physisorptive hydrogen uptake is well approximated as proportional to surface area in carbonaceous materials, and thus specific surface area is the benchmark material property for determining the "ballpark" hydrogen capacity of a new material. The relationship depends on temperature and pressure, and is commonly stated at 77 K and the surface excess maximum pressure. This specific relationship, "Chahine's rule," roughly predicts 1 wt% H_2 uptake per 500 $m^2\ g^{-1}$ of specific surface

area, corresponding to 6 molecules per square nm. The prediction is inexact, as we find the precise description of this relationship to be 0.009±0.001 mmol m^{-2}, or 5.6±0.8 molecules per square nanometer (see Section 4.5.2). A caveat is that, for carbonaceous materials, the relationship reaches a limit at ~3000 m^2 g^{-1}: relatively few higher surface area materials have been reported and the trend seems to level off.

Finding a material that deviates from this trend (significantly higher than scatter) has been the goal of the physisorptive hydrogen storage community in recent years. Two notable reports of enhanced uptake that have drawn significant attention are those of (atomic) hydrogen sorption by metal-assisted spillover and anomalous hydrogen adsorption densities in zeolite templated-carbons at high pressure (>10 MPa). We have focused on both of these systems in this study to understand the underlying principles of their anomalous behaviors, and presented a detailed assessment of their hydrogen storage properties in Chapters 3 and 4.

Toward new materials which could realize significantly higher adsorptive storage than that of typical activated carbons, we focused on methane adsorption since it is possible to perform extremely detailed thermodynamic studies in a region beyond that of the ideal gas. We collected a very large data set of high-pressure methane isotherms between 238-526 K up to 9 MPa, and with careful treatment of the data, were able to shed remarkable insight into the thermodynamics of adsorption in the carbon materials studied. Specifically, we showed that in zeolite-templated carbon ZTC-3, a combination of tuned material properties and strong, attractive methane-methane interactions in the adsorbed phase contributed to an anomalous increase in isosteric enthalpy of

adsorption with increased site occupancy at high pressure, presented in Chapter 5. We employed a simple and effective model to estimate the absolute adsorption from high-pressure experimental data, a key technique for extracting the level of detail from adsorption data that was necessary for this study (detailed in Chapter 2).

In summary, three primary results are presented in this thesis:

i. the addition of platinum nanoparticles to the surface of activated carbon, while creating suitable conditions for metal-assisted hydrogen spillover, does not appreciably enhance reversible hydrogen uptake above the pure supporting material,

ii. the physisorptive hydrogen storage capacity of zeolite-templated carbon is among the highest known for pure carbonaceous materials, but is ultimately proportional to surface area at all conditions measured, and

iii. the adsorption of methane on zeolite-templated carbon is anomalous compared to other physisorptive materials, showing an increase in isosteric enthalpy with uptake, a result of enhanced adsorbate-adsorbate interactions in the adsorption phase.

6.1.1 Hydrogen Spillover for Storage Applications

At the time of our investigation of metal-assisted hydrogen spillover materials, the factor of 2 enhancement reported for the Pt/AX-21 system and, similarly, the 8 times enhancement reported for “bridged” IRMOF-8 were perhaps the most prominent experimental results that suggested reversible hydrogen adsorption could be accomplished at significant capacities at room temperature. At the same time, these

results were poorly understood theoretically, sometimes referred to as “weak chemisorption” rather than physisorption, and the experimental evidence was limited to volumetric hydrogen sorption measurements that was unreproduced by other groups. Our efforts were to be initially focused on the simplest possible spillover system, since exposed transition metal sites (such as in MOFs), hydrogen absorbing metals (e.g., palladium nanoparticles), and organic molecule “bridges” were seen to be complicating variables and were reported as unnecessary to achieve significant enhancement of hydrogen uptake capacity. Platinum nanoparticles supported by a well-characterized support material was the chosen system for initial studies, equivalent to the previously reported Pt/AX-21. We synthesized materials, optimized the material properties for spillover (especially reducing nanoparticle size and increasing dispersion), and ultimately achieved products, referred to as Pt-MSC-30, which could not be differentiated from others in the literature based on typical characterization techniques: XRD, TEM, and TGA. Hydrogen sorption properties were assessed, first by standard techniques, and due to large uncertainties in the results, also by significantly more accurate methods. One unique quality of spillover compared to traditional physisorption is its long duration, reported to be 1-2 orders of magnitude longer in equilibration time due to surface diffusion of the atomic hydrogen, requiring alterations to our standard measurement apparatus and techniques to minimize numerous sources for substantial errors.

Our ultimate results, assured by increasing the signal to noise capabilities of our Sieverts instrument by a factor of 10-16, showed that the enhancement of hydrogen uptake capacity by spillover was below the detection limit of volumetric adsorption

measurements in Pt-MSC-30. We were not able to confirm the 100% increase associated with an otherwise identical system, Pt/AX-21, but were able to pinpoint possible sources of error accumulation in the methods of its measurement. Further work, including measurements from our lab as well as collaborators, has supported our initial results and refined our estimate of the magnitude of this effect in terms of storage. Details are provided in Appendix B.

6.1.2 Anomalous Adsorption Properties of Zeolite-Templated Carbons

Zeolite-templated carbons (ZTCs), a class of materials with extremely high surface area and narrow microporosity, received enthusiastic attention after the report of significantly increased hydrogen storage capacities at pressures between 10-34 MPa. To investigate the reported unique properties of adsorption in ZTCs at high pressure, where few instruments are capable of adsorption measurements, we designed, constructed, and commissioned an apparatus capable of measurements up to 70 MPa. In addition, we succeeded at synthesizing relatively large quantities of high surface area, high template-fidelity ZTCs comparable in quality to those reported in the literature. However, hydrogen adsorption characteristics of ZTCs were consistent with other carbonaceous materials, even beyond 10 MPa where it had previously been reported to differ. We established a “Chahine’s rule” relation of excess hydrogen capacity at 298 K and 30 MPa, 2.3 mmol g^{-1} per 1000 m^2 of BET surface area, or 1.4 H_2 per square nanometer for carbonaceous materials. The enthalpy of adsorption of hydrogen in ZTCs was also shown to be similar to other carbons, but interestingly, skeletal density was significantly lower in ZTCs due to a high H content as determined by elemental analysis

experiments. While the hydrogen adsorption properties of ZTCs are typical of other carbons, the unique periodic pore spacing, extremely high surface area, and practical synthetic procedures make ZTCs a highly interesting class of materials for adsorption applications beyond high-pressure hydrogen storage.

Following hydrogen, we investigated the methane adsorption properties of ZTCs with the motivation that strong, attractive intermolecular interactions would significantly alter the chemical potential environment, even at temperatures and pressures near ambient conditions. This was a convenient realization since extremely detailed thermodynamic information could be harvested with relative ease for methane, where hydrogen studies are much more limited (unless a helium cryostat is available). We measured methane adsorption uptake as a function of pressure at 13 temperatures between 238-526 K, the regime of practical importance for methane storage applications, and amassed one of the largest data sets for methane adsorption on high surface area carbonaceous materials. Combined with a simple and effective model for determining the absolute quantity of adsorption, this study lead to the central result presented in this thesis: the increasing isosteric enthalpy of methane adsorption with increasing uptake in faujasite-templated carbon, ZTC-3. This is an interesting and highly desirable deviation from the typical properties of high surface area carbonaceous materials, where the isosteric enthalpy of adsorption is usually observed to decline with uptake. It is intuitive that binding heterogeneities in high surface area carbons (where edge terminations, defects, and surface roughness typically contribute to the extremely high surface area quality of the material) ensure that high energy sites are filled

preferentially to low energy ones. However, it is precisely the homogeneous distribution of extremely narrow channels in ZTCs that lend the unique property of enhanced binding as fractional occupancy in the adsorbed phase increases.

The direct cause of this effect is not ascertainable without a better understanding of the relative roles of the strong lateral interactions of methane in the adsorbed phase and the extent of binding site homogeneity in ZTC. However, we can estimate that the lateral interactions are quite important in light of their importance to gas-phase properties of methane in this pressure and temperature regime. We cannot rule out entropic contributions, and analysis showed that the entropy of the adsorbed phase resembled that of liquid methane in the high-pressure region. In any case, templated-carbons remain an exciting class of materials and much remains to be investigated in this area.

6.2 Future Work

6.2.1 Zeolite-Templated BC_x Materials

Substitutional doping of carbon with beryllium, boron, and other light elements by solid-state diffusion has been discussed as a promising route toward increasing hydrogen binding energy. In particular, computational analysis shows that the strongly localized empty p_z orbitals at a Be or B site substituted within a graphite-like surface interacts with the occupied orbital of H_2, leading to a partial charge transfer from H_2 to the surface. Significantly higher hydrogen binding energy (~11 kJ mol^{-1}) has been reported experimentally for boron-doped carbon (BC_x) materials,[1] though surface areas

in these systems are limited to < 1000 m^2/g. As a result of stronger binding, hydrogen uptake is found to be increased by up to 50% in microporous BC_x materials compared to pure carbon materials of similar surface area. Compounds of beryllium-doped carbon are expected to have even higher hydrogen binding energy, but are unknown experimentally.

In practice, it is difficult to obtain boron levels in carbon greater than ~10 wt% by standard synthesis techniques.[1] Alternatively, graphite-like BC_3 (shown in Figure 6.1) has a high B:C ratio, but its synthesis is typically performed on the surface of a thin substrate inside a flow-through tube furnace.[2-4] Fabrication of high surface area sorbents with a chemical structure resembling BC_3 would be of significant interest for hydrogen physisorption. The precursors necessary for producing graphite-like BC_3 (boron trichloride and benzene) are both readily adsorbed by zeolites, and we suggest that under the right conditions, a BC_3-like coating could be formed on the inner surface of the zeolite template. Subsequent removal of the zeolite template as in ZTC synthesis should yield an amorphous BC_x ($x \approx 3$) material that exhibits extremely high surface area, narrow microporosity, and a homogeneous distribution of elevated hydrogen binding energies.

Our initial attempts at producing BC_3 are shown in Figure 6.2, where we have collected the product on a silicon substrate. The energy-loss spectrum shows boron and carbon K-edges with a boron concentration over twice that of the known solubility limit, but still half of that expected for pure BC_3. With the substantial potential for refinement

of the processing technique (involving the careful handling of corrosive gas precursors) in mind, this is a promising first result.

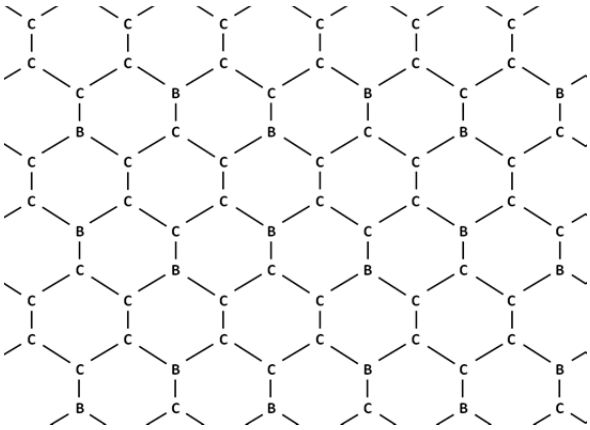

$$C_6H_6 + 2\,BCl_3 \rightarrow 2\,BC_3 + 6\,HCl$$

Figure 6.1. BC_3 synthesis reaction and chemical structure.

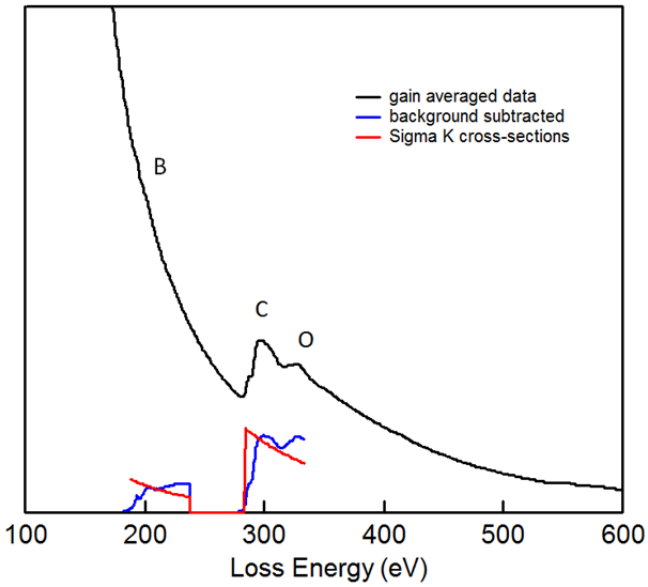

Figure 6.2. EELS spectrum of an early attempt to synthesize BC_3 on a silicon substrate.

6.2.2 Pressure to Change Chemical Potential: Carbon Nanotubes

Pressure can be used as a dial to tune the chemical energy environment of a gas-solid system. The chemical potential, μ, of a single-component gas held at a fixed temperature (the molar Gibbs free energy) increases proportional to ln P, that is, until the ideal gas limit is surpassed. The nature of the chemical potential in the non-ideal gas region for hydrogen and methane is plotted as a function of pressure in Figure 6.3, with reference to an arbitrary state so that $\mu(P,T)$ is 0 at P = 0.001 MPa. The deviation from ideality is positive for H_2 at all temperatures between 77-523 K, due to Pauli repulsion, while it has a negative initial deviation for CH_4 at low temperatures due to attractive intermolecular forces. Both gases show a positive deviation at high temperatures and pressures.

The proposed future work concerns using the change in chemical potential associated with a decrease in pressure to drive a phase transition between different states of surface exposure in a material. Single-walled carbon nanotubes are known to form bundled structures, bound by weak van der Waals forces between nanotubes, analogous to the inter-planar forces between graphene sheets in the structure of graphite. , bound by weak van der Waals forces between nanotubes, analogous to the inter-planar forces between graphene sheets in the structure of graphite. The magnitude of the binding interaction between planar carbon surfaces is not precisely known, but is often estimated to be ~50 meV per C in pure graphite. Within the last 10 years, the binding energy has been calculated to fall within the range of 8-200 meV per C. Misalignments, curvature, and defects in nanotubes could result in a lower value. It is

possible to probe this interaction using adsorption; if the chemical potential of the adsorptive phase exceeds that between self-interacting surfaces, it is plausible that a phase transition will proceed to expose a larger area for adsorption. The change in state from bundles to individual nanotubes would be accompanied by a large change in available surface for adsorption, and it is possible to design an experiment to test this.

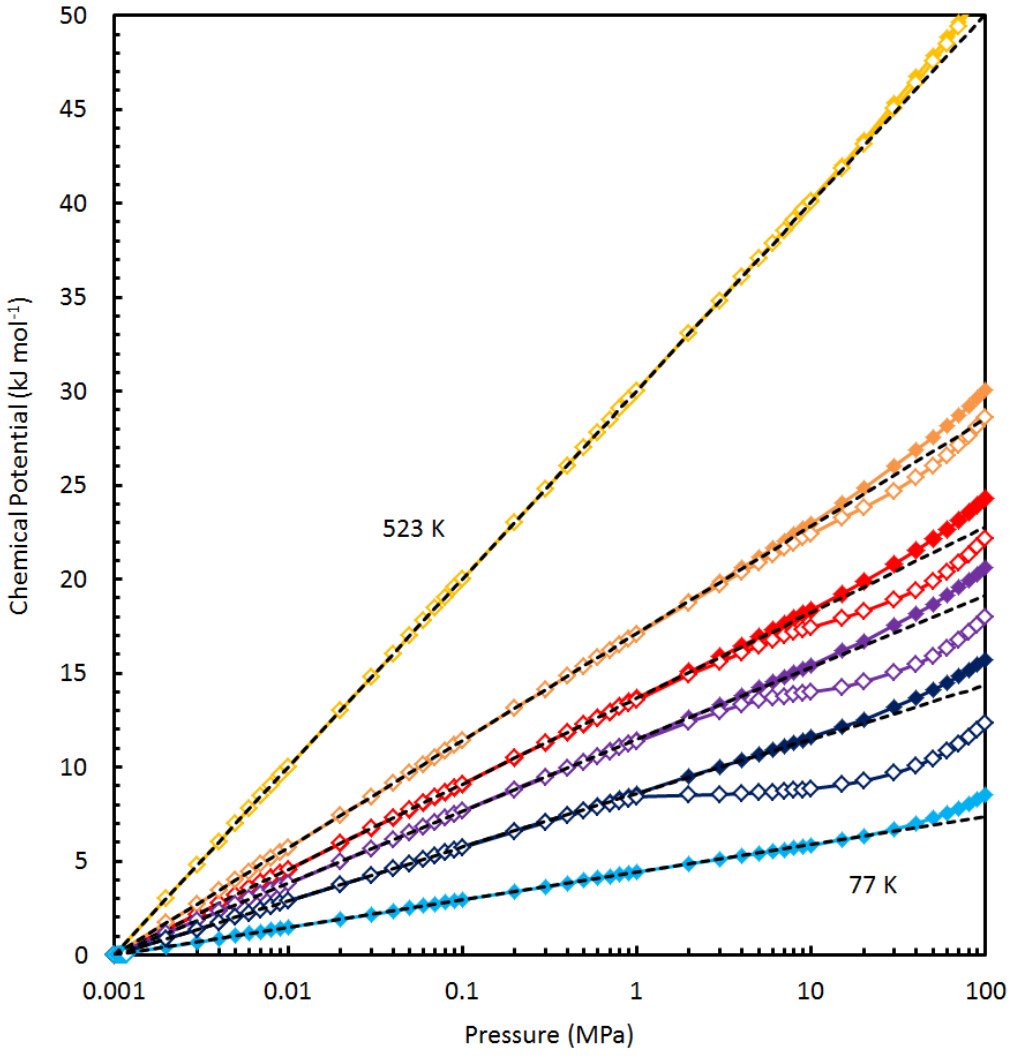

Figure 6.3. Chemical potential of methane (unfilled diamond) and hydrogen (filled diamond) at 77 K (light blue), 150 K (dark blue), 200 K (purple), 238 K (red), 298 K (orange), and 523 K (yellow). The reference state has been adjusted so that all curves intersect at P = 0.001 MPa and μ = 0 kJ mol^{-1}, for clarity.

The regime where the most chemical potential is available for driving this transition is one where the change in chemical potential with pressure is steepest. Adsorption on the large exposed area would result in a significantly lower final pressure of the system, a state with lower free energy than that in which the nanotubes remain bundled.

With some simple approximations, and using actual measured data for the amount of adsorbed hydrogen or methane as a function of pressure, we can predict the conditions which are most likely to result in un-bundling. It seems hydrogen, with its large positive slope in chemical potential with pressure, would be the better candidate gas. Secondly, lower temperatures, despite having a more gradual change in chemical potential with pressure, yield much higher surface coverages at the final pressure of the adsorption system, giving the highest values of change in chemical potential per C. A practical temperature would be 77 K. First approximations of the magnitude of this effect achievable in our laboratory predict at least 1-2 meV per C is possible within acceptable pressures, but would benefit from a specifically designed apparatus with carefully adjusted volumes (refer to Appendix E). An ideal setup would be to have a large sample with as much exposable surface as possible contained in the smallest void, thus giving the largest possible change in pressure on adsorption and exploiting the maximum chemical potential available in the gas phase.

While applications of this proposed idea are not obvious, it is possible that a material which undergoes such a pressure driven transition to a high surface area phase could have promising applications for energy storage since large changes in adsorption uptake would be possible with small changes in system pressure.

6.3 References

(1) T. C. M. Chung, Y. Jeong, Q. Chen, A. Kleinhammes, and Y. Wu, 'Synthesis of microporous boron-substituted carbon (B/C) materials using polymeric precursors for hydrogen physisorption', *J. Am. Chem. Soc.,* **130**, 6668-6669 (2008).

(2) J. Kouvetakis, R. B. Kaner, M. L. Sattler, and N. Bartlett, 'A novel graphite-like material of composition BC3, and nitrogen-carbon graphites', *J. Chem. Soc., Chem. Commun.*, 1758-1759 (1986).

(3) R. B. Kaner, J. Kouvetakis, C. E. Warble, M. L. Sattler, and N. Bartlett, 'Boron-carbon-nitrogen materials of graphite-like structure', *Mat. Res. Bull.,* **22**, 399-404 (1987).

(4) K. M. Krishnan, J. Kouvetakis, T. Sasaki, and N. Bartlett, 'Characterization of newly synthesized novel graphite films', *Mat. Res. Soc. Symp. Proc.,* **121**, 527-530 (1988).

Appendix A: Experimental Adsorption Measurements

A.1 Overview

Physical adsorption at the gas/solid interface is routinely measured in the laboratory. The most common example is found in measuring nitrogen adsorption isotherms of porous materials at 77 K between 0-100 kPa, which corresponds to the full range of P/P_0 for nitrogen (P_0 is the saturation pressure). The wide and cheap availability of nitrogen as a gas and liquid (used for cooling to 77 K) combined with its practicality as a probe molecule in determining surface area and pore size characteristics has established N_2 adsorption as a ubiquitous characterization tool and commercial instruments specifically for this purpose are widespread. In addition, commercial instruments are available for measuring the sorption of other gases such as hydrogen, carbon dioxide, and methane. Due to the complexity of these measurements and the subtleties of performing experiments across various adsorbents, adsorbates, and within different regimes of temperature and pressure, the dependability of even the most sophisticated commercial systems is inconsistent. More sophisticated apparatus and computer control typically goes along with less freedom to the scientific user. A typical pitfall is to assume that a greater number of data points may be used to overcome errors in measurement. In regimes of high temperature and pressure, systematic errors in adsorption measurement are substantial, and their effects are *cumulative*. Adsorptive

gases such as nitrogen and carbon dioxide are relatively easy to accurately measure due to larger changes in pressure and mass upon adsorption as well as typically stronger adsorption interactions. Hydrogen adsorption, on the other hand, must be measured with more care, due mainly to its lower specific uptake amounts in most materials as a result of weaker binding interactions compared to other gases (the implications for *ab*sorptive hydrogen uptake are different).

As adsorption occurs at the gas-solid interface, the weight of the solid increases and the pressure of the gas decreases. Thus, the amount adsorbed can be measured in at least two ways: by measuring the change in weight of the solid with a spring balance or measuring the change in pressure of the gas in an accurately known volume (if the volume of the sample is also known). These techniques, termed gravimetric and volumetric respectively, are summarized in Figure A.1. The resulting experimental data collected at a constant temperature, referred to as the equilibrium adsorption isotherm, is generally plotted as a function of pressure, or in some cases of P/P_0 where P_0 is the saturation vapor pressure of the adsorbate (typically at pressures below P_0):

$$n_{ads} = f(P)_T \qquad \text{(generally)}$$

$$n_{ads} = f\left(\frac{P}{P_0}\right)_T \qquad \text{(near-saturation regime)}$$

Equation A.1

Adsorption/desorption isotherms of various gases on a commercial sorbent material at different temperatures are shown in Figure A.2. The treatment of data in these distinct temperature regimes is usually different; unless otherwise noted, we will consider the case of near-critical to supercritical temperatures since this is the regime of interest for energy storage applications.

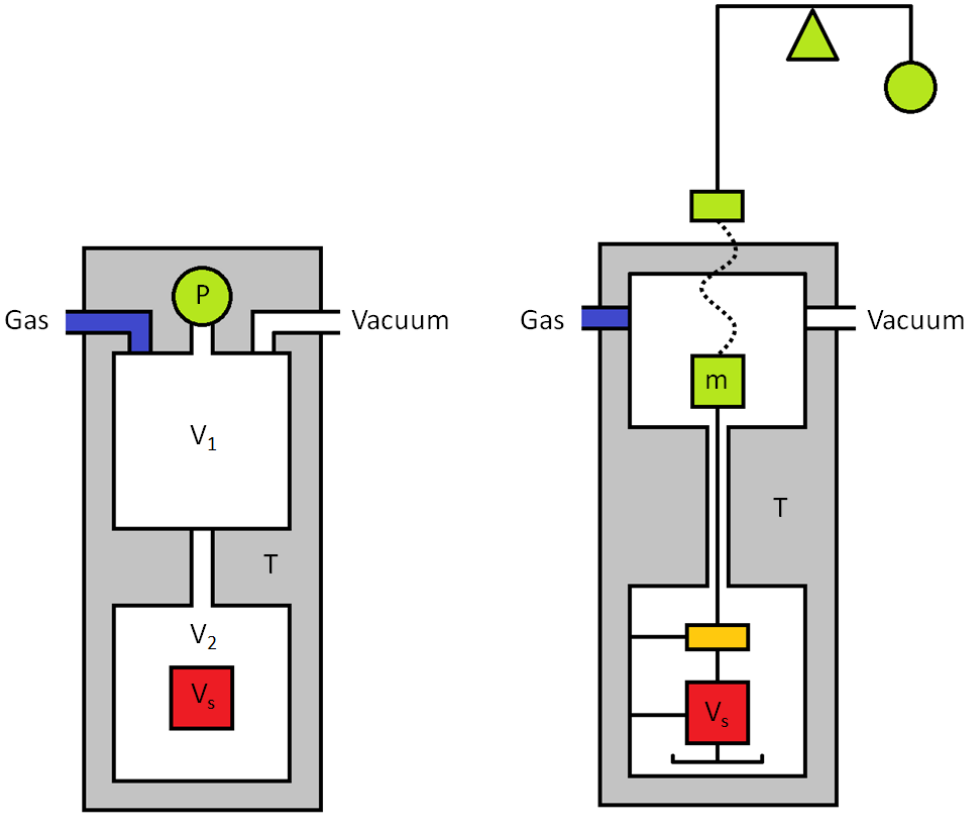

Figure A.1. Schematic representations of the volumetric (left) and gravimetric (right) methods for determining equilibrium gas-solid adsorption isotherms. In the volumetric method, pressure is measured at *P* before and after gas expansions between known volumes V_1 and V_2. In the gravimetric method, the mass of the sample is measured by a suspension balance (a magnetic balance is shown) at *m* as pressure is increased. A second mass, shown in orange, is used for simultaneous determination of the gas density to correct for buoyancy. The primary measurement device is shown in green. The sample volume, shown in red, must be known in both cases

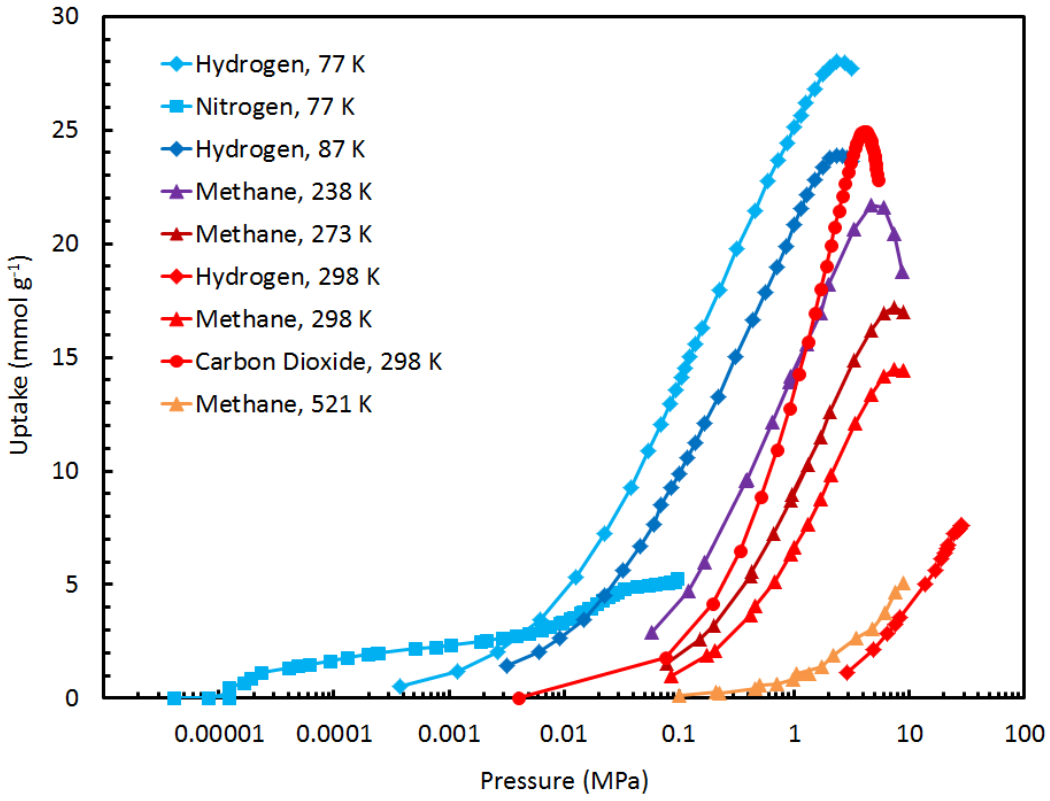

Figure A.2. Equilibrium adsorption isotherms of various adsorptive gases on a superactivated carbon, MSC-30, at temperatures between 77-521 K.

A.2 Volumetric Principles

The most common experimental technique for determining the adsorption uptake of gas by a solid material is the volumetric method. This technique is also referred to as the Sieverts method, a reference to Sieverts law which relates the concentration of gases *absorbed* in metals to pressure.[1] As the name implies, this method is also well suited to determining the absorption uptake quantities in materials.

A schematic representation of a general volumetric apparatus is shown in Figure A.3a. The simplest instrument consists of two accurately known volumes, V_1 and V_2,

separated by a valve, exposed to a pressure measurement device, and held at a constant temperature, *T*. There must be an inlet and outlet for gas. The sample, whose volume (V_s) is also known, is placed in V_2. A practical device is shown in Figure A.3b, where only the sample environment is immersed in a controllable temperature bath while the remainder of the apparatus is held at a constant temperature near ambient. In this case, some of the free gas (corresponding to V_{bath}) will be at the bath temperature, T_{bath}, while the remainder of the apparatus will be at near ambient temperature, T_{app}. For the purposes of the following formalism, we will consider this "practical" apparatus since it is the more common (and more general) experimental setup.

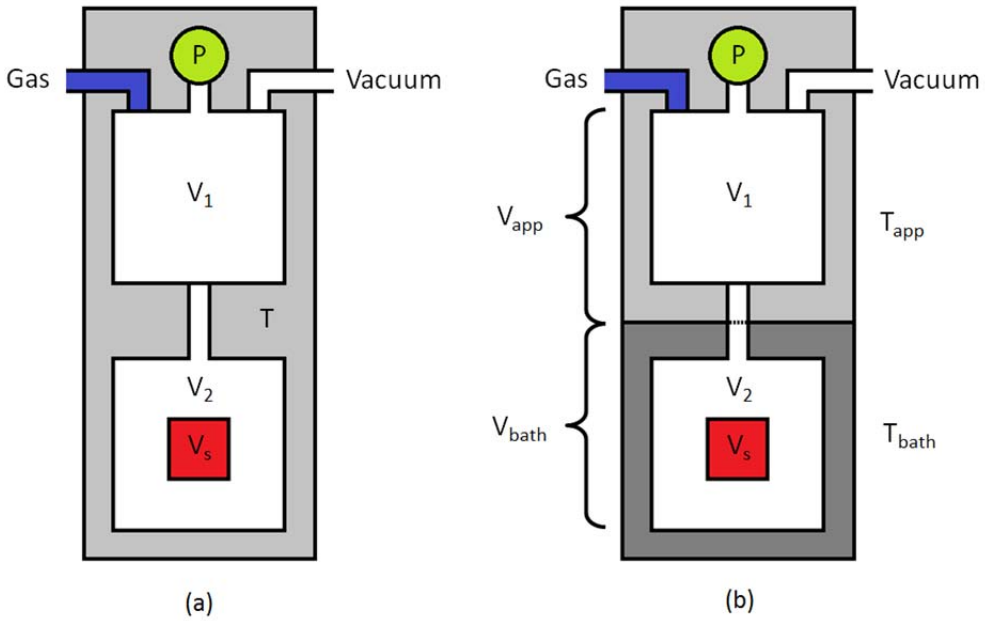

Figure A.3. The volumetric Sieverts apparatus. (a) The simplest apparatus is immersed in a constant temperature bath. (b) A more practical apparatus is held at a constant near-ambient temperature, but contains the sample and a small surrounding volume in a controllable temperature bath. The pressure is measured at *P* and the sample is shown in red. The areas shaded in gray represent a constant temperature region.

Measurement of a single value of the equilibrium adsorption uptake at a certain pressure and temperature requires two steps. In the first step, a specific amount of gas is confined in the "staging manifold," V_1. This initial amount, n_i, is the total amount of gas that will be available for adsorption in the second step. After equilibration, the dosing valve is opened and the gas is expanded into the "reactor," V_2, where it is exposed to the sample. After equilibration, the final amount of adsorptive remaining in the gas phase is n_f and fills a volume V_f. If we assume that the volume of the sample is independent of pressure in our experimental pressure regime (a typical assumption, suggested to be valid by both neutron diffraction measurements[2] and ab initio calculations[3]), we have the following relationships:

$$V_i = V_1$$

Equation A.2

$$V_f = V_1 + V_2 - V_s$$

Equation A.3

The temperatures of the bath and apparatus, T_{bath} and T_{app}, are held constant throughout the experiment. The temperature at the boundary between the bath and apparatus is intermediate between the two. If the volume in this intermediate region is suitably small and if the temperature control in each region is stable, we may approximate the temperature gradient between the two as a step function, so long as the ratio of the volumes of the isothermal regions, b, is accurately known. In the simplest apparatus, this approximation is not necessary. In the general case, the gaseous adsorptive in the final state occupies two isothermal volumes:

$$V_{f,app} = (1 - b)\, V_f$$

Equation A.4

$$V_{f,bath} = b\, V_f$$

Equation A.5

The equilibrium pressure before and after dosing, P_i and P_f, is measured. The density of the free gas is then determined at each step by application of the relevant gas law equation of state, and used to calculate the number of molecules in the gas phase before and after dosing, n_i and n_f, respectively:

$$n_i = \rho(P_i, T_{app})\, V_i$$

Equation A.6

$$n_f = \rho\left(P_f, T_{app}\right) V_{f,app} + \rho(P_f, T_{bath})\, V_{f,bath}$$

Equation A.7

If the reactor volume, V_2, is at zero pressure before the measurement, the (excess) quantity adsorbed is simply the difference between the initial and final number of free gas molecules:

$$n_e\left(P_f, T_{bath}\right) = n_i - n_f$$

Equation A.8

The amount adsorbed is reported as a function of the final conditions in the sample environment. Repeated points are measured in this way at different equilibrium pressures to construct an adsorption uptake isotherm at the constant temperature T_{bath}. If the pressure in V_2 is returned to zero between points, the calculated uptake at the x^{th} point is always the same:

$$n_{e,x}(P_f, T_{bath}) = n_{i,x} - n_{f,x}$$

Equation A.9

If a cumulative measurement is desired, the cumulative uptake may be measured at each point by taking into account that the final pressure from the previous point is the starting pressure in the reactor. The final free gas density in each temperature region of V_2 must be multiplied by its respective volume ($V_{2,app}$ and $V_{2,bath}$) and added to the new free gas dose to get the total initial amount of adsorptive:

$$n_{i,cum,x} = \rho(P_{i,x}, T_{app})V_i + \rho(P_{f,x-1}, T_{app})V_{2,app} + \rho(P_{f,x-1}, T_{bath})\, V_{2,bath}$$

$$\Delta n_{e,x}(P_f, T_{bath}) = n_{i,cum,x} - n_{f,x}$$

$$n_{e,x}(P_f, T_{bath}) = n_{e,x-1} + \Delta n_{e,x}$$

Together, the series of points $n_{e,x}$ are used to find the function f:

$$n_e = f(P)_T = f(P_f)_{T_{bath}}$$

Equation A.10

A schematic of the procedure corresponding to the cumulative measurement of two adsorption points by the volumetric method is shown in Figure A.4. Equilibrium desorption isotherms are measured in a similar way. In the initial step, there is a high pressure in the reactor and a lower pressure (or zero pressure) in the staging manifold. It is helpful to have an additional pressure gauge in the reactor volume, but is not necessary.

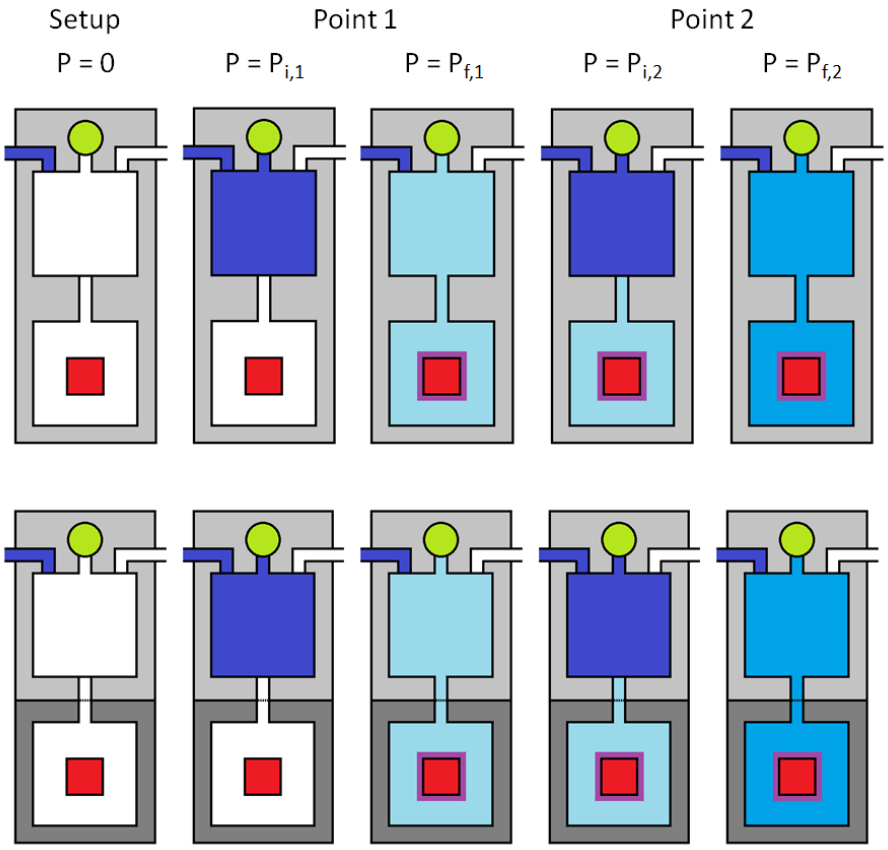

Figure A.4. The schematic representation of a 2 point dosing sequence during volumetric measurement of adsorption uptake, involving 2 steps at each point. The sequence is shown for increasing pressure steps from left to right. The top sequence corresponds to the simplest Sieverts apparatus, and the bottom corresponds to a practical apparatus. The pressure measured at each step is shown above.

Appendix B: Further Results Concerning Hydrogen Spillover

A response[4, 5] to our study presented in Chapter 3 opined that our materials were incorrectly synthesized, specifically questioning the nanoparticle dispersion and size. Attempts were made to compare TEM micrographs between materials, but this method of comparison is highly subject to bias in the region chosen. We suggest that a more accurate comparison be made by direct overlay of the XRD data of both materials, shown in Figure B.1. It can be seen that no significant difference, except possibly a *larger* mean particle size in Pt/AX-21[6], can be observed between it and Pt-MSC-30. The sharp peaks in the XRD data of Pt/AX-21 are not consistent with a Lorentzian shape and indicate the likelihood of a contribution by even larger particles as well. Both platinum-doped materials are confirmed to contain particles of diameter < 2 nm by TEM studies, but the distribution of particle sizes undoubtedly includes small particles as well as larger particles; we expect that if it was an important mechanism in overall uptake, enhancement due to spillover would be apparent in Pt-MSC-30 to a measurable extent.

Other points that should be addressed include:

1) The degas temperature used for Pt-MSC-30 was simply misstated, not incorrectly performed. The actual temperature of degas used in our studies was 623 K.
2) The Pt-content is ~30% higher in Pt-MSC-30 than Pt/AX-21, causing a more dramatic change in surface area upon doping. While the trend of decreased

spillover enhancement with increased catalyst loading was reported by Saha et al.[7] and Zieliński et al.[8], this was only for Ni particles in both cases. In fact, Saha reports that for Pt particles on OMC, spillover enhancement increased with Pt loading (up to 10 wt%). Enhancement due to spillover should still be measurable in Pt-MSC-30 if it plays an important role in overall hydrogen uptake. Furthermore, substantial (unexplained) hysteresis in the uptake measurements reported by Saha et al. is highly indicative of the type of error accumulation we have eliminated in our data by increasing sample size.

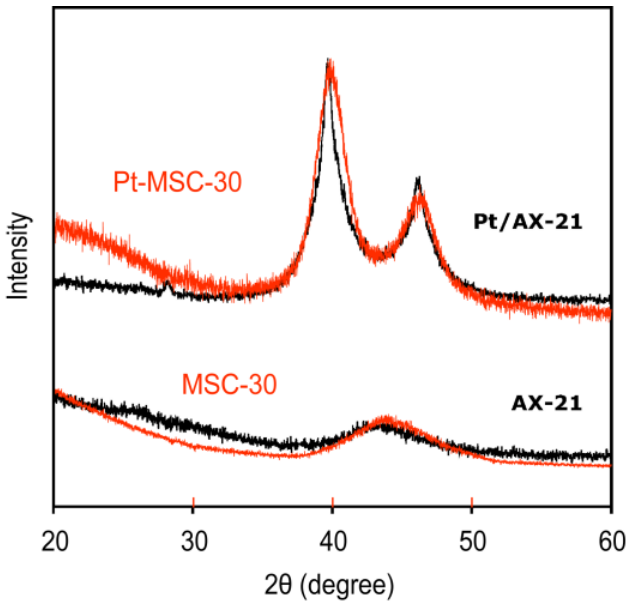

Figure B.1. XRD patterns of MSC-30 and Pt-MSC-30 (from this work) compared to Pt/AX-21 and AX-21.[6]

Further studies of the hydrogen spillover phenomenon and its role in hydrogen storage have been performed since our report. The experimental results can be

summarized by stating that uptake enhancement due to spillover is less than was originally reported in 2000-2007. Efforts to standardize the results have been undertaken by NIST. To control for differences in materials preparation, etc., the same samples were distributed to numerous groups for uptake measurements. We received a blind set of samples, used the specific degas protocols described by NIST, and contributed the results shown in Figure B.2. While the identity of the materials is not known to us, the results do show an appreciably higher hydrogen uptake capacity in Sample 2 (indicating the likelihood that Sample 1 is the standard and Sample 2 is the spillover material). However, the uptake in Sample 2 was not reversible at room temperature and desorption of hydrogen from the spillover sample was ~0.3 mmol g^{-1}, the same as in the pure carbon precursor. In addition, we studied the kinetics of possible hydrogen uptake by spillover, yielding the results shown in Figure B.3. After 2 hours of exposure to hydrogen at an equilibrium pressure of ~0.7 MPa, the measured pressure in the sample container was essentially constant within the limits of transducer resolution, indicating no significant ongoing adsorption associated with spillover. The temperature signal, converted to an effective pressure (from the assumption of constant volume and mass) can also be used to estimate changes in the thermodynamic state of the system: the rise of 0.5-1 Torr-equivalent of pressure as measured by temperature indicates that a maximum of ~1 Torr (0.1 kPa) may have left the gas phase over the course of the 2 hours, corresponding to 10^{-6} mol H_2, or ~2% of the total hydrogen adsorbed. We suggest this as an approximation of the limit of spillover contribution to hydrogen storage in this material.

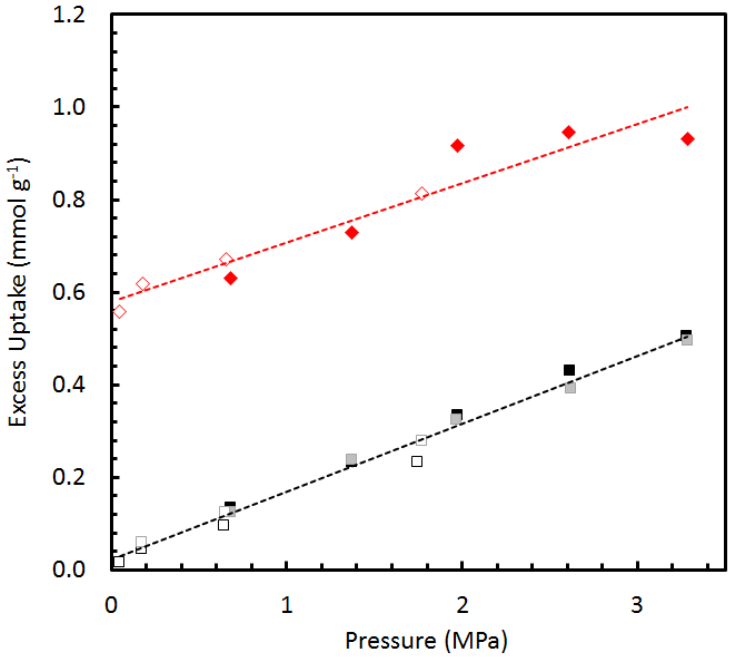

Figure B.2. Hydrogen adsorption isotherms (filled markers) of a sample of spillover-catalyst doped carbon "#2" (red) and its pure carbon precursor "#1" (black and gray) between 0-3.5 MPa at 298 K, showing a measurable increase in uptake in the spillover material. Reversible desorption (empty markers) is also shown.

The combined results from the entire multi-group NIST study led to the following conclusions:

1) The maximum uptake capacity of spillover materials is < 1 wt%, or 5 mmol g^{-1}, at 298 K, significantly below the original reports for Pt/AX-21 and IRMOF-8.

2) The presence of palladium nanoparticles is itself responsible for up to 30% enhancement in those materials, and the amount of enhanced hydrogen sorption by hydride formed should be subtracted from the capacity attributed to spillover.

3) The measurable enhancement of hydrogen uptake attributed to spillover ranged from 0-50% despite rigorous attempts to control sample quality.

4) The degassing temperature is considered a crucial step for proper sample preparation, and reversibility was an unresolved issue across all samples.

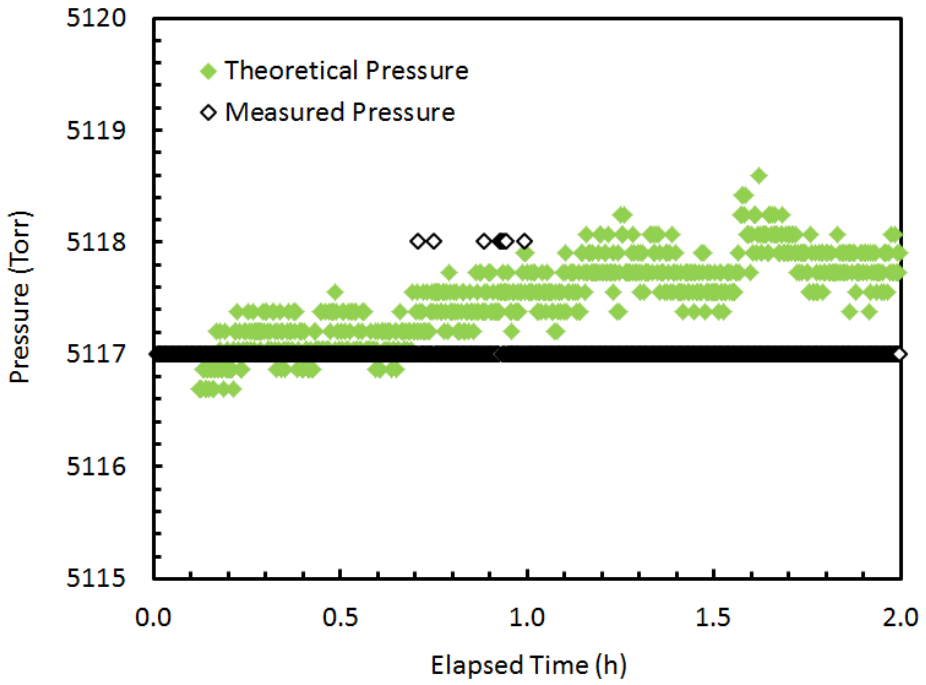

Figure B.3. The temperature and pressure data, shown in units of Torr, during an adsorption measurement step in sample #2, a spillover-catalyst decorated carbon, at 298 K and ~0.7 MPa. The difference in the signals from pressure (black unfilled diamond) and temperature (green diamond) could potentially be attributed to ongoing spillover, corresponding to 2% of the total uptake at this step: 0.01 wt% H_2.

Appendix C: Carbon Dioxide Adsorption on ZTCs

During the studies of gas adsorption on ZTCs, carbon dioxide measurements were performed in addition to the N_2, H_2, and CH_4 isotherms presented in Chapters 4-5. The results are presented in Figures C.1-2.

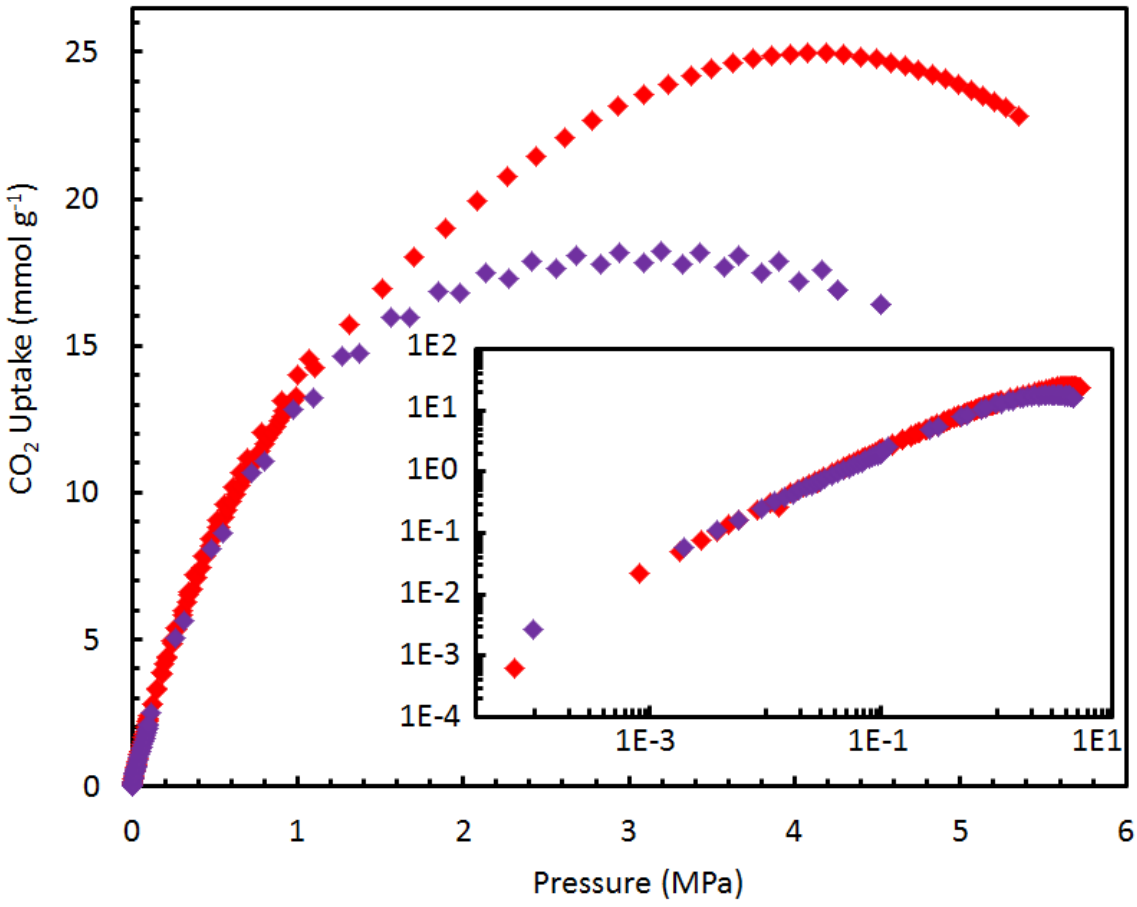

Figure C.1. Equilibrium excess adsorption isotherms of carbon dioxide on ZTC-2 (purple) and MSC-30 (red) at 298 K.

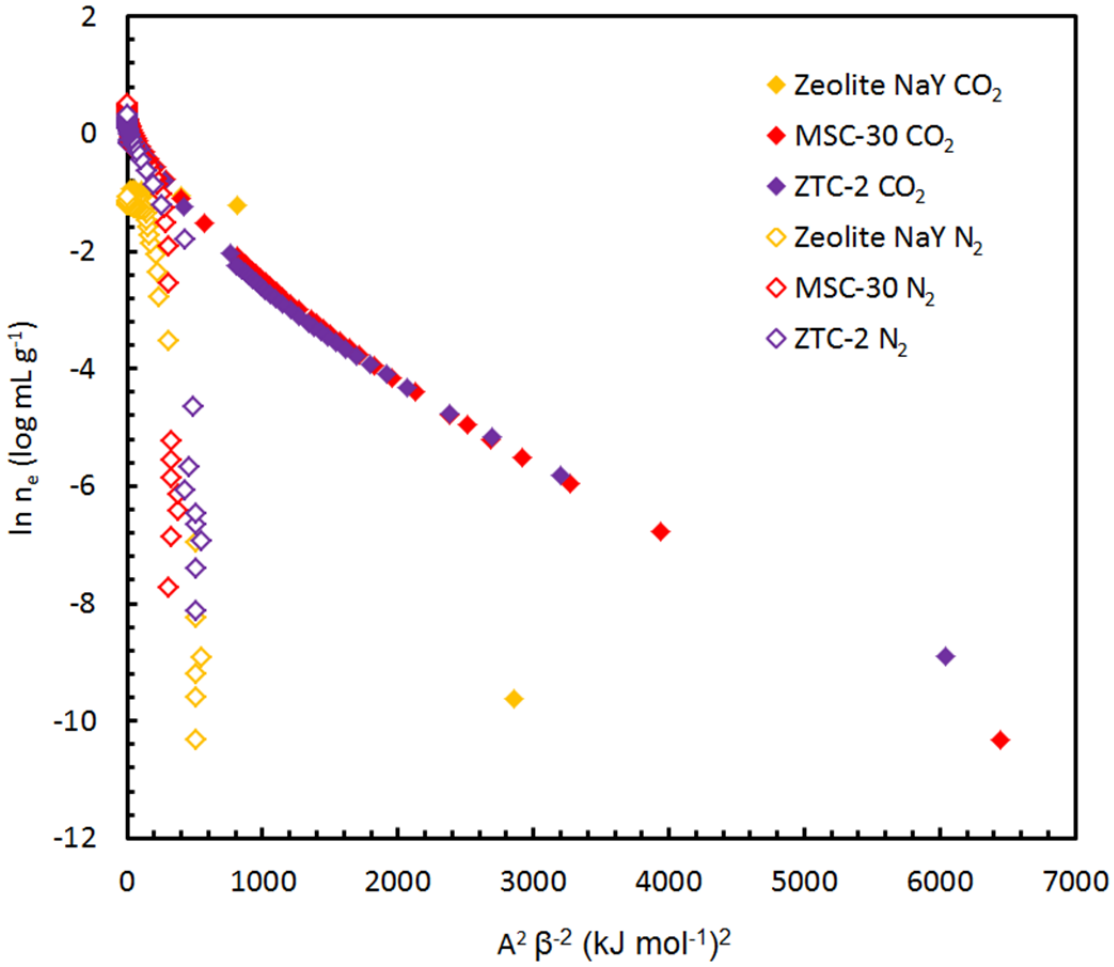

Figure C.2. Characteristic curves of N_2 (unfilled diamonds, 77 K) and CO_2 (solid diamonds, 298 K) adsorption on zeolite NaY (yellow), MSC-30 (red), and ZTC-2 (purple).

The results remain unclear, and not enough data was collected. However, it appears that while CO_2 adsorption at 298 K was similar between MSC-30 and ZTC-2, N_2 adsorption at 77 K was significantly different between them. It is interesting to note that N_2 adsorption in ZTC-2 and its raw zeolite template (NaY) show similar behavior at low pressure (where low pressure corresponds to large A^2/β^2 in the "characteristic curve"[9]). Further work remains to be done, and it is likely that more promising results could be obtained with the higher fidelity ZTC sample, ZTC-3.

Appendix D: BET and DR Trends of Adsorption Uptake

We have routinely performed Dubinin-Radushkevich[10] (DR) analyses on adsorbent materials to determine if there is a different trend than for BET surface area, and typically did not find a different result (see Figure D.1). Owing to its wider use and acceptance, the BET method was chosen for the results presented throughout this work.

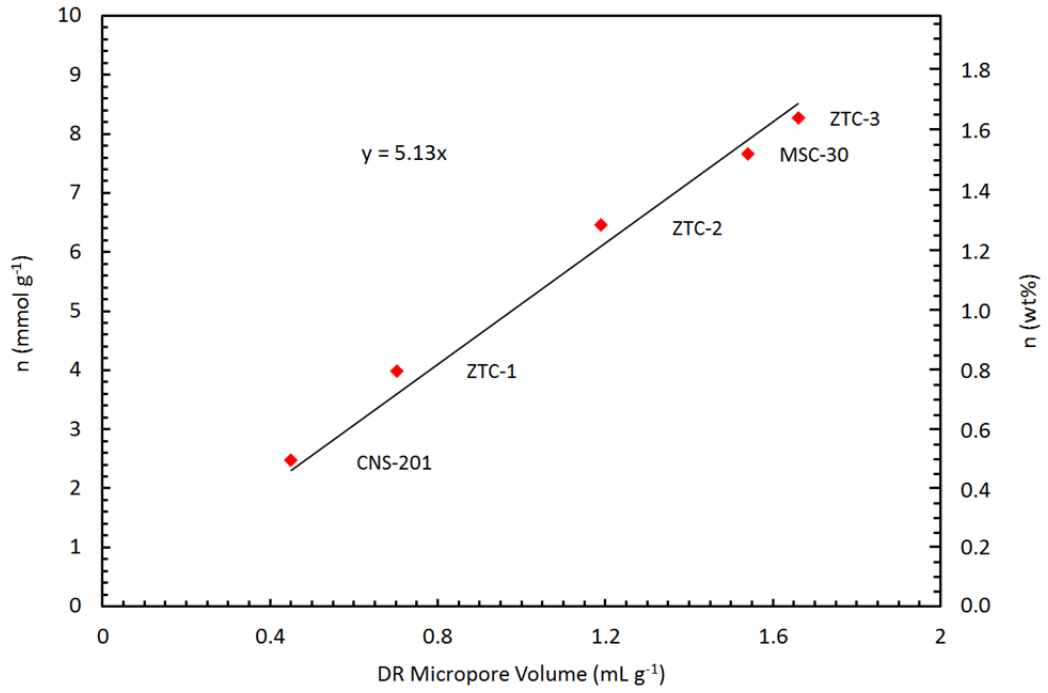

Figure D.1. Excess hydrogen uptake at 30 MPa and 298 K for various carbon materials as a function of DR micropore volume.

Appendix E: Pressure Driven Phase Transition

During gas adsorption measurements, gas is expanded through a valve into the sample container, as described in Appendix A. A fixed amount of gas, expanded from an initial pressure P_i, will equilibrate with the adsorbent at pressure P_f, determined by the properties of the adsorbent and the ratio of the final volume to the initial volume, $x = V_i/V_f$. Compared to an identical non-adsorption reference case, expansion of gas into a container filled with adsorbent results in a lower pressure and a lower free energy from solid-adsorbate interactions. This difference in pressure between the reference state and the adsorption system corresponds to a difference in chemical potential given by:

$$\Delta\mu_{ads}(P_i, P_f) = \mu(P_f, T) - \mu(P_i, T)$$

Equation E.1

The thermodynamic driving force for adsorption can be interpreted as this change in chemical potential. The larger the surface available for adsorption, and hence the more adsorptive molecules that can depart the gas phase to undergo adsorption, the larger the change in free energy of the system. In a carefully designed experiment, this potential difference can drive a phase transition of an adsorbent material to a lower free energy state where more binding sites are available for adsorption. The nature of the chemical potential in the non-ideal gas region for hydrogen and methane is different (see Figure 6.3).

As described in Section 6.2.2, this final state would be energetically favorable since adsorption interactions would lower the total free energy below that of the bound state. For carbon nanotubes, this corresponds to the separation of bundles to expose the full surface of the individual tubes, represented in Figure E.1. A series of TEM images (Figure E.2) verify the initial, bundled state of single-walled nanotubes obtained in early investigations.

With an adsorption isotherm measurement at temperature *T*, it is possible to derive the relationship between P_i and P_f for a specific amount of adsorbent in a given void volume if the adsorption isotherm is known. The change in chemical potential is unique to the experimental setup since the pressure change is dependent on the volume; for a large volume relative to the amount of adsorbent, the change in chemical potential will be small since the pressure drop associated with adsorption is small. However, with carefully chosen experimental conditions, one can effect a substantial decrease in chemical potential with the addition of a high surface for adsorption to an empty container. Initial calculations of the effective chemical potential that could be applied for different experimental conditions are shown in Figures E.3-4. Numerous simplifying approximations were used in order to predict the final pressure based on experimental excess hydrogen and methane adsorption uptake measured of MSC-30 compared to CNS-201. A key step was to assume that the bundled structures have a surface area 5% that of MSC-30 (150 $m^2\ g^{-1}$), and therefore 5% the excess maximum uptake before phase transition. After phase transition, the surface area was approximated to grow 10 fold. This is the maximum increase given the geometry of a typical bundle of 7 tubes.

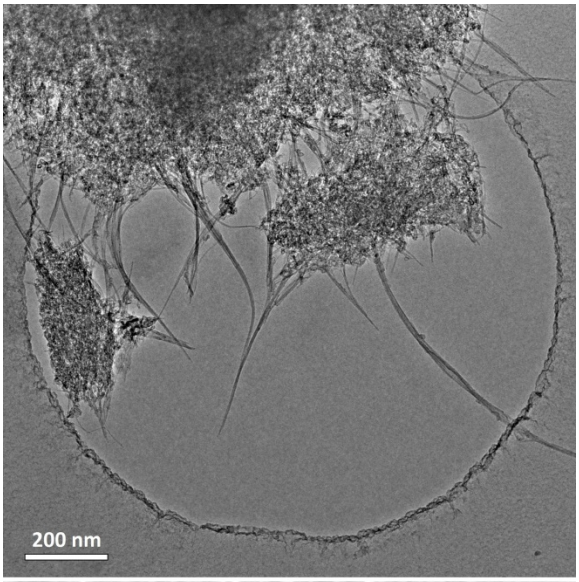

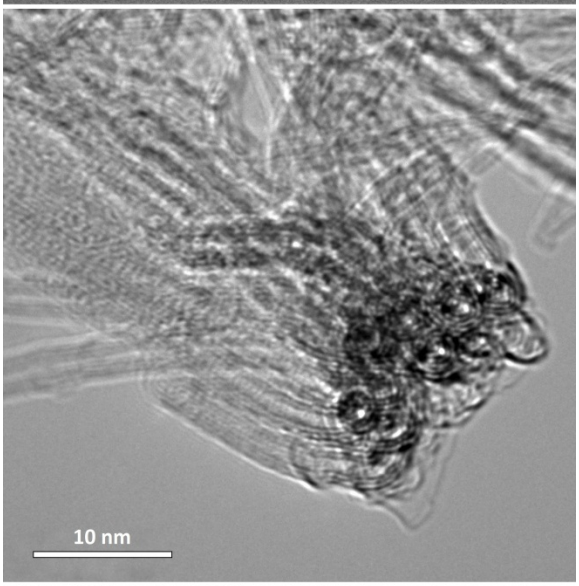

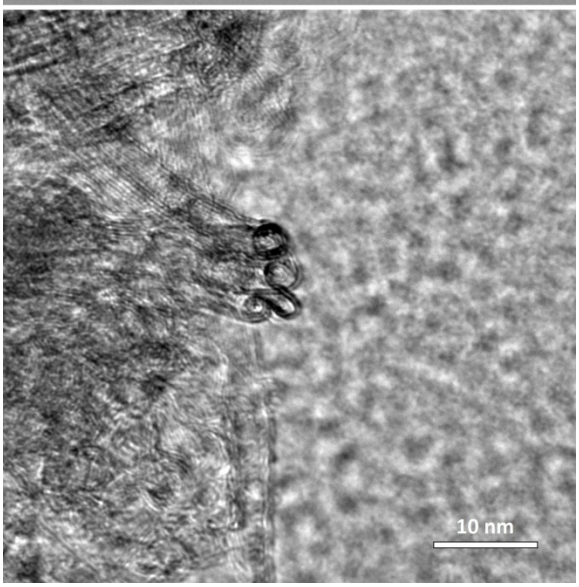

Figure E.2. (left) TEM micrographs of single-walled carbon nanotubes over a holey-carbon grid, showing their bundled structure.

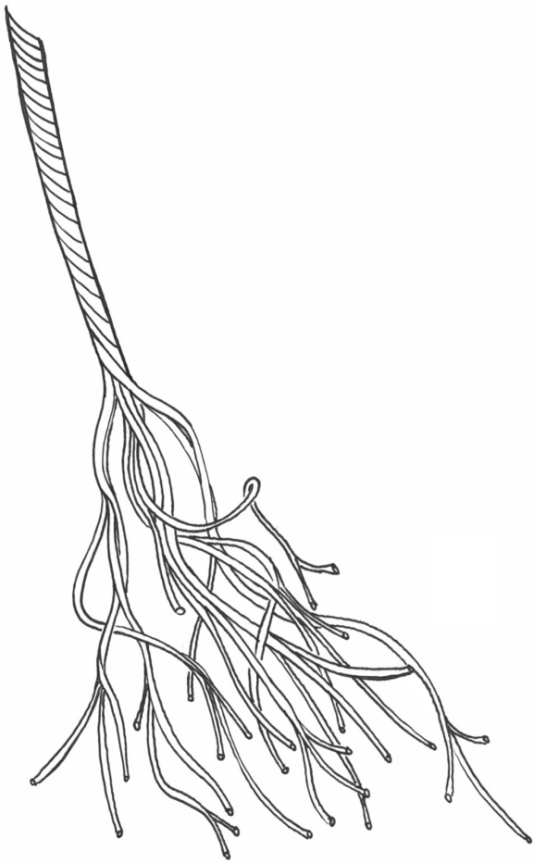

Figure E.1. (above) An artistic representation of the un-bundling of the rope structure of single-walled carbon nanotubes.

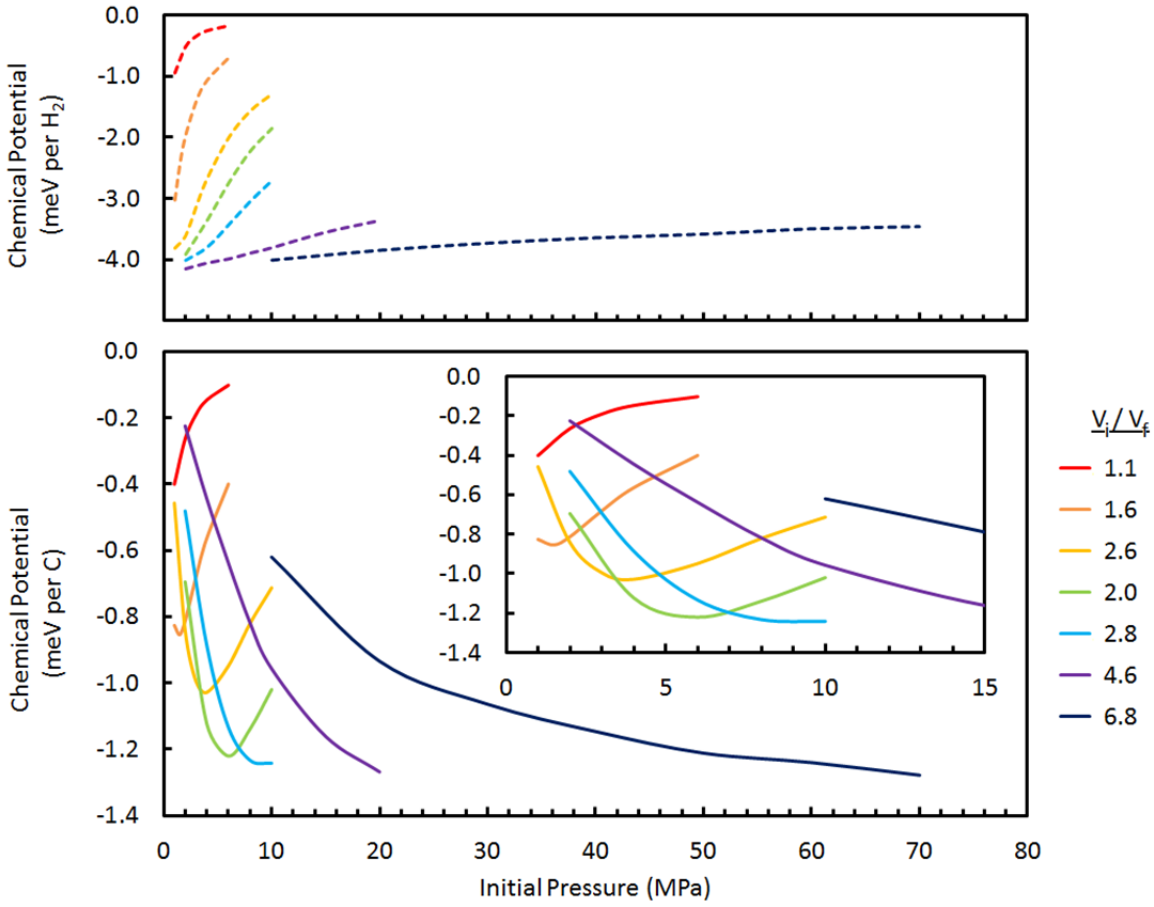

Figure E.3. (top) The change in chemical potential after a 1-step hydrogen expansion between 2 fixed volumes, one containing adsorbent, in a temperature bath held at 77 K, and (bottom) the corresponding effective change per carbon atom (a function of surface coverage) in seven different apparatuses with total volumes:
51 mL (red), 17 mL (orange), 10 mL (yellow), 2 L (green), 32 mL (light blue), 23 mL (purple), and 1 L (dark blue).

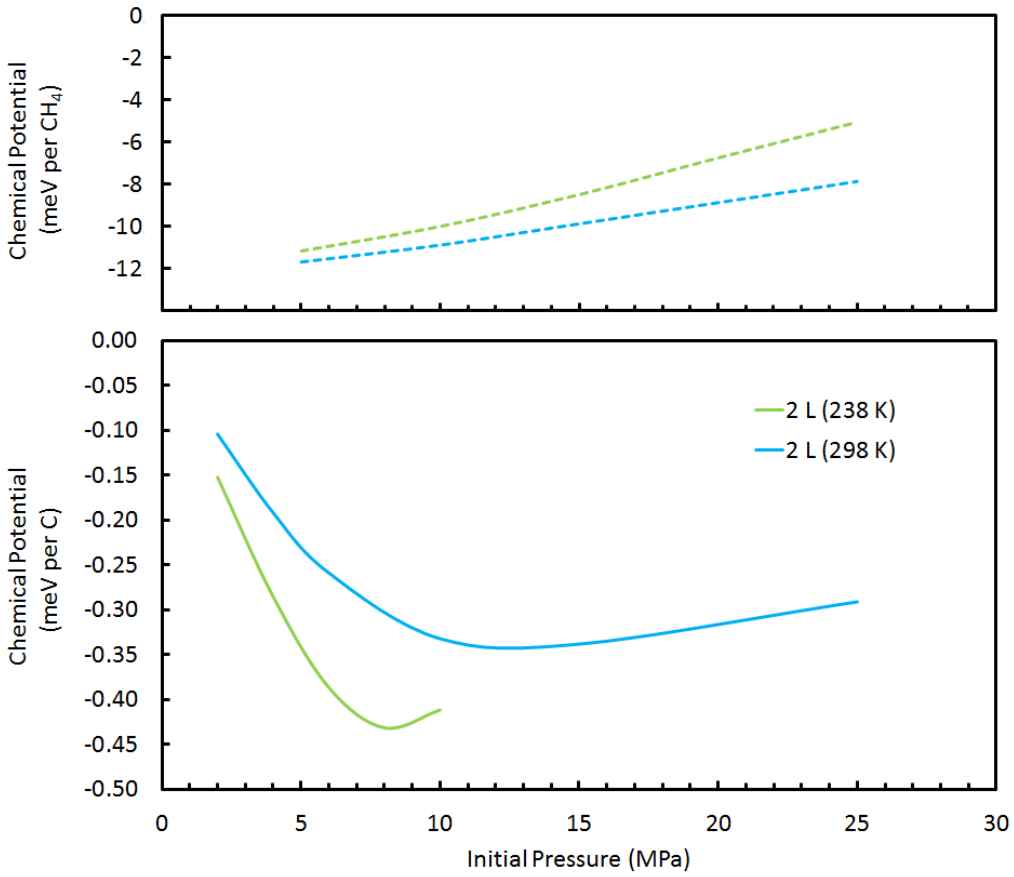

Figure E.4. (top) The change in chemical potential after a 1-step methane expansion between 2 fixed volumes, one containing adsorbent, in a fixed temperature bath, and (bottom) the corresponding effective change per carbon atom (a function of surface coverage), in the same model apparatus (2 L total volume) at two temperatures:
238 K (green) and 298 K (blue).

Appendices References

(1) A. Sieverts, 'Die aufnahme von gasen durch metalle', *Z. Metallkd.,* **21**, 37-46 (1929).

(2) H. Wu, W. Zhou, and T. Yildirim, 'High-capacity methane storage in metal-organic frameworks M2(dhtp): the important role of open metal sites', *J. Am. Chem. Soc.,* **131**, 4995-5000 (2009).

(3) K. Sillar and J. Sauer, 'Ab initio prediction of adsorption isotherms for small molecules in metal-organic frameworks: the effect of lateral interactions for methane/CPO-27-Mg', *J. Am. Chem. Soc.*, doi: 10.1021/ja307076t (2012).

(4) N. R. Stuckert, L. Wang, and R. T. Yang, 'Characteristics of hydrogen storage by spillover on Pt-doped carbon and catalyst-bridged metal organic framework', *Langmuir,* **26**, 11963-11971 (2010).

(5) H. Chen and R. T. Yang, 'Catalytic effects of TiF3 on hydrogen spillover on Pt/carbon for hydrogen storage', *Langmuir,* **26**, 15394-15398 (2010).

(6) Y. Li and R. T. Yang, 'Hydrogen storage on platinum nanoparticles doped on superactivated carbon', *J. Phys. Chem. C,* **111**, 11086-11094 (2007).

(7) D. Saha and S. Deng, 'Hydrogen adsorption on ordered mesoporous carbons doped with Pd, Pt, Ni, and Ru', *Langmuir,* **25**, 12550-12560 (2009).

(8) M. Zieliński, R. Wojcieszak, S. Monteverdi, M. Mercy, and M. M. Bettahar, 'Hydrogen storage in nickel catalysts supported on activated carbon', *Int. J. Hydrogen Energy,* **32**, 1024-1032 (2007).

(9) D. Cazorla-Amorós, J. Alcañiz-Monge, and A. Linares-Solano, 'Characterization of activated carbon fibers by CO2 adsorption', *Langmuir,* **12**, 2820-2824 (1996).

(10) S. J. Gregg and K. S. W. Sing, *Adsorption, surface area, and porosity*, Academic Press, London (1982).